

NEAR-FIELD CHARACTERISTICS OF ELECTRIC DIPOLE  
ANTENNAS IN THE INNER MAGNETOSPHERE

A DISSERTATION  
SUBMITTED TO THE DEPARTMENT OF ELECTRICAL  
ENGINEERING  
AND THE COMMITTEE ON GRADUATE STUDIES  
OF STANFORD UNIVERSITY  
IN PARTIAL FULFILLMENT OF THE REQUIREMENTS  
FOR THE DEGREE OF  
DOCTOR OF PHILOSOPHY

Timothy W. Chevalier

October 2007

© Copyright by Timothy W. Chevalier 2008  
All Rights Reserved

I certify that I have read this dissertation and that, in my opinion, it is fully adequate in scope and quality as a dissertation for the degree of Doctor of Philosophy.

---

(Umran S. Inan) Principal Adviser

I certify that I have read this dissertation and that, in my opinion, it is fully adequate in scope and quality as a dissertation for the degree of Doctor of Philosophy.

---

(Timothy F. Bell)

I certify that I have read this dissertation and that, in my opinion, it is fully adequate in scope and quality as a dissertation for the degree of Doctor of Philosophy.

---

(Antony C. Fraser-Smith)

Approved for the University Committee on Graduate Studies.

*This dissertation is dedicated to my parents Virginia and William;  
to my wife, Jane;  
and to my daughter, Hannah Grace.*

# Abstract

Electric dipole antennas are commonly used in space plasmas with applications that range from radio frequency probing of the magnetosphere to plasma diagnostics. With the recent interest in the in-situ injection of ELF/VLF waves for the study of magnetospheric wave-particle interactions, the characterization of the antenna-plasma coupling behavior in this regime is of primary importance. The coupling considered in this dissertation occurs in an operating environment that corresponds to magnetospheric conditions found between  $L=2$  and  $L=3$  in the geomagnetic equatorial plane. The magnetized plasma at this location is fully ionized and collisionless, consisting largely of electrons and protons.

The near field of the antenna consists of a plasma sheath which envelops the antenna, directly affecting the terminal impedance properties (and hence tuning parameters) of the antenna. Inside the sheath region, the plasma dynamics are highly nonlinear and must be solved numerically. In order to optimally inject VLF waves and thereby maximize the antenna-plasma coupling response, it is necessary to determine the near-field characteristics of electric dipole antennas operating within this region of space. This dissertation addresses the efficacy of using VLF electric dipole antennas as in-situ wave injection instruments and focuses on the near-field coupling of these antennas to the environment in which they are immersed.

A two-tiered hydrodynamic approach has been developed to solve for the plasma dynamics in the region surrounding the antenna. First, a three-dimensional parallelized full wave solution of Maxwell's equations is implemented to simulate the current distribution and input impedance of an electric dipole antenna operating in a cold magnetoplasma at VLF. It is shown that the current distribution for antennas

with length  $<100$  m is approximately triangular for magnetospheric conditions found at  $L=2$  and  $L=3$  in the geomagnetic equatorial plane. Calculated variations of input impedance as a function of drive frequency are presented for two case studies and compared with predictions of existing analytical work.

This model is then extended to include finite temperature effects allowing for the determination of the sheath characteristics as a function of drive frequency and voltage. The primary assumptions underlying the closure mechanisms for the infinite set of fluid moments are examined through theoretical observations and simulated comparisons of the various truncation schemes. Results from these two models allow for the complete characterization of the near-field properties of electric dipole antennas operating in this highly anisotropic environment.

# Acknowledgements

As the final days of this epic journey come to a glorious end, I would like to thank those people who made the pursuit of this elusive Ph.D degree an intellectual odyssey and tremendously gratifying experience.

First, I wish to express sincere thanks to my principal adviser Professor Umran Inan for allowing me to work on a breadth of research projects during my tenure at Stanford. I am very grateful for his enthusiasm and encouragement through the years; most notably, his eagerness to send me to remote locations on the globe such as Antarctica and the dense, dark forests of Alaska, which very few have had the opportunity to see.

Next, I would like to thank the members of my defense committee: Dr. Timothy Bell, Professor Tony Fraser-Smith and Professor Shanhui Fan. I am grateful to Dr. Bell for our insightful late night conversations, both research and non-research related, and for being the second reader of this dissertation. To the third reader of my dissertation, Professor Tony Fraser-Smith, I thank for entertaining discussions on every topic and for more serious advice about where to tour in his beautiful homeland, New Zealand. I am thankful to Professor Shanhui Fan for chairing my oral defense session. Additionally, I wish to acknowledge the generous insights and intellectual offerings of Professors Don Carpenter, Martin Walt, Robert Helliwell and, in memoriam, Ronald Bracewell, throughout the many, long years. Lastly, I thank Professor Donald Cox for use of his super-computing cluster which was essential to my research.

Shaolan Min has been an invaluable friend, both in terms of administrative related activities and putting together some great holiday parties. I also thank Shaolan, along with Helen Niu, for providing much appreciated assistance with and advice on

parenting.

I wish to extend my gratitude to all past and present VLF group members for making my experience at Stanford a fondly memorable one, especially Dr. Jacob Bortnik, Dr. Robert Moore, Dr. Joseph Payne, Dr. Maria Spasojevic, Dr. Troy Wood, Dr. Ana Bertran-Ortiz, Cécile Le Cocq, Ben Cotts, Hrefna Gunnarsdottir, Sarah Harriman, Max Klein, Prajwal Kulkarni, Bob Marshall, Ryan Said, Erin Selser and Fraser Thomson. Thanks so much guys!

I would like to give special thanks to my parents William and Virginia, and to my siblings William, Karen, Michele, Michael and Kevin, and their families, for their steadfast encouragement and support. In particular, my brother Dr. Michael Chevalier has been a great mentor and collaborator as we pursued our degrees together at Stanford in the VLF group. You made my experience exceptionally fulfilling.

To my beautiful wife Jane, I would like to express my love and gratitude for your endless patience and unwavering support through this entire process, despite the fact that she probably thought this dissertation might never come to fruition. And finally, I would like to thank my darling daughter Hannah Grace whose birth provided the necessary motivation to finish, and whose laughter and love is one of life's great blessings.

TIMOTHY W. CHEVALIER

*Stanford, CA*

*October 2007*

The work in this dissertation was supported by the Air Force Office of Scientific Research (AFOSR) under grant F49620-03-1-0338, by the Multidisciplinary University Research Initiative (MURI) under grant Z882802, by Sequoia Technologies under grant SEQ-07-04-01, and by the High-Frequency Active Auroral Research Program (HAARP).

# Contents

<b>Abstract</b>	<b>v</b>
<b>Acknowledgements</b>	<b>vii</b>
<b>1 Introduction</b>	<b>1</b>
1.1 Van Allen Radiation Belts . . . . .	2
1.2 Antenna-plasma Coupling . . . . .	3
1.3 Antennas in Linearized Plasma Regimes . . . . .	5
1.3.1 Theoretical Work . . . . .	5
1.3.2 Simulation Work . . . . .	8
1.4 The Plasma Sheath Region . . . . .	8
1.4.1 Sheaths Surrounding Electric Dipole Antennas . . . . .	9
1.4.2 Sheath Waves . . . . .	10
1.4.3 Planar Sheaths and RF Discharges . . . . .	10
1.4.4 Numerical Simulation and Laboratory Work . . . . .	12
1.4.5 Hydrodynamic Closure Relations . . . . .	15
1.5 Thesis Organization . . . . .	18
1.6 Scientific Contributions . . . . .	19
<b>2 Derivation of Hydrodynamic Moment Method</b>	<b>20</b>
2.1 Theoretical Formulation . . . . .	20
2.1.1 Moments of the Vlasov Equation . . . . .	21
2.2 Instabilities and Resonances . . . . .	25
2.2.1 Two-Stream Instability and Landau Damping . . . . .	26

2.2.2	Particle Trapping and Secondary Emission . . . . .	27
<b>3</b>	<b>Cold Plasma Electromagnetic Model</b>	<b>29</b>
3.1	Cold Plasma Simulation Development . . . . .	29
3.2	Theoretical Formulation . . . . .	31
3.3	Simulation Properties . . . . .	33
3.3.1	Computational Mesh Setup . . . . .	33
3.3.2	Frequency Domain Technique . . . . .	36
3.3.3	Boundary Condition Instabilities . . . . .	38
3.3.4	PML Derivation . . . . .	39
3.3.5	PML in Free-space . . . . .	40
3.3.6	PML in the Whistler Mode . . . . .	41
3.3.7	Solution to PML Instability in Whistler Mode . . . . .	44
3.3.8	The Z-mode Instability . . . . .	46
<b>4</b>	<b>Current Distribution and Terminal Impedance</b>	<b>48</b>
4.1	Simulation Setup . . . . .	48
4.2	Antenna Current Distribution in Free-space . . . . .	53
4.3	Current Distributions and Input Impedance Calculations for a 100 m Antenna at $L=2$ . . . . .	54
4.4	Current Distributions and Input Impedance Calculations for a 100 m Antenna at $L=3$ . . . . .	57
4.5	Non-triangular Current Distributions . . . . .	59
4.5.1	Long Antennas . . . . .	59
4.5.2	High Plasma Frequency . . . . .	60
<b>5</b>	<b>Warm Plasma Electrostatic Model</b>	<b>62</b>
5.1	Closure Approximations . . . . .	62
5.2	Quasi-Electrostatic Approximation . . . . .	64
5.3	Simulation Development . . . . .	65
5.3.1	Fluid Formulation . . . . .	66
5.3.2	Normalization of Fluid Equations . . . . .	69

5.3.3	Multi-scale Simulations . . . . .	69
5.3.4	Boundary Conditions . . . . .	70
<b>6</b>	<b>Plasma Sheath Results</b>	<b>73</b>
6.1	One-dimensional Planar Sheath . . . . .	74
6.1.1	Bohm Sheath Derivation . . . . .	74
6.1.2	1-D Simulation of Planar Sheath . . . . .	75
6.2	Two-dimensional Infinite Line Source . . . . .	78
6.2.1	Proton Dynamics . . . . .	79
6.2.2	Comparison of Isothermal and Adiabatic Closure Conditions for Sinusoidal Excitation . . . . .	82
6.2.3	Comparison of Isothermal and Adiabatic Closure Conditions for Pulse Train Excitation . . . . .	85
6.3	Three-dimensional Dipole Antenna . . . . .	88
6.3.1	Antenna at $L=3$ with Electron Gun and 2 m Gap . . . . .	90
6.3.2	Antenna at $L=2$ with Electron Gun and 2 m Gap . . . . .	95
6.3.3	Antenna at $L=3$ with Electron Gun and 20 cm Gap . . . . .	99
6.3.4	Antenna at $L=3$ without Electron Gun and 2 m Gap . . . . .	102
6.3.5	Antenna Tuning . . . . .	106
<b>7</b>	<b>Summary and Suggestions for Future Work</b>	<b>107</b>
7.1	Cold Plasma Model Contributions . . . . .	107
7.2	Warm Plasma Model Contributions . . . . .	108
7.3	Suggestions for Future Research . . . . .	109
7.3.1	Adaptive Mesh Refinement . . . . .	109
7.3.2	Unstructured Grids and Sub-cell Modeling . . . . .	110
7.3.3	Particle in Cell Methods . . . . .	110
<b>A</b>	<b>Tensor Quantities</b>	<b>111</b>
<b>B</b>	<b>Time Integration Schemes</b>	<b>113</b>
B.1	Staggered Leapfrog . . . . .	113

B.2	Runge-Kutta Methods . . . . .	113
B.2.1	Explicit Runge Kutta . . . . .	115
B.2.2	Implicit Runge Kutta . . . . .	115
B.3	Alternating Direction Implicit . . . . .	117
<b>C</b>	<b>Time Domain Solution to Z-mode Instability</b>	<b>118</b>
C.1	Low-Pass Filtering of Cold Plasma Equations . . . . .	119
<b>D</b>	<b>Details of Finite Volume Method</b>	<b>121</b>
D.1	Shocks and Artificial Viscosity . . . . .	121
D.2	Flux Calculation . . . . .	122
D.3	Shock Capture . . . . .	123

# List of Tables

B.1	Butcher array for general Runge-Kutta method . . . . .	114
B.2	Butcher array for Explicit Runge-Kutta (ERK) method . . . . .	115
B.3	Butcher array for Single Diagonally Implicit Runge-Kutta (SDIRK) method . . . . .	116

# List of Figures

1.1	Conceptual drawing of radiation belts . . . . .	3
1.2	Antenna-plasma coupling regions . . . . .	4
2.1	Transport properties . . . . .	23
3.1	Computational mesh of Lee and Kalluri . . . . .	33
3.2	Longitudinal oscillations . . . . .	35
3.3	Finite-difference stencil . . . . .	36
3.4	Free-space refractive index surface . . . . .	41
3.5	Cold plasma dispersion diagrams . . . . .	42
3.6	Whistler mode refractive index surfaces . . . . .	43
3.7	Unstable PML for whistler mode propagation . . . . .	44
3.8	Unstable PML for Z-mode propagation . . . . .	46
4.1	Computational domain for cold plasma simulations . . . . .	49
4.2	Cell layout for cold plasma calculations at $L=2$ . . . . .	51
4.3	PML performance . . . . .	52
4.4	Current distribution on thin linear antenna . . . . .	54
4.5	Current distributions for a 100 m antenna at $L=2$ . . . . .	55
4.6	Input impedance for a 100 m antenna at $L=2$ . . . . .	56
4.7	Current distributions for a 100 m antenna at $L=3$ . . . . .	58
4.8	Input impedance for a 100 m antenna at $L=3$ . . . . .	58
4.9	Current distributions for increased antenna length . . . . .	60
4.10	Current distributions for increased plasma frequency . . . . .	60

5.1	Electrostatic potential variation on electrically short dipole antenna . . . . .	65
5.2	Fluid boundary condition at conductor surface . . . . .	72
6.1	Comparison of 1-D planar sheath simulation with analytical results. . . . .	77
6.2	Conceptual drawing of two-dimensional simulation region . . . . .	79
6.3	Slice plane through infinite line source . . . . .	79
6.4	Transient response of 2-D simulation at $L=3$ . . . . .	80
6.5	Snapshot during positive potential cycle of infinite line source . . . . .	81
6.6	Snapshot during negative potential cycle of infinite line source . . . . .	82
6.7	Current-voltage relationship for isotropic plasma with 15 kHz sinusoid . . . . .	83
6.8	Current-voltage relationship for isotropic plasma with 25 kHz sinusoid . . . . .	83
6.9	Current-voltage relationship for magnetized plasma with 15 kHz sinusoid . . . . .	84
6.10	Current-voltage relationship for magnetized plasma with 25 kHz sinusoid . . . . .	85
6.11	Current-voltage relationship for isotropic plasma with 15 kHz pulse train . . . . .	86
6.12	Current-voltage relationship for isotropic plasma with 25 kHz pulse train . . . . .	86
6.13	Current-voltage relationship for magnetized plasma with 15 kHz pulse train . . . . .	87
6.14	Current-voltage relationship for magnetized plasma with 25 kHz pulse train . . . . .	88
6.15	Location of sheath edge . . . . .	89
6.16	Three-dimensional computational domain at $L=3$ . . . . .	90
6.17	Orthographic projection of sheath at $L=3$ . . . . .	91
6.18	Electron and proton density variation for antenna at $L=3$ . . . . .	92
6.19	Terminal characteristics for 20 m antenna at $L=3$ . . . . .	93
6.20	Inter-element gap current for dipole antenna at $L=3$ . . . . .	94
6.21	Three-dimensional computational domain at $L=2$ . . . . .	95
6.22	Orthographic projection of sheath at $L=2$ . . . . .	96
6.23	Electron and proton density variation for antenna at $L=2$ . . . . .	97
6.24	Terminal characteristics for 20 m antenna located at $L=2$ . . . . .	98
6.25	Inter-element gap current for dipole antenna at $L=2$ . . . . .	99
6.26	Orthographic projection of sheath at $L=3$ with 20 cm gap . . . . .	100

6.27	Electron and proton density variation for antenna at $L=3$ with 20 cm gap . . . . .	101
6.28	Terminal characteristics for 20 m antenna located at $L=3$ with 20 cm gap . . . . .	102
6.29	Inter-element gap current for dipole antenna at $L=3$ with 20 cm gap .	102
6.30	Orthographic projection of sheath at $L=3$ without electron gun . . .	103
6.31	Electron and proton density variation for antenna at $L=3$ without electron gun . . . . .	104
6.32	Terminal characteristics for 20 m antenna located at $L=3$ without electron gun . . . . .	105
6.33	Inter-element gap current for dipole antenna at $L=3$ without electron gun . . . . .	106
D.1	Example of shock capturing scheme . . . . .	124

# Chapter 1

## Introduction

The purpose of this dissertation is to determine the near-field behavior of electric dipole antennas operating in a magnetized plasma environment. To perform this task, we have developed a comprehensive simulation tool to explore various aspects of the coupling response. This simulation tool is referred to as the Antenna-In-Plasma (AIP) code. The work presented herein is motivated by the interest in using electric dipole antennas as in-situ wave injection instruments to study wave-particle interactions within the magnetosphere. Since one of the possible applications of this research is the pitch-angle scattering of highly energetic electrons from the inner radiation belts, we consider frequencies that lie within the Very Low Frequency (VLF) band from 3-30 kHz.

A magnetized plasma is a highly nonlinear, conducting, and anisotropic medium. The determination of the antenna-plasma coupling is thus a very challenging task. This introductory chapter focuses on both early and recent attempts at characterizing the performance of electric dipole antennas operating in this region of space. Throughout this dissertation we emphasize the shortcomings of these previous works and highlight our contributions in the context of the numerical simulation tool (i.e., AIP code) developed as a product of this research. After a discussion in this chapter of the relevant background material presented, we proceed with the theoretical development and application of our AIP code to address several aspects of antenna-plasma coupling. Initially, the plasma is treated as a linear medium and we compare

the current distribution and terminal input impedance as predicted by our model with available analytical results in order to validate the AIP code. Finally, we increase the complexity of our validated tool in order to study the inherent nonlinear characteristics of the plasma sheath in a regime for which theoretical results are not available. The contributions from this dissertation emphasize the importance of detailed numerical simulation work in the accurate analysis of dipole antennas operating in this complex magnetoplasma environment.

## 1.1 Van Allen Radiation Belts

The Van Allen radiation belts are two toroidal regions surrounding the Earth, populated primarily with energetic protons and electrons [Walt, 1994, pages 1-9]. These two regions cover the range in  $L$ -shell from  $L \simeq 1.2-2.5$  and  $L \simeq 2.8-10$  constituting the so-called inner and outer belts respectively. The parameter  $L$  is defined as the distance in Earth radii (assuming a tilted, off-center dipolar magnetic field) from the center of the Earth to a point on the corresponding magnetic field line located in the geomagnetic equatorial plane [Walt, 1994, page 54]. A diagram depicting the inner and outer belts is shown in Figure 1.1.

For many years, the study of electromagnetic wave propagation and wave-particle interactions in this region of space has received a great deal of interest [Carpenter and Anderson, 1992; Carpenter et al., 2003; Bell et al., 2004; Platino et al., 2005]. Along with electromagnetic waves launched from ground based VLF transmitters, naturally occurring VLF radiation such as whistlers injected by lightning discharges and hiss and chorus emissions generated by the energetic magnetospheric plasma have been shown to influence the populations of these highly energetic electrons that reside within the Earth's radiation belts [Abel and Thorne, 1998]. It has been recently proposed [Inan et al., 2003], that space-based transmitters may be used as in-situ wave-injection instruments for the purpose of mitigating unwanted and harmful enhancements of energetic electron fluxes in the inner radiation belt. As suggested by Albert [2001], the dominant mechanism behind the precipitation of these energetic

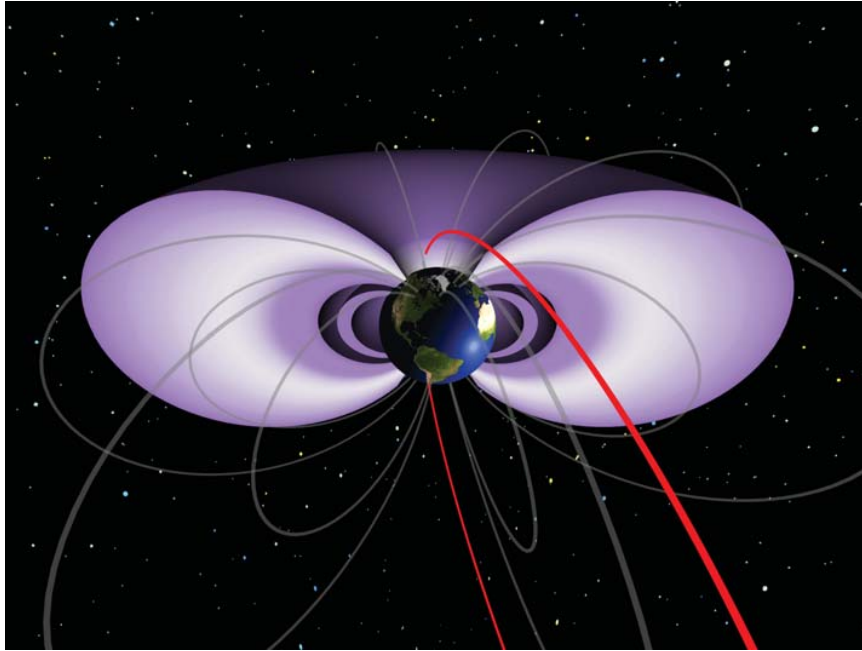


**Figure 1.1:** Conceptual drawing of inner and outer radiation belts. Taken from <http://www.nasa.gov/centers/goddard/images/content/> Credit: NASA/Tom Bridgman

particles is pitch angle diffusion in the course of cyclotron resonant wave-particle interactions by whistler mode waves. Motivated by the work of *Inan et al.* [2003], the focus of this dissertation is on the determination of the antenna-plasma coupling for electric dipole antennas operating in the Earth's inner radiation belts. In particular, we explore the efficacy of using these antennas as wave-injection instruments with emphasis on the near field coupling.

## 1.2 Antenna-plasma Coupling

The coupling of an antenna embedded in a magnetized plasma to its environment induces qualitatively different behavior in a number of distinct regions as shown in Figure 1.2. Close to the antenna there exists a plasma sheath within which electrostatic effects are dominant and particle energization is significant, especially for large applied antenna voltages. The electromagnetic field energy in this region is primarily reactive. Beyond the sheath region, large amplitude electromagnetic waves

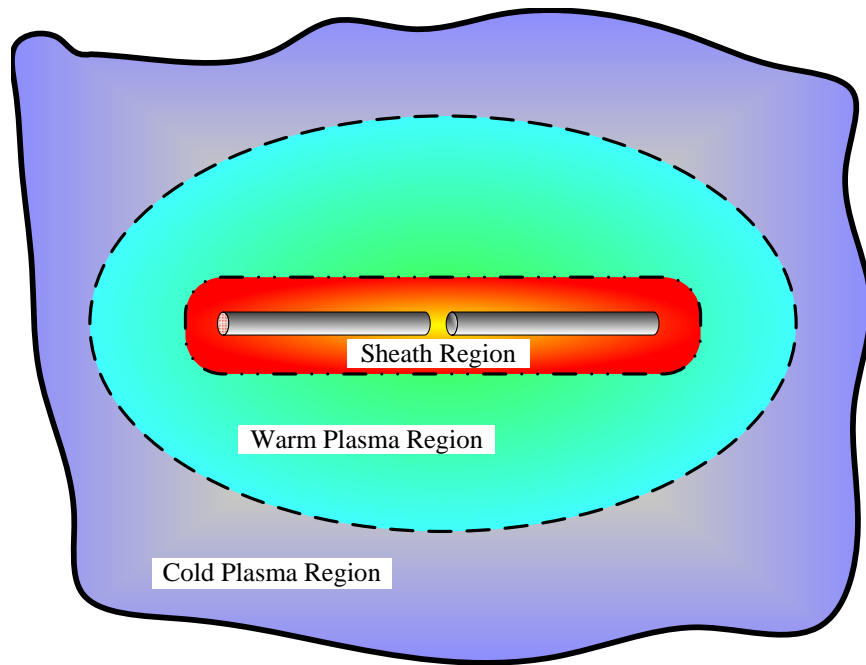


**Figure 1.2:** Conceptual diagram of antenna-plasma coupling regions.

produce strong currents with nonlinear effects still prevalent. This warm plasma region represents the transition region between the sheath region and the surrounding cold plasma region as shown in Figure 1.2. Beyond the warm plasma region, the electromagnetic waves are of a low enough intensity such that the electrodynamics of this region can be well described by a linear cold plasma treatment. The work presented in this dissertation focuses on the sheath region, which exhibits the most complex plasma behavior. As we show later, the adjacent regions can eventually be modeled by simplified versions of the numerical code developed to treat the sheath region.

Most related past work on the subject of near-field coupling of antennas in plasma falls into two distinct categories. The first category involves the characterization of dipole antennas operating in a linearized plasma regime for which the presence of the plasma sheath is neglected. These results are applicable to the cases in which the antenna is used either for receiving only or when the transmit drive voltages applied on the antenna are relatively small compared to the background plasma potential

given by the relation  $|q_e\Phi| \ll \frac{3}{2}k_B T$  where  $q_e$  is the *charge* of an electron,  $\Phi$  is the *potential*,  $k_B$  is *Boltzmann's constant* and  $T$  is the plasma *temperature*. The relation  $|q_e\Phi| \ll \frac{3}{2}k_B T$  simply states that the potential energy of the particle is less than the thermal energy. The second category involves the more general topic of sheath formation near conductive surfaces in a plasma which is not specific to antennas but is relevant to the work presented in this thesis. This category of work involves the more general area of the interaction of conducting bodies with their plasma environment. A brief synopsis of some of this past work in the context of the aforementioned categories is now discussed.

## 1.3 Antennas in Linearized Plasma Regimes

### 1.3.1 Theoretical Work

The coupling of antennas to a magnetized plasma has been an area of active research for decades. *Balmain* [1964] performed some of the first analytical studies concerning the behavior of electric dipole antennas in a cold magnetoplasma. Formulas for the input impedance of short cylindrical dipoles of arbitrary orientation with respect to the background magnetic field were derived using quasi-electrostatic theory assuming a lossy (i.e., collisional) plasma. The analysis was limited to electrically short antennas (relative to a free-space wavelength) so that the current distribution along the length of the antenna was assumed to be triangular. In addition, *Balmain* [1964] compares his theoretical results with experimental data for combinations of neon and argon plasmas, obtaining good agreement. A good review of the relevant literature during this period of time involving the status of antenna research for a variety of plasma environments and antenna types including dipole and loop antennas is provided by *Balmain* [1972] and *Balmain* [1979]. These review papers cover such topics as impedance, radiation, resonances and nonlinearities for both isotropic and anisotropic plasmas. However, up until the times of these reviews, only a few works were published on the treatment of antennas operating in a collisionless magnetoplasma at VLF frequencies. A series of papers were produced at Stanford on

this subject, including *Wang and Bell* [1969, 1970]; *Wang* [1970]; *Wang and Bell* [1972a,b,c]. All of these papers considered electrically small antennas, assuming that the current distribution on the antenna was triangular, and ignored any effects of the plasma sheath. Salient aspects of these works are described below.

*Wang and Bell* [1969] derived closed-form analytical expressions for the radiation resistance of electric dipole antennas operating in a cold magnetoplasma using a full-wave solution. The frequency range considered included whistler-mode frequencies (i.e., below the electron gyrofrequency) well above the Lower Hybrid Resonance (LHR) frequency denoted as  $f_{\text{LHR}}$ . Antenna orientations both parallel and perpendicular to the background magnetic field were considered in this work, assuming an electron-proton plasma. *Wang and Bell* [1970] extended their previous analysis to include the frequency range below  $f_{\text{LHR}}$  and calculate the radiation resistance for electric-dipole antennas of arbitrary orientation with respect to the background magnetic field. In addition to highlighting the fact that Balmain's electrostatic approximation [*Balmain*, 1964] is valid for frequencies well above  $f_{\text{LHR}}$ , *Wang and Bell* [1970] point out that this same electrostatic theory predicts an erroneous value of zero for the radiation resistance below  $f_{\text{LHR}}$ . Furthermore, they conclude that more power is radiated from a dipole antenna oriented perpendicular to the background magnetic field than for parallel orientations since the propagating modes launched from this orientation provide a much higher radiation resistance. The frequency range for which their full wave solution is valid for a 100 m antenna was determined to be  $f < 1.4f_{\text{LHR}}$  and  $f < 1.16f_{\text{LHR}}$  for magnetospheric locations corresponding to  $L=2$  and  $L=3$  respectively. In the same year, *Wang* [1970] provided closed-form formulas for the input impedance of VLF antennas operating in a magnetoplasma.

In following work, formulas for the radiation patterns of arbitrarily oriented electric and magnetic dipoles in a cold collisionless magnetoplasma were derived [*Wang and Bell*, 1972a]. Expressions for the power patterns were given as a function of driving frequency and magnetospheric location, which determines the local refractive index surface that governs wavelength and propagation direction. *Wang and Bell* [1972a] conclude in this work that the focusing of the radiation changes from the resonance cone direction (wave normal angle in a cold magnetized plasma for which the

refractive index approaches infinity) for frequencies that are a factor of 0.75 times the electron gyrofrequency  $f_{ce}$  to a pencil beam pattern focused along the static magnetic field for whistler mode frequencies in the range  $f \ll f_{ce}/2$ . Following their extensive cold plasma analysis, *Wang and Bell* [1972b] examine the radiation characteristics of an electric dipole at VLF frequencies in a linearized warm magnetoplasma by adding a finite electron temperature effect incorporated through the addition of a scalar pressure term in the cold plasma equations, a commonly used practice at the time [*Balmain*, 1979]. *Wang and Bell* [1972b] ignore the nonlinear sheath [*Bittencourt*, 2003, pages 279-288] in their formulation by assuming low voltage antenna operation and use a Fourier decomposition of the wave and plasma equations of motion to solve the resulting linear system. They assert that for frequencies above  $f_{LHR}$ , propagation characteristics may be significantly altered since the thermally modified whistler mode wave can propagate at angles beyond the resonance cone. For frequencies below  $f_{LHR}$  however, the refractive index surface is basically unmodified while noting radiation efficiencies for the perpendicular antenna greater than at least 10% over the parallel antenna for most cases.

During the same period, studies of whistler mode radiation patterns of electric dipole antennas in a laboratory setting were performed by *Stenzel* [1976] and more recently by *Amatucci et al.* [2005], providing some reassurance for the theoretical predictions of *Wang and Bell* [1972a]. Even with all of these advancements, the primary underlying assumption made in *Wang and Bell* [1969, 1970]; *Wang* [1970]; *Wang and Bell* [1972a,b,c] which remained to be verified, was that the current distribution along the length of the antenna was triangular. Some of the more recent analytical work performed on the subject is that of *Nikitin and Swenson* [2001] who studied the impedance characteristics of High Frequency (HF) electric dipole antennas operating in the collisional ionospheric conditions found at 100 km altitude. Though this work is not directly related to the collisionless magnetospheric environment considered herein, the conclusions drawn in this work are noteworthy. In this paper, a comparison of the input impedance of short dipole antennas was made between assumed triangular and exponential current distributions along the length of the antenna. As in the work of *Balmain* [1964], *Nikitin and Swenson* [2001] used a quasi-electrostatic approach

to determine the terminal properties for an antenna with orientation parallel to the static magnetic field. The impedance values in *Nikitin and Swenson* [2001] demonstrate good agreement with the results of *Balmain* [1964] for frequencies between the electron gyrofrequency and upper-hybrid frequency inclusive and demonstrate the relative insensitivity of the impedance results to the particular form of the current distribution. In a more recent paper by *Bell et al.* [2006], closed form solutions for the current distribution along an electric dipole antenna operating within the plasmasphere were derived, however, these formulas are constrained to a limited range of plasma parameters and antenna lengths.

### 1.3.2 Simulation Work

Simulation work involving antennas operating in a magnetized plasma is scarce, with *Ward et al.* [2005] constituting some of the first modeling attempts on the subject. In this paper, the authors use a warm plasma model to determine the terminal impedance of very short dipole antennas in a collisional ionospheric plasma using the Finite Difference Time Domain (FDTD) method but without an effective absorbing boundary condition. Their model assumes an incompressible Maxwellian fluid for the electrons using the first two moments of the Boltzmann equation for electrons only while the ions and neutrals are assumed to remain stationary. As in the case of *Wang and Bell* [1972b], a scalar pressure is assumed for the electrons. Current distributions and impedance values are determined for a 1 m linear antenna and results are compared once again to the electrostatic model of *Balmain* [1964] with good agreement. The authors circumvent undetermined boundary condition instabilities by stopping the simulations before reflections from the numerical space boundary could contaminate the solution results.

## 1.4 The Plasma Sheath Region

Whether operating as transmitting or receiving elements, electric dipole antennas in a magnetoplasma are surrounded by an electrostatic sheath. This sheath can

significantly alter the antenna properties (both near and far field) relative to those which would be in effect if the plasma remained uniform near the antenna surface. For receiving purposes, the sheath is on the order of a few Debye lengths and is well approximated by existing analytical theory. However, when used for transmit applications requiring the driving of the transmitting element at large voltages far in excess of the surrounding plasma potential, the sheath is highly nonlinear and its structure is generally not well known.

The analysis of plasma sheath formation and behavior is important in a number of disciplines where a conducting surface is in contact with a plasma. Such applications include plasma chambers, fusion reactors, semi-conductor processing, and the Earth's near-space environment. In the absence of an applied potential, a conductor rapidly absorbs electrons, the most mobile plasma species, forming a net negative charge on the conductor [Bittencourt, 2003, pages 280-281]. The induced negative potential bias prevents additional electrons from being absorbed, resulting in the formation of a region of positive space charge between the conducting surface and ambient plasma called the 'sheath'. Though there is still some debate on the actual definition of the sheath region [Franklin, 2004], this layer of non-neutrality exists in all plasma environments with boundaries, and its characteristics are governed in part by the species present, collisionality of the medium, and the presence (or not) of a static magnetic field. In addition, the structure of the sheath is further augmented through an applied potential on the conducting surface, as in the case of a transmitting antenna.

Since the pioneering work of *Langmuir* [1929] and later by *Bohm* [1949] which formed the basis of the sheath models found in most literature on the subject, there has been considerable work performed in the areas of theory, simulation and experiment, some of which is now discussed.

### 1.4.1 Sheaths Surrounding Electric Dipole Antennas

Early attempts at modeling the sheath effects on the terminal properties of dipole antennas include *Mlodnosky and Garriott* [1963] who used small signal analysis coupled with a fixed-capacitor analogy to derive closed-form expressions for the sheath radius,

capacitance and resistance of a VLF dipole antenna moving through an ionospheric plasma. *Shkarofsky* [1972] extended the analysis of *Mlodnosky and Garriott* [1963] to include large signal excitation and the effects of an induced electromotive force (emf) resulting from the drift motion of the antenna at orbit speed (i.e., due to  $\mathbf{v} \times \mathbf{B}_0$ ). The following year *Baker et al.* [1973], using the same linear theory, incorporated a DC bias into their model resulting from spacecraft charging between the antenna and the satellite body on which the antenna was mounted. *Mlodnosky and Garriott* [1963]; *Shkarofsky* [1972]; *Baker et al.* [1973] all used very crude first order approximations of the current and voltage on the antenna and greatly simplified the description of the sheath region through approximations such as uniform charge density and a simple exponential voltage dependence through the sheath. More recently, *Song et al.* [2007] used linearized fluid theory based upon that of *Shkarofsky* [1972] to analytically determine the terminal properties and sheath characteristics surrounding electrically short dipole antennas in the inner magnetosphere at large drive voltages relative to the ambient plasma potential. However, *Song et al.* [2007] ignored the ion current to the antenna, which is crucially important as we show in Chapter 6.

### 1.4.2 Sheath Waves

The study of High Frequency (HF) sheath waves has also received some attention in recent years. Both *Laurin et al.* [1989] and *Luttgen and Balmain* [1996] examined the dispersion relations for sheath waves propagating in a magnetized plasma between a planar conducting surface and the ambient plasma. The sheath in these cases was approximated as a vacuum gap with an abrupt sheath edge, while *Morin and Balmain* [1993] examined sheath waves between a wire and an ambient isotropic plasma by approximating the sheath region as a series of constant density steps.

### 1.4.3 Planar Sheaths and RF Discharges

More comprehensive theoretical modeling work has been performed in the areas of DC applied potentials and radio-frequency (RF) discharges in the context of planar

sheaths. Recent progress in this area utilizes some variant of the linearized hydrodynamic plasma description for each species based on the original work of *Bohm* [1949]. It has been pointed out by many authors that Bohm's original sheath model suffers from some major deficiencies such as singular field values in the plasma sheath transition region resulting from the zero-field condition in the plasma-sheath boundary layer [*Self*, 1963; *Godyak and Sternberg*, 1990b; *Riemann*, 1991; *Vandenberg et al.*, 1991; *Godyak and Sternberg*, 2002]. Each of these authors propose various modifications to the transition layer such as a non-zero electric field or enhancement of the ion injection rate into the sheath. Indeed most analytical models are essentially a matching scheme to link two distinct regions i.e., the sheath and presheath regions. The presheath is a region of quasi-neutrality in which ions are accelerated into the sheath region at the Bohm velocity [*Bittencourt*, 2003, page 288], providing the necessary condition for a stable sheath. The transition region which joins the sheath and presheath regions represents a theoretical layer which is the source of the mathematical discontinuities found in the original work of *Bohm* [1949].

Additional work has been performed in the area of RF sheaths. *Godyak and Sternberg* [1990a] developed a linearized hydrodynamic model of the plasma sheath valid for arbitrary collisionality in the frequency range  $\omega_{pi} < \omega < \omega_{pe}$  where  $\omega_{pi}$  is the ion plasma frequency and  $\omega_{pe}$  is the electron plasma frequency. *Morin and Balmain* [1991] developed a small signal RF sheath model for a spherical probe in the frequency domain, comparing both single step and continuous sheath profiles with good agreement relative to warm-plasma fluid and kinetic theory. In addition, *Lieberman* [1988, 1989] derive time average values for capacitance and voltage for RF sheaths using an extremely simplified fluid approximation. In general, analytical sheath models are only valid under the assumption that  $q\Phi/k_B T \ll 1$  where  $q$  is the *charge* of the particle,  $\Phi$  is the *potential*,  $T$  is the *temperature* and  $k_B$  is *Boltzmann's* constant. This assumption allows for an implicit linearization of the set of fluid equations providing the steady-state equilibrium distribution of the electrons within the sheath modified by the Boltzmann factor:  $n_e = n_0 \exp(-q_e \Phi/k_B T)$ , where  $n_e$  is the density variation of the electrons,  $n_0$  is the ambient density of the quasi-neutral bulk plasma, and the quantity  $\exp(-q_e \Phi/k_B T)$  is the *Boltzmann factor* for electrons.

A recent paper by *Franklin* [2003], which covers both early and recent modeling work, provides a review of relevant literature on the plasma sheath boundary region. This work considers collisional and collisionless plasmas and discusses the use of various boundary conditions on the conducting surface and plasma-sheath transition region, including generalizations of the Bohm criteria for the steady state and time-dependent RF sheaths. Unfortunately, in many applications, theoretical models are usually insufficient for applied potentials that far exceed the plasma potential since the nonlinear terms cannot be neglected when using fluid theory. In addition, analytical modeling work is not completely self-consistent, commonly neglecting the time-dependence of the system of equations by assuming linear plasma behavior. [*Franklin*, 2003].

#### 1.4.4 Numerical Simulation and Laboratory Work

When nonlinear behavior is prevalent and the simplifying assumptions underlying an analytical treatment are no longer justified, numerical simulation provides an invaluable tool for determination of antenna behavior in a plasma. Numerical methods generally fall into the categories of kinetic and fluid approaches.

*Cook and Katz* [1988], comparing both analytical results and those obtained from a multi-moment fluid model in a collisional plasma, examined the instability created in the sheath region from impact ionization with neutral atoms. The secondary plasma resulting from the ionization was created as a result of the large DC electric field with positively biased probes pulling electrons through the collisional sheath region.

More recent work in the area of fluid simulation includes *Wang and Wendt* [1999] who, using a two moment multi-fluid one-dimensional simulation, point out the weakness of the Child-Langmuir law for collisionless and weakly collisional plasmas. *Wang and Wendt* [1999] highlight the sensitivity and dependence of sheath thickness on the electric field and space charge density located at the sheath edge in the context of low pressure, high density plasmas. In addition, *Wang and Wendt* [1999] truncate their system of moment equations with an assumption of isotropic pressure and utilize Poisson's equations to solve for the quasi-electrostatic fields. The system is iterated in

time until a steady-state convergence is reached. Recommendations for an adaptation to the original work of *Bohm* [1949] are cited in this work.

*Baboolal* [2002] used a finite-difference method following a similar one-dimensional two-moment fluid approach and truncated their system using the well known adiabatic relation  $p_\alpha n_\alpha^{-\gamma_\alpha}$  to solve for the time-dependent steady-state sheath for both finite and semi-infinite spaces. Particle injection, which is essential for a ‘stable’ sheath, is provided by a non-zero electric field boundary condition in the case of the semi-infinite space.

*Roy et al.* [2003] and *Kumar and Roy* [2005] use a Finite-Element Method (FEM) based drift diffusion model to solve for sheath formation governed by DC and RF driven discharges from electrodes in a non-magnetized plasma. As is discussed later, the collisional closure relations used in drift diffusion models are more easily justified for highly collisional plasmas than for collisionless environments. Highly collisional fluid moment methods such as the drift-diffusion models can be derived from a Chapman-Enskog type procedure [*Chapman and Cowling*, 1970] which performs a series expansion in Knudson number assuming quick relaxation to thermodynamic equilibrium. This procedure is discussed in more detail in the following section. *Roy et al.* [2003] includes the conservation of energy equation and compare their results with the work of *Godyak and Sternberg* [1990a], showing good agreement.

In recent years, the need to understand the behavior of semi-conductor devices at a microscopic level has led to various simulation works using hydrodynamic approaches. Though the emphasis is not necessarily focused on sheath dynamics, sheaths are certainly present in these calculations. Semi-conductor simulations typically employ a fluid treatment using moments of the Boltzmann equation with closure mechanisms based upon the principle of maximum entropy [*Trovato and Falsaperla*, 1998; *Anile et al.*, 2000b,a]. *Trovato and Falsaperla* [1998], *Anile et al.* [2000b] and *Anile et al.* [2000a] all use a three-moment approach incorporating some form of the energy equation and heat flux component with results that compare favorably with a Monte-Carlo analysis.

Particle In Cell (PIC) codes are used when wave-particle interactions are of interest since a fluid code by its nature cannot, in general, properly describe the influence of

single particles. In a fluid approach, this individual particle motion is averaged out into collective behavior. A number of authors have examined the sheath dynamics and related phenomena using a PIC approach. *Procassini et al.* [1990] examined the formation of an electrostatic sheath in the presence of a floating conducting wall using a PIC approach and compared it with early analytical work using the Boltzmann relation for electrons. Good agreement was obtained between the PIC simulation and analytical results for large ion-electron mass ratios.

Time-dependent sheath dynamics resulting from both positive and negative step function voltage changes on an electrode in a collisionless non-magnetized plasma were also studied for both cylindrically and spherically symmetric geometries [*Calder and Laframboise*, 1990; *Calder et al.*, 1993]. The magnitude of the drive potentials used in *Calder and Laframboise* [1990] and *Calder et al.* [1993] were on the order of  $10^3$  times the background plasma potential. Langmuir oscillations amplified by the electron-ion two-stream instability were evident in these simulations, which as noted in *Calder and Laframboise* [1990] can also be treated with a fluid description. However it was also suggested by *Calder and Laframboise* [1990] that plasma ringing exists due to the abrupt voltage changes which can affect the transient current collection on the electrodes for many plasma periods that cannot be accounted for in a fluid treatment. A similar analysis was made by *Borovsky* [1988] using a PIC approach in which he varied the potential on the electrode and noted the plasma ringing effects which were also amplified by the electron-ion two-stream instability.

Fluid models have successfully been applied to the sheath problem with good comparisons with PIC techniques. Some of the most pertinent works was in relation to the recent Space Power Experiments Aboard Rockets (SPEAR) program. This work includes *Ma and Schunk* [1989, 1992a,b] and *Thiemann et al.* [1992], who used a two-moment fluid analysis to study the temporal evolution of particle fluxes on high-voltage spheres in a collisionless non-magnetized plasma noting abrupt changes to the current collection as a result of the initial sheath formation. For large negative voltages, *Ma and Schunk* [1992a] and *Thiemann et al.* [1992] were able to reproduce the transient plasma ringing found in earlier PIC codes such as *Borovsky* [1988]; *Calder*

and Laframboise [1990] and Thiemann *et al.* [1992] (who performed a PIC-fluid comparison). Labrunie *et al.* [2004] performed a comparison between a one-dimensional Vlasov-Poisson kinetic simulation and a three-moment fluid code by studying ion-acoustic waves in a collisionless plasma. These authors highlight that fluid codes, even in the collisionless limit, can be very accurate, provided that certain conditions are met. The most relevant of these conditions is that the characteristic speeds of the phenomena of interest are not on the same order as the particle thermal velocities in which Landau damping is of concern. However, even in this velocity range, Landau damping has been treated using a fluid model by Goswami *et al.* [2005] in the context of magnetohydrodynamics (MHD) equations in the collisionless limit.

In addition to the earlier work of Stenzel [1976] involving whistler-mode antenna patterns, there have been recent laboratory experiments performed in the area of sheath formation and impedance calculations. For instance, Stenzel [1988] examined the plasma sheath resonance in a collisionless laboratory plasma and noted that this resonance became unstable for large applied potentials resulting from the negative differential resistance across the sheath region. Blackwell *et al.* [2005] and Walker *et al.* [2006] determined the sheath thickness and terminal impedance of small spherical probes immersed in a laboratory plasma.

### 1.4.5 Hydrodynamic Closure Relations

In general, closure relations in the collisionless limit based upon moments of the Vlasov equation are more difficult to justify than those derived from moments of the Boltzmann equation for which collisions are dominant. The problems arise due to the fact that the collisional operator in the Boltzmann equation, which is assumed to dominate particle dynamics, allows for the relaxation of the distribution function back to a state of thermal equilibrium faster than the time scales of interest. With the exception of the heat flux moment and beyond, each moment up to and including the pressure/energy moment assume some sort of symmetry in the distribution function. As such, most antenna work to date, whether analytical in nature or involving

simulation techniques, has focused primarily on highly collisional plasmas where various simplifying assumptions such as linearity of the medium or an isotropic pressure tensor are often times valid and used in conjunction with small signal analysis.

In a collisionless plasma on the other hand, a strong magnetic field can often times play a similar role as collisions, as noted by *Chew et al.* [1956], in one of the first works to examine the validity of the fluid approximation in the collisionless limit. In the collisional case, truncation of the fluid moments is determined through an expansion in mean free path or Knudsen number of the collisional operator in the Boltzmann equation since it is this term which is assumed to dominate the particle dynamics [*Chapman and Cowling*, 1970]. This procedure, also called the Chapman-Enskog closure, treats any deviation from the Maxwell-Boltzmann distribution as a small scale perturbation. Convergence of the Chapman-Enskog approach in weakly ionized plasmas was further studied by *Furkal and Smolyakov* [2000] and *Bruno et al.* [2006] who considered both magnetized and non-magnetized plasmas.

Other expansions have also been used, including those for distributions consisting of a non-Maxwellian high-energy tail. This high-energy tail is due to a large percentage of particles in the distribution function having velocities greater than the thermal velocity. For instance, *Salat* [1975] performed an expansion of the Fokker-Planck equation in powers of the ratio of flow and thermal velocities to provide the collisional/viscous components of the pressure and heat flux tensors. For a collisionless plasma however, it is the Lorentz force that is dominant. Using this fact, *Chew et al.* [1956] expanded the Boltzmann equation in powers of the Larmor radius, noting that the Larmor frequency provides the dominant frequency of the system in the case of a strong magnetic field. This expansion is essentially a statement of adiabaticity of the system, providing the well known Chew-Goldberger-Low (CGL) laws that are put forth in that work. Many authors have provided extensions to the work of *Chew et al.* [1956], including *Barakat and Schunk* [1982a,b] for anisotropic velocity distributions resulting from different temperatures parallel and perpendicular to the static background magnetic field.

Closure relations for the pressure and heat flux moments, developed by *Barakat and Schunk* [1982a,b], were based upon the magnitude of the temperature anisotropy

and by utilizing a bi-Maxwellian distribution, exploiting perpendicular and parallel symmetries of the problem that were loosely justified *Chust and Belmont* [2006]. *Chust and Belmont* [2006], which include the works of *Ramos* [2003, 2005], provide some of the most comprehensive justifications for closure relations in a collisionless plasma for the pressure and heat-flux tensors. The paper treats closure mechanisms based on the roles of adiabaticity both parallel and perpendicular to the magnetic field, gyrotopry, non-adiabatic closures, and the relative importance of temporal and spatial variations on the phenomena of interest. In addition, *Chust and Belmont* [2006] and references therein provide regions of validity and state that the CGL laws only apply in the case where the phase velocity of the waves is much greater than the thermal velocity of the particles, i.e., the condition of zero heat flux. As stated previously, it is the region where the phase velocity is on the order of the particle thermal velocity which is of concern, since this is the area where wave particle interactions (including mechanisms such as Landau damping) occur that may or may not be treatable with a fluid approach as discussed in *Chust and Belmont* [2006].

With the recent work of *Chust and Belmont* [2006] providing additional validation for the collisionless fluid approach with respect to our antenna-sheath problem, we have developed both electrostatic and electromagnetic simulation tools to examine the dynamics of the collisionless sheath and antenna terminal characteristics therein using a two-species plasma fluid formulation. The antennas of interest here are located at magnetospheric points corresponding to  $L=2$  and  $L=3$  where the plasma consists of a fully-ionized electron-proton plasma. Our simulation tool (i.e., the AIP code) utilizes both Finite-Difference (FD) and Finite-Volume (FV) methods with the electrostatic and electromagnetic fields provided through solution of Poisson's and Maxwell's equations respectively. Whereas past work has primarily involved the study of antennas using linear analysis, or in the case of the sheath formation has considered only DC potentials applied to two-dimensional symmetric geometries, we extend this past analysis to include AC applied potentials and three-dimensional geometries using fully nonlinear formulations. This dissertation thus presents significant contributions to the advancement of knowledge in the area of antenna-plasma coupling, most notably in the area of sheath dynamics surrounding electric dipole

antennas.

## 1.5 Thesis Organization

The work presented in this thesis is organized as follows.

Chapter 1, the present chapter, introduces the motivation for this work and provides a discussion of relevant background material and past work related to antennas operating in a plasma.

In Chapter 2, the theoretical background is provided for the fluid approach based on taking successive moments of the Vlasov equation. We address the concept of closure as it relates to our  $N$ -moment fluid system concerning sheath dynamics and discuss potential problems with the use of a fluid approach versus a fully kinetic model in the context of instabilities, wave-particle interactions and particle trapping, along with resolutions of these issues.

We begin Chapter 3 with a discussion of our initial simulation development which includes a linearized cold plasma electromagnetic model. In this chapter, numerical absorbing boundary condition instabilities are discussed as well as methods to circumvent such issues.

In Chapter 4, we apply the cold plasma model developed in Chapter 3 to determine the current distribution and terminal impedance of a 100 m long dipole antenna in the absence of a plasma sheath.

In Chapter 5, we extend the capability of our cold plasma model by including non-linear and finite temperature effects. In this warm plasma formulation, we substitute Maxwell's equations with Poisson's equation to ease the computational burden and to avoid problems associated with the electromagnetic boundary conditions discussed in Chapter 3. This Chapter also provides the theoretical background for the model used to simulate the quasi-electrostatic sheath formation surrounding electric dipole antennas discussed in Chapter 6.

In Chapter 6, we compare our fluid model with existing analytical results for the one-dimensional steady-state sheath formation adjacent to a floating electrode. We then proceed to compare the role of various truncation schemes on the current-voltage

relationship on an infinite cylindrical antenna placed in a two-dimensional space. Two whistler-mode frequencies are considered in this case with simulations that include both magnetized and non-magnetized plasma environments in the presence of time-varying potential functions far exceeding the background plasma potential. A comparison of truncation schemes based on the two-moment isothermal approximation (isotropic pressure tensor) and three-moment adiabatic approximation (negligible heat flux) is provided. We conclude Chapter 6 with three-dimensional simulations of sheath formation surrounding a 20 m dipole antenna using our validated fluid model. The terminal properties of the antenna for the aforementioned cases are given for the electric dipole and a discussion of the relative importance of various fluid quantities is given in relation to the time-varying sheath formation.

Chapter 7 summarizes the results presented in Chapters 4 and 6 and concludes with a discussion of future extensions of the work presented in this dissertation.

## 1.6 Scientific Contributions

The contributions to knowledge presented in this dissertation are as follows:

- Developed fully parallel 3-D finite-difference time-domain (FDTD) and finite-difference frequency-domain (FDFD) codes for the simulation of electromagnetic waves in cold magnetized plasmas with arbitrary material boundaries.
- Applied the FDFD code to determine the current distribution and terminal impedance of an electric dipole antenna in the inner magnetosphere.
- Developed a fully parallel 3-D nonlinear multi-moment hydrodynamic code for the simulation of electrostatic sheath formation in warm unbounded collisionless magnetized plasmas.
- Applied the nonlinear fluid code to determine the effects of the plasma sheath on the near field characteristics of electric dipole antennas.

# Chapter 2

## Derivation of Hydrodynamic Moment Method

### 2.1 Theoretical Formulation

Our fluid formulation uses a macroscopic multi-fluid approach to solve for the non-linear sheath dynamics. The fluid model is comprised of moments of the Vlasov equation  $\mathcal{F}_v$  for each particle species, representing the time-evolution of the distribution function  $f=f(\mathbf{r}, \mathbf{v}, t)$  in a collisionless plasma where  $\mathbf{r}$ ,  $\mathbf{v}$  and  $t$  are coordinates in *configuration* space, *velocity* space and *time* respectively. The Vlasov equation is given by Equation 2.1.

$$\mathcal{F}_v(\mathbf{v}, \mathbf{r}, t) = \frac{\partial f}{\partial t} + (\mathbf{v} \cdot \nabla_{\mathbf{r}})f + \left[ \frac{\mathbf{F}}{m} \cdot \nabla_{\mathbf{v}} \right] f = 0 \quad (2.1)$$

where  $m$  is the *mass*, and  $\mathbf{F}=q(\mathbf{E}+\mathbf{v} \times \mathbf{B})$  is the Lorentz force with *charge*  $q$ , *velocity* vector  $\mathbf{v}$ , *electric* field  $\mathbf{E}$  and *magnetic* field  $\mathbf{B}$ . Since the bulk of the plasma between  $L=2$  and  $L=3$  is virtually cold ( $\sim 2000^\circ$  K) consisting of very low energy particles [Bezrukikh *et al.*, 2003], we assume that our initial distribution for each species is a Maxwellian distribution as in Calder and Laframboise [1990] and Calder *et al.* [1993]. In a three-dimensional Cartesian coordinate system, this distribution is given by Equation 2.2.

$$\mathbf{f}_m(\mathbf{v}) = n_0 \left( \frac{m}{2\pi k_B T} \right)^{\frac{3}{2}} e^{-mv^2/(2k_B T)} \quad (2.2)$$

$$v = |\mathbf{v}| = \sqrt{(v_x - v_{x0})^2 + (v_y - v_{y0})^2 + (v_z - v_{z0})^2}$$

where  $n_0$  is the bulk density,  $v$  is the magnitude of the velocity vector represented by coordinates  $v_x$ ,  $v_y$  and  $v_z$  in velocity space,  $v_{x0}$ ,  $v_{y0}$  and  $v_{z0}$  are the drift velocities in their respective directions,  $k_B$  is Boltzmann's constant, and  $T$  is temperature. In our simulations, we assume that the drift velocities  $v_{x0}$ ,  $v_{y0}$  and  $v_{z0}$  are initially zero; however as discussed in Section 5.3, these drifts are important in deriving the fluid boundary conditions at the surface of the antenna.

### 2.1.1 Moments of the Vlasov Equation

The series of moments that comprise our fluid model are derived by multiplying each term in the Vlasov equation by powers of  $\mathbf{v}$  and then integrating the resultant equation over all velocity space. In many cases including ours, it is convenient to define the second and third order moments which specify the stress tensor  $\mathbf{\Pi}$  and energy flux density  $\mathcal{E}$  in the rest frame of the species using the relation  $\mathbf{c} = \mathbf{v} - \mathbf{u}$ , where  $\mathbf{c}$  is the random velocity due to the thermal motions of the particles,  $\mathbf{u}$  is the bulk flow velocity, and  $\mathbf{v}$  is the velocity distribution of the particles in phase space as defined earlier. In the rest frame,  $\mathbf{\Pi}$  and  $\mathcal{E}$  become the pressure  $\mathbf{P}$  and heat flux density  $\mathbf{Q}$ , which are integrated with respect to the Vlasov equation in powers of  $[\mathbf{v} - \mathbf{u}]^N$ . The  $N^{\text{th}}$  moment  $\mathbf{M}$  of the Vlasov equation is defined as follows:

$$\mathbf{M}^{N^{\text{th}}} = \iiint_{\mathbf{v}} \begin{cases} m\mathcal{F}_v(\mathbf{v})d\mathbf{v} \\ m\mathbf{v}\mathcal{F}_v(\mathbf{v})d\mathbf{v} \\ m[\mathbf{v} - \mathbf{u}][\mathbf{v} - \mathbf{u}]\mathcal{F}_v(\mathbf{v} - \mathbf{u})d(\mathbf{v} - \mathbf{u}) \\ m[\mathbf{v} - \mathbf{u}][\mathbf{v} - \mathbf{u}][\mathbf{v} - \mathbf{u}]\mathcal{F}_v(\mathbf{v} - \mathbf{u})d(\mathbf{v} - \mathbf{u}) \end{cases} \quad (2.3)$$

The fluid transport model comprising the first four moments given by Equations

2.4a-2.4d (which are found in *Chust and Belmont* [2006]) correspond to *density, momentum, pressure, and heat-flux* respectively:

$$\partial_t(nm) + \nabla \cdot (nm\mathbf{u}) = 0 \quad (2.4a)$$

$$\partial_t(nm\mathbf{u}) + \nabla \cdot (nm\mathbf{u}\mathbf{u} + \mathbf{P}) - nq(\mathbf{E} + \mathbf{u} \times \mathbf{B}) = 0 \quad (2.4b)$$

$$\partial_t(\mathbf{P}) + \nabla \cdot (\mathbf{u}\mathbf{P} + \mathbf{Q}) + \{\mathbf{P} \cdot \nabla(\mathbf{u}) + \boldsymbol{\Omega}_c \times \mathbf{P}\}^{\text{sym}} = 0 \quad (2.4c)$$

$$\partial_t(\mathbf{Q}) + \nabla \cdot (\mathbf{v}\mathbf{Q} + \mathbf{R}) + \left\{ \mathbf{Q} \cdot \nabla(\mathbf{u}) + \boldsymbol{\Omega}_c \times \mathbf{Q} - \mathbf{P} \nabla \cdot (\mathbf{P}) \frac{1}{nm} \right\}^{\text{sym}} = 0 \quad (2.4d)$$

In Equations 2.4c and 2.4d,  $\boldsymbol{\Omega}_c$  and  $\mathbf{R}$  represent the *gyrofrequency* vector along the magnetic field and the 4<sup>th</sup> order moment respectively, while the superscript ‘sym’ denotes a symmetric tensor. It is useful to note that with each moment, the rank of each tensor increases by  $x^N$  where  $x$  is the number of dimensions and  $N$  is the order of the moment. Therefore, the density equation for each species comprises only a single element, while the heat-flux tensor, which is of rank three, consists of 27 individual elements. The rapid increase in the number of equations can render the fluid moment method intractable unless simplifying assumptions are made for higher moments. The form of the tensors representing velocity, pressure, heat-flux and the 4<sup>th</sup> order moment  $\mathbf{R}$  in a Cartesian coordinate system are given by Equations A.1-A.4 found in Appendix A.

As stated previously, each additional moment included in the fluid description allows for the corresponding property of the distribution function to vary in both space and time during the evolution of the simulation, allowing for a more complete description of the plasma. Although the hydrodynamic description of the plasma is not specific to a particular distribution function, each moment has a particular meaning, based on the form of the distribution function. Figure 2.1 describes the first few transport properties for a plasma that is initially in the thermodynamic equilibrium state described by the Maxwellian distribution of Equation 2.2.

The 0<sup>th</sup> moment as shown in Figure 2.1a allows for the number density within each cell to vary, while the 1<sup>st</sup> moment allows for the Maxwellian distribution to possess a non-zero average drift velocity  $\mathbf{u}$ . The next three moments correspond to the width,

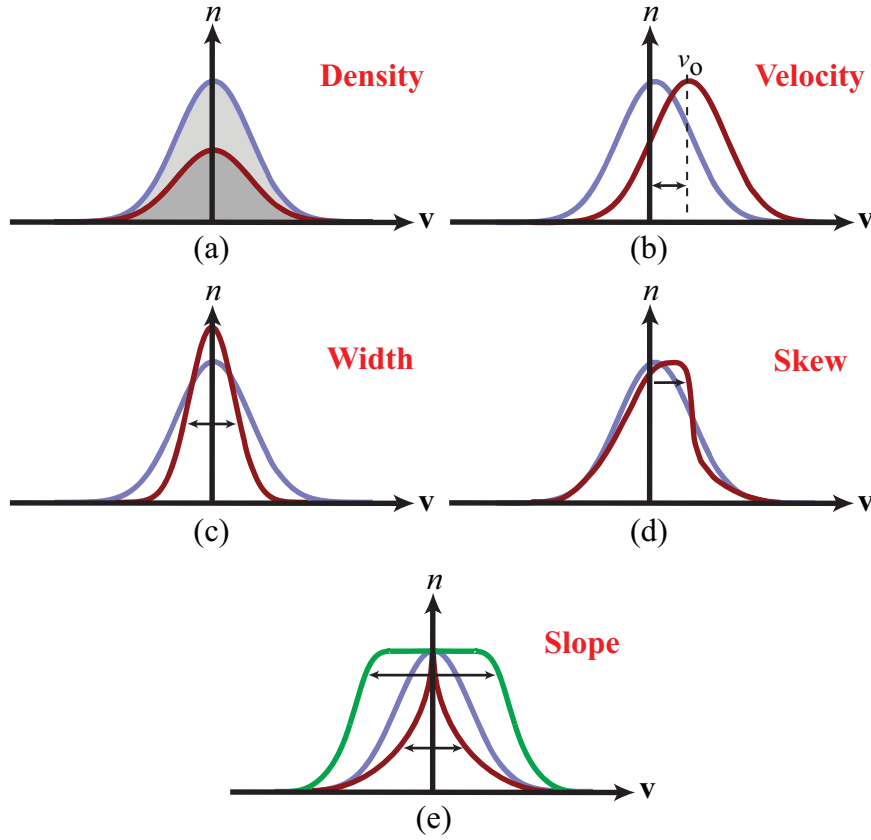


**Figure 2.1:** Transport properties for Maxwellian distribution function. (a)  $0^{\text{th}}$  moment  $n \equiv$  total number density. (b)  $1^{\text{st}}$  moment  $\mathbf{v} \equiv$  average fluid velocity. (c)  $2^{\text{nd}}$  moment  $\mathbf{P} \equiv$  width of distribution. (d)  $3^{\text{rd}}$  moment  $\mathbf{Q} \equiv$  skew of distribution. (e)  $4^{\text{th}}$  moment  $\mathbf{R} \equiv$  slope or inflection of distribution.

skew, and slope of the distribution respectively as shown in Figures 2.1c - 2.1e. As can be seen from Figure 2.1, the even moments correspond to an even symmetry about the local mean of the distribution while the odd moments possess an odd symmetry about this point; this behavior is simply a result of the assumed Maxwellian being an even distribution.

There are four different closure relations that are used in this dissertation. The first closure relation is the cold plasma approximation given by Equations 2.4a and 2.4b which assumes that the pressure tensor  $\mathbf{P}$  is identically zero. Furthermore, if we assume small signal analysis, Equations 2.4a and 2.4b can be linearized and combined

into a single auxiliary current equation. This process and the corresponding model are discussed in Chapter 3. The cold plasma approximation does not allow for the formation of the sheath since the linearization of the equations assumes that the density is only a small perturbation from the ambient value; however, it is useful in the determination of the antenna current distribution and subsequent code validation, as discussed in Chapter 4.

The last three closure relations include all temperature and nonlinear terms in the system of moments, allowing for the sheath to develop. These closure relations are collectively denoted as the warm plasma approximation. The second closure relation (or the first warm plasma relation) is based upon the ideal gas law which provides a relationship between temperature and pressure given by  $\mathbf{P} = nk_B \mathbf{T}$  where  $\mathbf{T}$  is a diagonal tensor describing the temperatures parallel and perpendicular to the background magnetic field. This relation is the equation of state based on the ideal gas law for thermodynamics and provides a mechanism for truncating the infinite set of moments at the momentum equation assuming a diagonal pressure tensor. For the case in which the temperatures parallel and perpendicular to the background magnetic field are the same (isothermal),  $\mathbf{P}$  simplifies to a scalar representing isotropic pressure.

The third closure relation (or the second warm plasma relation) utilizes the assumption of adiabaticity  $\nabla \cdot \mathbf{Q} = 0$ , which essentially means that the contribution due to the heat-flux is negligible (i.e., no heat transfer); however, all components of the pressure tensor are kept in the fluid description. In a collisional plasma, the off-diagonal elements of the pressure tensor are associated with viscous and shearing forces resulting from collisions, whereas in a collisionless plasma, these same viscous forces are due to velocity gradients and the presence of a magnetic field, as seen from Equation 2.4c.

The final closure relation considered is that which is involved with truncating at the heat-flux moment. In this case, our closure relation is based on an assumption concerning the next highest moment  $\mathbf{R}$  in Equation 2.4d. We follow the example of *Chust and Belmont* [2006] in this case, and assume that each element of the tensor  $\mathbf{R}$  is given by  $r_{\alpha\beta\gamma\kappa}$  and satisfies the relation  $r_{\alpha\beta\gamma\kappa} = p_{\alpha\beta} p_{\gamma\kappa} / (nm)$ , where  $p$  are elements of the *pressure* tensor,  $n$  is the local *number density*,  $m$  is *mass* and  $\alpha, \beta, \gamma$  and  $\kappa$

are indices which span the dimensions  $\hat{x}$ ,  $\hat{y}$ , and  $\hat{z}$ . This assumption, as with all other closure relations given, is equivalent to assuming that the distribution function remains sufficiently compact and symmetric about the mean (thermal velocity) so that the first few moments provide an adequate description of the distribution. In fact, up until the addition of the heat-flux moment, which allows for skew about the mean velocity in the distribution, all other moments assume a symmetry about the mean velocity, which in the case of a warm plasma, would be the thermal velocity.

In Chapters 5 and 6 of this dissertation, we develop the warm plasma models and compare results of the various truncation relations through simulation for both magnetized and unmagnetized plasmas in the context of sheath formation. This comparison allows us to verify the applicability of our simulation tool since the regions of validity of the fluid approach as applied to sheath formation are not readily apparent, as outlined in *Chust and Belmont* [2006]. *Chust and Belmont* [2006] provide an analytical justification of the fluid approach based on various time and spatial scales for the various truncation mechanisms for velocities either above or below the thermal velocity, for which wave-particle interactions such as Landau damping may be of concern, as discussed in Chapter 1. However, since there is the potential for waves to exist for which the phase velocity spans the thermal velocity range during the sheath formation process, such a concise analytical solution as presented in *Chust and Belmont* [2006] is not easily justifiable.

## 2.2 Instabilities and Resonances

Though the fluid model can provide a very accurate description of plasma behavior over a wide range of conditions, there are some phenomena for which a fluid description is inadequate. These phenomena are usually associated with wave-particle interactions, since the behavior of individual particles is not taken into account as they would be, for example, in PIC method. We now address the potential importance of such effects in our sheath simulations.

### 2.2.1 Two-Stream Instability and Landau Damping

In the simulations of *Borovsky* [1988], *Calder and Laframboise* [1990], *Ma and Schunk* [1992a], *Thiemann et al.* [1992] and *Calder et al.* [1993], it was seen that transient electron plasma oscillations formed during the initial step response of the system to the high voltage excitation on spherical electrodes, when using both PIC and fluid approaches. *Calder and Laframboise* [1990] additionally noted that these same large plasma ringing effects were driven to large amplitude by the ion-electron two-stream instability, which they stated that a fluid code can capture. *Calder et al.* [1993] observed that this instability was present only in simulations of positively stepped electrodes, since for negatively stepped potentials, the electrons were completely evacuated from the sheath region due to their much higher mobility. The ions left inside the sheath had no electrons with which to interact and thus the instability could not develop. For the case of a positive applied potential, the ions are not fully depleted from the sheath region since they are much heavier.

The same PIC simulations suggested that Landau damping was also negligible since the phase velocity of Langmuir modes is much larger than particle thermal velocity [*Calder and Laframboise*, 1990]. Later, *Thiemann et al.* [1992] determined that not only could a two-moment fluid code reproduce the oscillation in general character, but that some of the oscillations present in the PIC code were due in large part to numerical noise resulting from under-sampling the particle distribution function, an inherent problem in large-scale PIC codes. The same fluid code was also able to capture the formation of a double layer during the initial phase of the sheath formation, resulting from the mass exodus of ions from the sheath region for large positive DC applied potentials.

The remaining question is whether or not the electron-electron two stream instability is present during sheath formation since a fluid code cannot capture this instability. Counter-streaming electrons in a macroscopic fluid element would average each other out and simply enhance the local electron density. On the other hand, an electron-electron two-stream instability has not been observed in any PIC plasma sheath simulations that we are aware of, including those referenced herein. This result is perhaps due to the symmetry of the cases considered. Directly counter-streaming

electrons would only interact from opposing sides of the sheath, in which case they would hit the conductor and be absorbed. Any electrons that do not collide with the antenna surface would have their trajectories randomized, most notably in the case of an ambient magnetic field, and would therefore not satisfy the condition for a two-stream electron-electron instability.

### 2.2.2 Particle Trapping and Secondary Emission

The effect of particle trapping in the sheath region surrounding high voltage conductors has been previously studied [*Parker and Murphy*, 1967; *Palmadesso*, 1989]. *Parker and Murphy* [1967] used theoretical arguments involving conservation of energy and angular momentum to derive a closed form solution for the radius in which electron trapping would occur for DC applied potentials surrounding spherical electrodes in a magnetic field. The radius for which this effect is important is called the Parker-Murphy radius  $R_{\text{pm}}$  taken from *Palmadesso* [1989] and is equal to:

$$R_{\text{pm}} = R_0 \left[ 1 + \sqrt{\frac{8q_e \Phi_0}{m_\alpha \Omega_\alpha^2 R_0^2}} \right]^{\frac{1}{2}} \quad (2.5)$$

where  $R_0$  is the *radius* of the spherical electrode,  $q_e$  is the *charge* of an electron,  $\Phi_0$  is the *potential* on the electrode, and  $m_\alpha$  and  $\Omega_\alpha$  are the *mass* and magnitude of the *cyclotron* frequency for the trapped particle of species  $\alpha$  respectively. Using the theoretical work of *Parker and Murphy* [1967], *Palmadesso* [1989] suggested on these grounds that trapping would potentially be important to the overall structure of the sheath if a substantial volume of the sheath lay outside of the Parker-Murphy radius. Thus, trapping would be significant for kilovolt DC applied voltages such as those found in the SPEAR experiments. However, in the PIC simulations of *Calder et al.* [1993] involving large DC applied potentials applied to electrodes, it was shown that it is really only the positive ions that are trapped as a result of biasing the electrode rapidly. The electrons would not be trapped since they would have comparable orbits with the ions in the steady state fields when their energies are equivalent, despite the large ion-electron mass ratio. Therefore, since we consider cases in which the

potential on the antenna is slowly varying at VLF frequencies, we would not expect particle trapping to be of concern.

Secondary emission of electrons occurs when a conductor is biased to a high negative voltage for which ions accelerated to high energies impact the surface of the conductor, and kick off secondary electrons. *Cluggish and Munson* [1998] studied secondary emission in the context of plasma source ion implantation, a commonly used technique in the semiconductor industry for doping semiconductors. These studies were performed using collisional plasmas with comparisons between fluid simulation and experiment in which secondary emissions could potentially ionize the background plasma. Directly related to our studies is the work of *Franklin and Han* [1988] who analyzed the beam-plasma instability formed within the collisionless plasma-sheath due to secondary emission from a conducting wall using a PIC technique. The PIC simulations of *Franklin and Han* [1988] revealed that for the high temperature collisionless plasmas considered, the plasma oscillations that were produced, limited the growth of the instability. Only under strong current carrying conditions would the beam-plasma instability greatly modify the plasma within the sheath and potentially trap additional particles.

For the case of a thin wire antenna in three-dimensions, the secondary emission effect would be much less pronounced since the actual surface area over which secondary electrons sputter from the antenna elements is very small compared to the conductor surface area in the one-dimensional PIC simulations of *Franklin and Han* [1988]. In addition, the radial symmetry of the antenna geometry provides further evidence against the formation of a beam which would excite the instability. We do not include secondary emission effects in our current model, but discuss this topic in Chapter 7 as a future extension of the current work.

# Chapter 3

## Cold Plasma Electromagnetic Model

In this chapter, we cover the initial development of our Antenna-In-Plasma (AIP) simulation tool beginning with the linear cold plasma approximation. Our simulation tool involves a full wave solution of Maxwell's equations in a linearized magnetized plasma environment using finite-difference time-domain (FDTD) and finite-difference frequency-domain (FDFD) techniques, the details of which are discussed herein.

### 3.1 Cold Plasma Simulation Development

The radiation pattern and efficiency of an antenna is directly related to the distribution of currents flowing along its surface. For electrically short dipole antennas operating in a free-space environment, the current distribution is known to be triangular [*Kraus*, 1988, pages 40-42]. For an antenna operating in a magnetoplasma however, the situation is more complex with possible wavelengths for a single excitation frequency that can cover a range of several orders of magnitude as a result of the high anisotropy of the medium.

In this dissertation, we make no assumptions about the form of the current distribution as in the work of *Wang and Bell* [1969, 1970] and *Wang* [1970]. Instead, the current distribution and the terminal properties of the antenna are determined

through simulation in a fully self-consistent manner. Since past analytical formulations are only valid for simple dipole geometries in a linear environment, we use numerical methods which are not subject to these constraints. Our numerical approach allows for a relatively straightforward extension into regimes for which there are no analytical solutions, such as inhomogeneous plasmas or more complex antenna designs.

FDFD is the frequency-domain counterpart of the well established FDTD technique [Taflove and Hagness, 2000]. Although literature on the application of FDFD to wave propagation in a magnetoplasma is scarce, there have been several applications of the FDTD method to the subject of wave propagation through a plasma, which are directly applicable to simulation using the FDFD method. The flexibility and generality of the FDTD method accounts for its acceptance as the method of choice for electromagnetic wave interaction within complex media [Taflove and Hagness, 2000]. As it pertains to the study of plasmas, Cummer [1997] provides a detailed comparison of the methods used to date; however, the works mentioned therein deal strictly with isotropic plasmas. Lee and Kalluri [1999] address the problem of electromagnetic wave propagation inside a cold magnetoplasma using FDTD but do not address the application of Absorbing Boundary Conditions (ABCs) for the reflection-free absorption of outgoing waves. In this chapter, we show that ABCs are one of the most difficult and pervasive issues underlying the simulation of electromagnetic wave propagation in a magnetoplasma.

Since the introduction of the Perfectly Matched Layer (PML) [Berenger, 1994], it has been used extensively in the field of computational electromagnetics due to its superiority over other types of ABCs. The PML, however, suffers from instabilities in the presence of some anisotropic media, such as orthotropic materials as discussed in *Becache et al.* [2003]. As demonstrated in *Becache et al.* [2003], this instability is not unique to a particular system of equations; rather, it is inherent in all PML derivations since they share the same underlying structure. In this chapter, we show that this numerical instability is present within the context of magnetized plasma simulations that need to be used to solve Maxwell's equations with a PML boundary condition. In addition, this instability is independent of the method used for the

plasma dynamics or the type of time integration scheme used. Thus, PIC, fluid, time and frequency domain methods are all affected by the presence of this numerical instability.

The purpose of this chapter is to demonstrate the complexity involved in numerically modeling the near field properties of electric dipole antennas operating in a cold, collisionless magnetized plasma, specifically emphasizing some of the numerical challenges in connection with PML boundary conditions and wave propagation in such media. In Chapter 4, we present comparisons of the results of our simulations with available analytical results for both current distribution and input impedance, in order to assess the validity of the assumptions made in past analytical work.

## 3.2 Theoretical Formulation

We mentioned in the beginning of the chapter that both time and frequency domain methods (FDTD and FDFD) are incorporated into our AIP simulation tool. For time-domain simulations, once a particular discretization technique is chosen to solve for the spatial derivatives in Maxwell's equations, the resulting set of equations can be represented by a system of ordinary differential equations (ODE)s represented by Equation 3.1:

$$\frac{d\bar{\mathbf{U}}}{dt} = \mathcal{F}(\bar{\mathbf{U}}) \quad (3.1)$$

where  $\bar{\mathbf{U}}$  represents a vector containing the electric and magnetic fields and  $\mathcal{F}$  represents the vector of spatial derivatives and source terms with all differential operators evaluated using a technique such as finite-differences or finite-volumes. With  $\mathcal{F}$  known, Equation 3.1 can be evaluated using one of many numerical time-integration methods including the staggered leapfrog method, backward differencing, or a class of Runge-Kutta methods. In addition to the original staggered leapfrog method used by Yee [1966] for the solution of Equation 3.1, we have also implemented both explicit and implicit Runge-Kutta methods into our simulation tool, the details of which are

discussed in Appendix B. However, for reasons that become clear later in this chapter, the cold plasma results presented in this dissertation use the frequency domain method FDFD.

The cold plasma description we use for our FDFD modeling combines the first two linearized moments of Vlasov's equation coupled with Maxwell's equations. The final system of equations representing our cold plasma model is given by Equations 3.2a-3.2c:

$$\nabla \times \mathbf{H} = \sum_N \mathbf{J}_\alpha + \epsilon_0 \frac{d\mathbf{E}}{dt} \quad (3.2a)$$

$$\nabla \times \mathbf{E} = -\mu_0 \frac{d\mathbf{H}}{dt} \quad (3.2b)$$

$$\frac{d\mathbf{J}_\alpha}{dt} + \nu_\alpha \mathbf{J}_\alpha = \frac{q_\alpha}{m_\alpha} (q_\alpha n_\alpha \mathbf{E} + \mathbf{J}_\alpha \times \mathbf{B}_0) \quad (3.2c)$$

where  $\mathbf{E}$  and  $\mathbf{H}$  are the wave *electric* and *magnetic* fields,  $\mathbf{J}$ ,  $\nu$ ,  $n$ ,  $q$ , and  $m$  are the *current density*, *collision frequency*, *number density*, *charge*, and *mass* of species  $\alpha$ . Equation 3.2c represents a simplified version of the generalized Ohm's Law [*Bittencourt*, 2003, pages 229-233].

For the purpose of the present work, the dipole antennas considered are taken to be located near the magnetic equatorial plane at  $L=2$  and  $L=3$ . The plasma in this region is fully ionized and is largely composed of protons and electrons. At  $L=2$ , the number density and magnetic field strength are taken to be  $n = 2 \times 10^9 \text{ m}^{-3}$  and  $B_0 = 3.931 \times 10^{-6} \text{ T}$ , with corresponding plasma and gyrofrequencies equal to  $f_{pe} = 401 \text{ kHz}$  and  $f_{ce} = 110 \text{ kHz}$  [*Carpenter and Anderson*, 1992]. At  $L=3$ , the plasma parameters are  $n = 1 \times 10^9 \text{ m}^{-3}$  and  $B_0 = 1.165 \times 10^{-6} \text{ T}$  providing  $f_{pe} = 284 \text{ kHz}$  and  $f_{ce} = 32.6 \text{ kHz}$  respectively. Since the number density of each species at these locations is relatively low, the plasma is entirely collisionless.

## 3.3 Simulation Properties

### 3.3.1 Computational Mesh Setup

The numerical mesh used for the cold electromagnetic plasma simulation is based on the traditional staggered/interleaved FDTD mesh for locations of electric and magnetic fields [Yee, 1966]. The currents described by Equation 3.2c are spatially colocated with their electric field counterparts. Care must be taken in the placement of the components of the current  $\mathbf{J}$ . Recent papers on the subject such as *Lee and Kalluri* [1999] propose colocating all components of the currents at the corner of the electric field Yee cell. However, such positioning of the currents produces spurious electrostatic waves, which possess a spatial wavelength on the order of the mesh cell size. Such numerical waves are a result of the spatial averaging of the currents and are explained as follows.

Referring to Figure 3.1, which represents the computational grid of *Lee and Kalluri* [1999], the locations of the electric fields are 1/2 cell width away from the corresponding components of the current density  $\mathbf{J}$  described by Equation 3.2c.

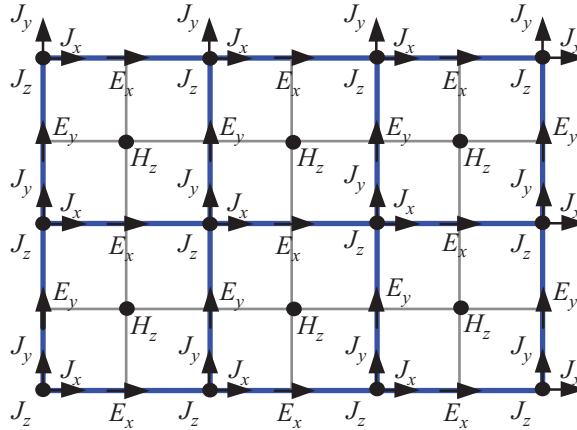


**Figure 3.1:** Two-dimensional mesh of Lee and Kalluri

Spatial averaging of a field value is necessary when the field quantity at a given location on the computational mesh is desired but not available. For instance, the update equation for the electric field described by Equation 3.2a requires values of

the current density  $\mathbf{J}$ . Because the components of  $\mathbf{J}$  are not colocated with the corresponding components of electric field on the mesh, a suitable average must be made, i.e., averaging  $J_x$  at the location of  $E_x$ . The same type of process holds true for the current density update equations presented by Equation 3.2c. Removing all references to time, the grid of *Lee and Kalluri* [1999] requires the averaging given by Equations 3.3a-3.3c in order to spatially colocate the electric field components of  $\mathbf{E}$  with the corresponding component of the current density  $\mathbf{J}$  given by Equation 3.2c.

$$E_x |_{J_x} = \frac{1}{2} \left( E_x |_{i+\frac{1}{2},j,k} + E_x |_{i-\frac{1}{2},j,k} \right) \quad (3.3a)$$

$$E_y |_{J_y} = \frac{1}{2} \left( E_y |_{i,j+\frac{1}{2},k} + E_y |_{i,j-\frac{1}{2},k} \right) \quad (3.3b)$$

$$E_z |_{J_z} = \frac{1}{2} \left( E_z |_{i,j,k+\frac{1}{2}} + E_z |_{i,j,k-\frac{1}{2}} \right) \quad (3.3c)$$

For frequencies  $f$  such that  $f_{\text{LHR}} < f < f_{\text{ce}}$ , where  $f_{\text{LHR}}$  represents the Lower Hybrid Resonance frequency, propagation in directions orthogonal to the static magnetic field is not supported in a cold plasma. This fact is verified with reference to Figures 3.6a and 3.6b, and further discussed in Section 3.3.6. Using a Cartesian coordinate system and assuming a  $+\hat{z}$ -directed static magnetic field, any electric field components excited in the  $+\hat{x}$  or  $+\hat{y}$ -direction subsequently produce currents in that respective direction through the spatial averaging of Equation 3.3a. The recursive process of spatial averaging leads to nonphysical electrostatic waves (of numerical origin) which propagate in a direction orthogonal to the static magnetic field, as shown in Figure 3.2.

The formation of these nonphysical wave modes is most easily demonstrated in the time domain. As such, Figure 3.2 represents a one-dimensional time domain simulation showing the formation of nonphysical electrostatic waves resulting from the spatial averaging of Equation 3.3a. A 20 kHz sinusoidal  $E_x$  source is placed in the center of the space in Figure 3.2. The medium is a cold plasma with properties consistent with those found at  $L=2$ . The horizontal axis represents the  $\hat{x}$ -dimension, with a static magnetic field present in the  $+\hat{z}$ -direction. Since there are neither propagating nor evanescent wave modes supported in this scenario, we would expect

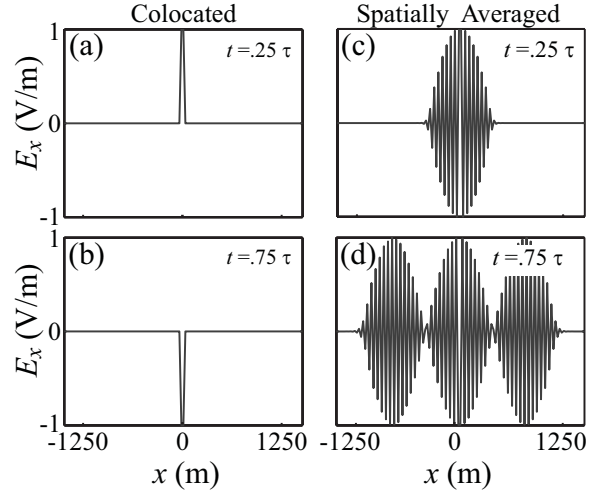


**Figure 3.2:** One-dimensional time domain simulation in cold plasma depicting nonphysical electrostatic wave formation on spatially averaged mesh vs. collocated mesh taken at times  $t = \frac{\tau}{4}$  and  $t = \frac{3\tau}{4}$  where  $\tau$  represents the period of a 20 kHz sine wave source. (a) Collocated E-field at time  $t = .25\tau$ . (b) Collocated E-field at time  $t = .75\tau$ . (c) Spatially averaged E-field at time  $t = .25\tau$ . (d) Spatially averaged E-field at time  $t = .75\tau$ .

to see only the source point oscillating in a sinusoidal fashion. Figure 3.2a and Figure 3.2b represent simulation snapshots at  $t = \tau/4$  and  $t = 3\tau/4$  (where  $\tau$  is the period of a 20 kHz wave) respectively for a mesh in which  $E_x$  is colocated with  $J_x$ . Figure 3.2c and Figure 3.2d represent a mesh in which  $E_x$  and  $J_x$  are staggered in space per Equation 3.3a. It is seen that the collocation of  $E_x$  and  $J_x$  found in Figures 3.2a and 3.2b correctly captures the physics (with only the source point oscillating in time) while the staggered mesh of Figures 3.2c and 3.2d produces an electrostatic wave (possessing no associated magnetic field) that propagates along the  $\hat{x}$ -direction. In fact, the only frequency range that supports electrostatic wave propagation in a cold plasma environment is that associated with the extraordinary mode. This mode is discussed in Section 3.3.6 in conjunction with the so-called Z-mode propagation branch. The Z-mode resides above the plasma frequency; a frequency well above the 20 kHz source, being 401 kHz at  $L=2$  in the equatorial plane. Thus, the oscillations seen in Figures 3.2c and 3.2d must be nonphysical in nature.

To prevent the formation of these non-physical waves, the components of current density  $\mathbf{J}$  for each species are colocated with their electric field counterpart as shown

in Figure 3.3 and applied to our FDFD formulation. Although our model utilizes spatial averaging, the averaging does not appear to create nonphysical modes.

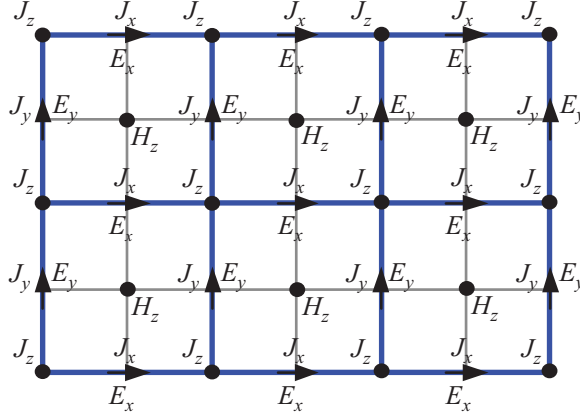


**Figure 3.3:** Two dimensional grid used in present model.

### 3.3.2 Frequency Domain Technique

The use of frequency domain techniques rather than those based on time integration (FDTD for instance) allows for the accurate modeling of spatial structures which are orders of magnitude smaller than a wavelength without an appreciable increase in computation time. This feature is a major advantage in our case, since the wavelengths for VLF waves below the electron gyrofrequency considered in this paper range from meters to megameters in the same simulation due to the high anisotropy of the refractive index. Refractive index surfaces are discussed later in Sections 3.3.5 and 3.3.6.

In order to speed up the software development cycle, we take advantage of pre-existing software libraries for some of the tasks involving numerical computation. Our model uses the PETSc (Portable Expression Template for Scientific Computing) framework *Balay et al.* [2001, 2004] for both its embedded parallelism and integrated linear and nonlinear solvers, which are integral parts of the frequency domain methods used. The code is parallelized using the Message Passing Interface (MPI). The FDFD technique solves for the sinusoidal steady state response of a single frequency

excitation. In order to solve our system of Equations 3.2a-3.2c, we must transform them into the frequency domain by substituting  $j\omega$  for the time derivative operator (i.e.,  $d/dt \leftrightarrow j\omega$ ) and by using complex phasor field quantities instead of time domain ones. This transformation results in the following set of equations:

$$\nabla \times \vec{H} = \sum_N \overleftrightarrow{\sigma}_\alpha \vec{E} + \epsilon_0 j\omega \vec{E} \quad (3.4a)$$

$$\nabla \times \vec{E} = -\mu_0 j\omega \vec{H} \quad (3.4b)$$

$$\overleftrightarrow{\sigma}_\alpha = \epsilon_0 \omega_p^2 (j\omega \mathbb{I} - \Omega)^{-1}$$

$$\Omega = \begin{bmatrix} -\nu & -\omega_{bz} & \omega_{by} \\ \omega_{bz} & -\nu & -\omega_{bx} \\ -\omega_{by} & \omega_{bx} & -\nu \end{bmatrix}$$

where  $\overleftrightarrow{\sigma}_\alpha$  represents the *conductivity* tensor in the relation  $\vec{J} = \sigma \vec{E}$  resulting from the transformation of Equation 3.2c into the frequency domain.  $\mathbb{I}$  represents the *identity* matrix, and  $\omega_b = \frac{|q_e B_0|}{m_e}$  is the electron *gyrofrequency* with corresponding  $\hat{x}$ ,  $\hat{y}$  and  $\hat{z}$ -components  $\omega_{bx}$ ,  $\omega_{by}$  and  $\omega_{bz}$ , where  $B_0$  represents the magnitude of the static *magnetic* field.

Frequency domain methods require a large complex matrix inversion. Normalization of the equations is especially important in avoiding an ill-conditioned system. Therefore, all dependent simulation variables such as length scales and field values are normalized into dimensionless quantities. Due to the size of the problem, the matrix is inverted using an iterative Krylov Subspace method in parallel [Demmel, 1997, pages 299-321]. The type of Krylov method used in this simulation is the Generalized Minimum Residual (GMRES) along with an Additive Schwarz (ASM) preconditioning matrix Balay *et al.* [2001, 2004].

### 3.3.3 Boundary Condition Instabilities

A variation of the PML originally proposed by *Berenger* [1994] is implemented in order to absorb electromagnetic radiation outgoing from the numerical space. The PML used in this paper is a frequency domain adaptation of the CPML (Convolutional PML) based on *Chevalier and Inan* [2004]. Since virtually all PML derivations begin with a frequency domain representation, the implementation of one in our FDFD model is straightforward.

Regardless of the PML type used, all PML derivations follow the same basic principle. This principle is to match the tangential component of the wave numbers at the computational/PML interface. This matching is then continued throughout the absorbing layers of the PML. Attenuation is realized with the addition of an artificial imaginary component of the wave normal vector  $\vec{k}$ . In most applications of computational electromagnetics, the PML accomplishes this task by absorbing the wave function in the direction orthogonal to the PML interface *Berenger* [1994].

Two recent papers that discuss issues with the PML related to our study are *Becache et al.* [2003] and *Cummer* [2004]. The work of *Becache et al.* [2003] highlights the fact that for a wave in which the group and phase velocities are antiparallel at the PML interface, the wave experiences exponential growth inside of the PML when the standard PML expressions are used. *Becache et al.* [2003] demonstrates this problem in orthotropic media, but do not present any recommendations as to the resolution of this dilemma.

The paper by *Cummer* [2004] examines the properties of a traditional PML in the presence of negative index of refraction materials. Within a material that possesses a negative index of refraction, antiparallel group and phase velocities are ubiquitous at a particular frequency within the computational space. This condition exists at all PML interfaces. In the case of *Cummer* [2004], a relatively simple fix (involving a simple switch in the sign of the exponent at different boundaries) is incorporated in the model to allow for proper absorption of outgoing waves. Unfortunately this method does not work in a magnetized plasma, since the switch of *Cummer* [2004] is only frequency dependent, while, as shown below, in a cold magnetized plasma, anti-parallel group and phase velocity behavior is both direction (i.e., k-vector) and

frequency dependent.

Using the stretched coordinate version of the PML first derived in *Chew and Weedon* [1994], we now show the manifestation of the PML region instability for a cold magnetized plasma. This instability is not just a cold plasma phenomena, but exists in any electromagnetic magnetoplasma model that utilizes a PML as an absorbing boundary condition.

### 3.3.4 PML Derivation

The derivation of the PML is well documented and can be found in numerous papers and books, including *Berenger* [1994] and *Taflove and Hagness* [2000]. A brief description of the PML suffices in order to illustrate the problem at hand. In a conventional stretched coordinate PML, the nabla operator used in Maxwell's equations is replaced by the nabla operator given by:

$$\tilde{\nabla} = \hat{x} \frac{1}{s_x} \frac{\partial}{\partial x} + \hat{y} \frac{1}{s_y} \frac{\partial}{\partial y} + \hat{z} \frac{1}{s_z} \frac{\partial}{\partial z} \quad (3.5)$$

where  $s_x$ ,  $s_y$ , and  $s_z$  denote *stretching* variables in their respective coordinate directions [*Chew and Weedon*, 1994]. The form of the stretching variable is given by:

$$s = \left( 1 + \frac{\alpha}{j\omega} \right) \quad (3.6)$$

where  $\omega$  represents radian frequency and  $\alpha$  describes an attenuation constant that exists only within the PML. Denoting the region inside the computational domain as *Region 1* and the interior of the PML as *Region 2*, and assuming plane wave solutions, the relationship between the wave numbers inside and outside the PML denoted by  $k_2$  and  $k_1$  respectively are given by:

$$k_2 = \left( 1 + \frac{\alpha}{j\omega} \right) k_1 \quad (3.7)$$

For simplicity, we assume a uniform plane wave in 1-D propagating in the  $+\hat{x}$ -direction. The wave number  $k_2$  admits plane wave solutions inside of the PML given by:

$$e^{-jk_{x1}(1+\alpha/(j\omega))x} \quad \text{or} \quad (3.8a)$$

$$e^{-jk_{x1}x} e^{-(\alpha k_{x1}/\omega)x} \quad (3.8b)$$

*Becache et al.* [2003] states that an instability develops if, for a given mode, the perpendicular components of the  $k$ -vector and group velocity vector  $\vec{v}_g$  are antiparallel at the entrance of the PML. This result can be ascertained by examination of the exponential attenuation term in Equation 3.8b. If a wave possesses a component of group velocity  $\vec{v}_g$  in the  $+\hat{x}$ -direction and component of  $\vec{k}$  in the  $-\hat{x}$ -direction, the fields exponentially grow inside the PML as opposed to the exponential decay as desired.

To illustrate this concept, we make use of the refractive index surfaces for propagation in both free-space and a cold magnetized plasma and discuss the differences in the context of the PML. The refractive index surface determines the relative directions of the group velocity  $\vec{v}_g$  and  $\vec{k}$  vectors.

### 3.3.5 PML in Free-space

In free-space, the refractive index surface is a sphere of unit radius and its cross section is shown as the circle surrounding the dipole antenna in Figure 3.4.

The  $k$ -vector represents the initial wave launched from the antenna and the group velocity direction is normal to the refractive index surface. It is readily seen from the free-space refractive index surface of Figure 3.4 that all components of the group velocity and  $k$ -vector are parallel within the medium and at the PML interface. According to *Becache et al.* [2003] and Equation 3.8b, this constitutes a stable system, with the wave attenuating inside the PML. However, in a magnetized plasma, the refractive index surface is highly anisotropic and thus dependent on the  $k$ -vector direction.

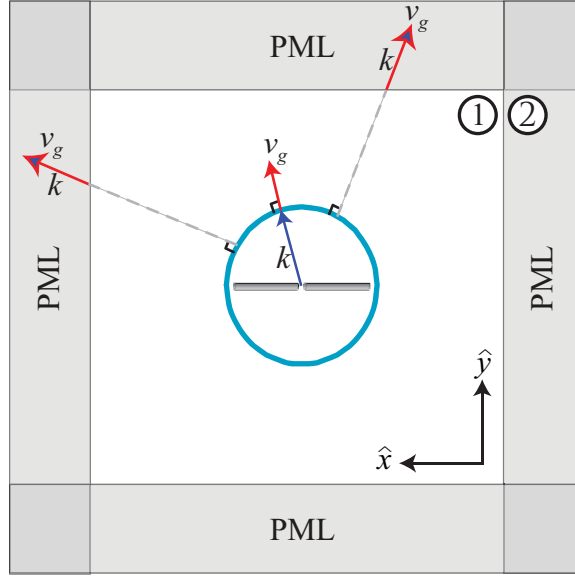


**Figure 3.4:** Free-space isotropic refractive index surface.

### 3.3.6 PML in the Whistler Mode

For the purpose of the present development, we are interested in waves with frequencies below the electron gyrofrequency, also known as whistler-mode waves. Characteristics of this propagation mode are illustrated by the dispersion diagrams of Figures 3.5a and 3.5b adapted from [Kivelson and Russell, 1995, pages 356-392] where Figure 3.5b represents an expanded region around  $f_{\text{LHR}}$ .

The LHR frequency in Figure 3.5b appears when ions are included in the cold plasma formulation. For the case when the ratio of electron plasma frequency to electron gyrofrequency is high, its value is approximately equal to [Stix, 1962, pages 30-32]:

$$f_{\text{LHR}} \simeq \sqrt{f_{\text{ce}} f_{\text{ci}}} \quad (3.9)$$

where  $f_{\text{ce}}$  and  $f_{\text{ci}}$  are the electron and ion *gyrofrequencies* respectively. It is important to note that all wave numbers less than zero in Figure 3.5a represent imaginary wave

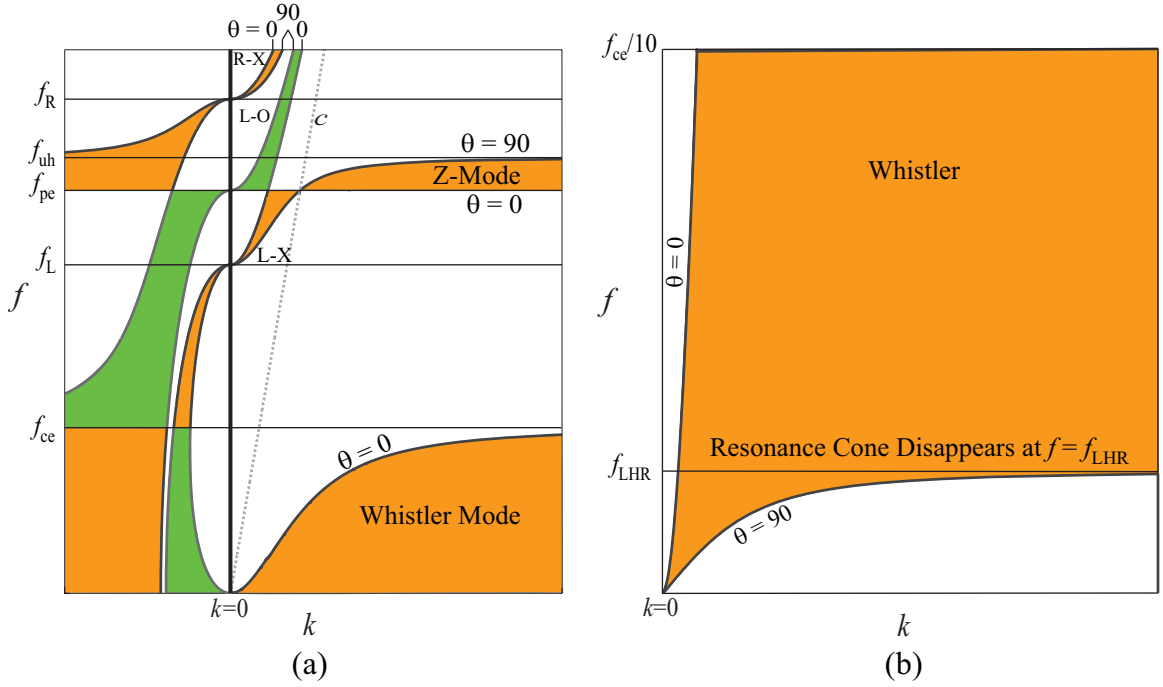


**Figure 3.5:** Cold plasma dispersion diagrams for  $f_{pe} > f_{ce}$  where  $\theta$  represents the propagation direction with respect to the background magnetic field.  $k > 0$  corresponds to the real part of the wave number.  $k < 0$  corresponds to the imaginary part of the wave number. R  $\equiv$  Right-handed mode. L  $\equiv$  Left-handed mode. O  $\equiv$  Ordinary mode. X  $\equiv$  Extraordinary mode.  $f_R \equiv$  Right-hand cutoff frequency.  $f_L \equiv$  Left-hand cutoff frequency.  $f_{uh} \equiv$  Upper hybrid frequency.  $f_{pe} \equiv$  Plasma frequency.  $f_{ce} \equiv$  Electron gyrofrequency. (a) Frequency range including evanescent modes. (b) Whistler-mode including Lower Hybrid Resonance (LHR) frequency.

numbers corresponding to evanescent modes, while those greater than zero represent propagating modes. Although we are mainly interested in whistler-mode propagation, the dispersion diagram of Figure 3.5a contains frequencies in the HF range including the Z-mode branch [Carpenter *et al.*, 2003] for completeness. Waves propagating in the Z-mode exhibit simultaneous electrostatic and electromagnetic behavior and, shown in Section 3.3.8, PML instabilities exist in this frequency range as well.

For frequencies between  $f_{LHR}$  and  $f_{ce}$ , wave propagation in directions orthogonal to the static magnetic field is not possible, and such wave energy is thus strictly evanescent. For  $f_{LHR} < f < f_{ce}$ , the resonance cone angle is defined as the angle between the direction orthogonal to the background magnetic field and the cone along which

the refractive index tends to infinity as shown in Figure 3.6a. Example refractive index surfaces for frequencies above and below the local LHR frequency are shown in Figures 3.6a and 3.6b where  $\vec{k}$  represents the *wave number*,  $\vec{v}_g$  is the *group velocity* or velocity of energy flow given by the normal to the refractive index surface, and  $\theta_{\text{res}}^*$  is the complement of the *resonance cone* angle discussed earlier.

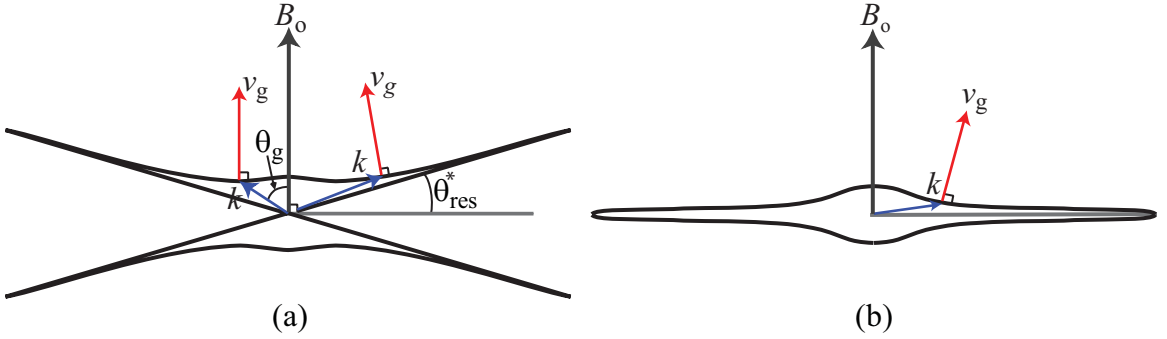


**Figure 3.6:** Whistler mode refractive index surfaces. (a)  $f_{\text{LHR}} < f < f_{\text{ce}}/2$ . (b)  $f_{\text{ci}} \ll f < f_{\text{LHR}}$ .

The refractive index surfaces depicted in Figures 3.6a and 3.6b are functions of the wave normal angle, defined as the angle between the  $k$ -vector direction and the ambient magnetic field. The Gendrin angle is the non-zero wave normal angle at which the group velocity is parallel with the static magnetic field [*Gendrin*, 1961]. The Gendrin angle  $\theta_g$  is illustrated in Figure 3.6a and for high ratios of ( $f_{\text{pe}}/f_{\text{ce}}$ ) is given approximately by the relation [*Gendrin*, 1961]:

$$\cos \theta_g \simeq \frac{2\omega}{\omega_{\text{ce}}} \quad (3.10)$$

where  $\omega$  and  $\omega_{\text{ce}}$  are the angular wave frequency and electron gyrofrequencies respectively. For angles  $\theta < \theta_g$  in an orthogonal coordinate system, all components of  $\vec{v}_g$  and  $\vec{k}$  are in the same relative direction. However, for wave normal angles beyond the Gendrin angle, i.e.,  $\theta > \theta_g$ , the components of  $\vec{v}_g$  and  $\vec{k}$  which are orthogonal to the static magnetic field are antiparallel when entering the PML as shown in Figure 3.7.

Whistler-mode waves with a wave normal angle greater than the Gendrin angle,

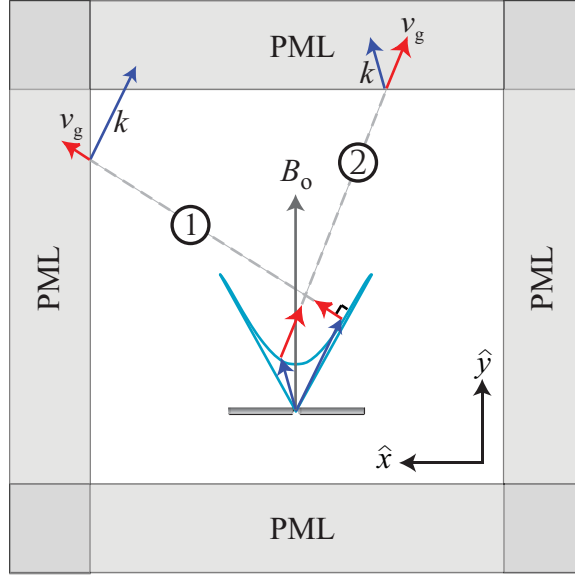


**Figure 3.7:** Unstable PML for whistler mode propagation.

such as the wave denoted by ‘1’ in Figure 3.7, exhibit exponential growth in the PML per Equation 3.8b. This growth occurs because the PML shown to be unstable in Figure 3.7 is designed to absorb waves with wave normals in the  $+\hat{x}$ -direction or waves of the form  $e^{-jk_1x}$ . Since the  $\hat{x}$ -component of  $\vec{k}$  is negative at the PML interface (and thus immediately inside it), the wave fields experience non-physical growth inside the PML. Wave ‘2’ is attenuated in the PML since the  $\hat{y}$ -components of  $\vec{k}$  and  $\vec{v}_g$  are parallel at the PML interface.

### 3.3.7 Solution to PML Instability in Whistler Mode

The negative index of refraction materials discussed by *Cummer* [2004] present a similar problem with antiparallel group and phase velocities, except in that case, the antiparallel group and phase velocity condition occurs at a particular frequency and is independent of the  $k$ -vector direction. Furthermore, in the case of the negative index of refraction materials, the group and phase velocity vectors are exactly antiparallel, i.e., are at 180-degrees with respect to one another. A simple frequency dependent adjustment to the stretching parameter of Equation 3.6 is all that is needed

to compensate for the PML instability. In a magnetized plasma, the situation is more complex with the group velocity and  $k$ -vectors being both frequency and direction dependent, and being at a finite angle (that is neither zero or 180-degrees) with respect to one another. Thus, the stretching parameter, in addition, must incorporate information about the  $k$ -vector direction. We have chosen to incorporate a specially adapted form of the PML which has been tailored to isolate and absorb evanescent modes in the directions orthogonal to the static magnetic field for frequencies  $f$  in the range  $f_{\text{LHR}} < f < f_{\text{ce}}$ . For  $f$ ,  $f_{\text{ci}} \ll f < f_{\text{LHR}}$  however, the aforementioned instability is not present. Though the refractive index surface of Figure 3.6b is highly anisotropic at these frequencies, for the PML surface alignment shown in Figure 3.7, there is no  $k$ -vector for which the directional components of  $\vec{k}$  and  $\vec{v}_g$  are antiparallel and thus a PML can be made to absorb both propagating and evanescent modes in this frequency range.

Numerical errors due to the reflection of propagating modes from the evanescent boundary conditions do not pose an issue for antennas oriented perpendicular to the static magnetic field at whistler-mode frequencies. For frequencies well below the electron gyrofrequency, the refractive index surface is virtually flat with the resonance cone angle being within a few degrees of the direction orthogonal to the static magnetic field. In this case, most of the wave energy is focused into the PML parallel to the static magnetic field and the evanescent modes are absorbed by the PML in the direction orthogonal to the static magnetic field.

A strictly evanescent PML can be realized by utilizing the formulation given in *Chevalier and Inan* [2004]. For simplicity, we only show the  $\hat{x}$ -component. From Equation 7 of *Chevalier and Inan* [2004], we have:

$$\nabla_{x_{\text{PML}}} = \left[ 1 - b_{x0} - \left( \sum_{n=1}^N \frac{b_{xn}\alpha_{xn}}{j\omega + \alpha_{xn}} \right) \right] \frac{\partial}{\partial x} \hat{a}_x \quad (3.11)$$

where  $\nabla_{x_{\text{PML}}}$  is the modified  $\nabla$  operator inside the PML,  $b_{x0}$  is a factor which controls evanescent attenuation for non-propagating modes, and  $(b_{xn}\alpha_{xn}) / (j\omega + \alpha_{xn})$  are terms which control the attenuation of simultaneous propagating and evanescent

modes. Since the inclusion of any terms in the  $(b_{xn}\alpha_{xn}) / (j\omega + \alpha_{xn})$  sequence produces amplification inside of the PML orthogonal to the static magnetic field, these terms are removed. Thus, a strictly evanescent PML for the  $\hat{x}$ -direction is given by Equation 3.12:

$$\nabla_{x_{\text{PML}}} = [1 - b_{x0}] \frac{\partial}{\partial x} \hat{a}_x \quad (3.12)$$

where  $b_{x0}$  represents a *conductivity* profile which varies from 0 at the PML interface to 1 at the last PML layer in a low order polynomial fashion.

### 3.3.8 The Z-mode Instability

Analogous to the PML which amplifies waves in the whistler-mode, Z-mode wave propagation [Budden, 1985, page 84] for frequencies between the plasma frequency and upper hybrid frequency, as shown in Figure 3.5a, exhibits these same instabilities within the PML. Figure 3.8 illustrates this instability in conjunction with the Z-mode refractive index surface.

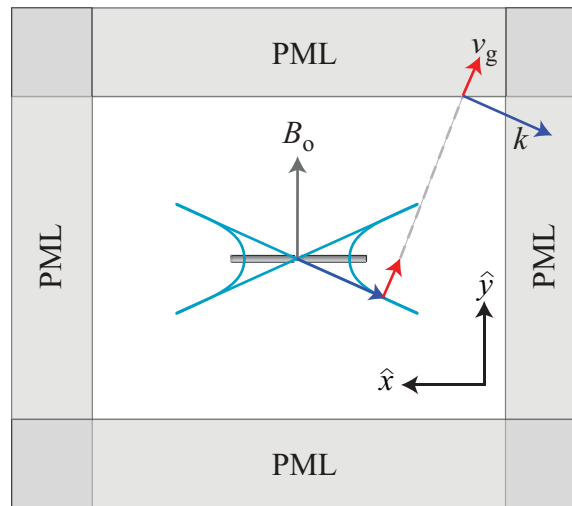


**Figure 3.8:** Unstable PML for Z-mode propagation.

It is seen from Figure 3.8 that the PML oriented perpendicular to the magnetic

field which attenuates waves at frequencies in the whistler-mode is now unstable for Z-mode propagation. An important benefit of the FDFD method is that it allows us to isolate a particular frequency of interest without exciting transients at other frequencies due to broadband numerical noise. These transients, which are fundamental characteristics of time domain simulations methods such as FDTD, result from the introduction of a source into a computational space with zero-field initial conditions. Regardless of the steady-state waveform function used, this initial transient is equivalent to a delta function (albeit small) which produces noise across the entire frequency spectrum. Since we are not concerned with propagation at these higher frequencies for our applications, this HF branch can be ignored. For time-domain simulation techniques such as FDTD, however, this issue would need to be specifically addressed and resolved as discussed in Appendix C.

# Chapter 4

## Current Distribution and Terminal Impedance

### 4.1 Simulation Setup

We now present results for the current distributions and input impedance of electric dipole antennas operating in a cold magnetized plasma obtained using the AIP code by neglecting the plasma sheath. The effects of the nonlinear sheath are addressed in Chapters 5 and 6. FDFD simulations are carried out for dipole antennas oriented perpendicular to the ambient static magnetic field. This orientation is chosen since the antenna pattern and power delivery are optimal for launching waves parallel to the static magnetic field [*Wang and Bell, 1972a,b*] which would in turn, optimally interact with energetic radiation belt particles. Antennas considered for the purpose of our application are on the order of 100 m in length and up to 20 cm in diameter. The placement of the antenna in the numerical space is shown in Figure 4.1.

The FDFD method is well suited to model geometries small compared to the free space wavelength. The antenna itself is assumed to be a PEC (Perfect Electric Conductor) and the current distribution along the length of the antenna is calculated by taking a line integral of the frequency domain magnetic field components encircling each wire element along the length of the antenna. The input impedance is calculated using Equation 4.1:

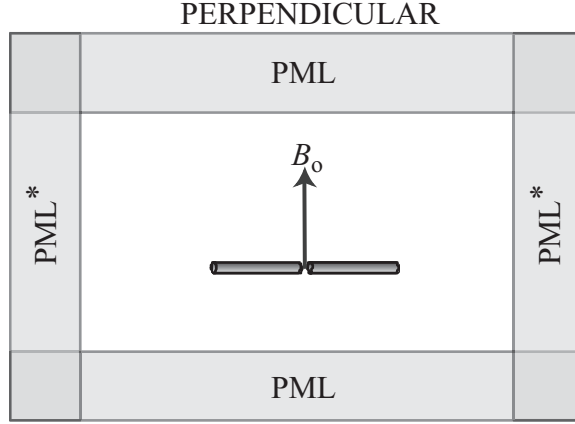


**Figure 4.1:** Computational domain for cold plasma simulations. The PML boundary conditions orthogonal to the magnetic field and denoted by PML\* are evanescent for  $f_{\text{LHR}} < f < f_{\text{ce}}$

$$\mathcal{Z}_{\text{in}} = \frac{\mathcal{V}(f)}{\mathcal{I}(f)} = \frac{(\int \vec{E} \cdot d\vec{l})_{\text{feed}}}{(\oint \vec{H} \cdot d\vec{l})_{\text{feed}}} \quad (4.1)$$

where the field quantities are already in the frequency domain per use of the FDFD method. Equation 4.1 represents the ratio of the complex phasor quantities for the current and voltage at the terminals of the antenna.

The computational grid used in our model is a non-uniform Cartesian mesh. For propagation at wave normal angles close to the resonance cone, the theoretical wavelength drops to zero in the cold plasma limit, and is thus not properly resolved on a mesh with finite cell size. As a consequence, waves propagating with wave normal angles close to the resonance cone realize wavelengths on the order of the mesh cell size regardless of the cell resolution.

With the inclusion of an antenna, however, it has been verified in our simulations that if the antenna is well resolved by the largest cell size used in the computational space (i.e., 30 cells over the length of the antenna), it is not necessary to realize zero-wavelengths using finite size cells. Thus, increasing the cell resolution beyond 30 cells does not adversely affect the impedance values since the waves dominating the energy flow are well resolved. This observation is supported by *Wang and Bell*

[1972a,b] who found that dipole antennas operating in a magnetized plasma environment preferentially radiate waves whose wavelength is of the order of the antenna length.

For the purposes of our simulation, we first examine the properties of a 100 m long electric dipole antenna in a cold magnetized plasma operating near  $L=2$  in the magnetic equatorial plane. We consider an electron-proton plasma with  $f_{pe} = 401$  kHz and  $f_{ce} = 110$  kHz in a collisionless environment. The computational meshes for a 100 m antenna are shown in Figure 4.2 representing the geometries for frequencies above and below  $f_{LHR}$ . The  $\hat{z}$ -directed antenna is located in the center of the space and is 20 cm in diameter which corresponds to the smallest cell size in the space. The magnetic field is oriented in the  $+\hat{y}$ -direction and a PML is used to truncate the space in all directions. The dipole antenna is excited with an  $E_z$  hard source [Taflove and Hagness, 2000, page 176] in the gap between the conducting elements with a value of 1 V/m and the system is allowed to converge with a relative residual norm of  $10^{-6}$ .

One of the primary benefits of using a frequency-domain method over time-domain analysis is the ability to use a different mesh and PML configuration for each simulation run. Though we do not use this advantage to the full extent available (a different configuration for each frequency), we do use a different mesh and PML configuration for frequencies below and above  $f_{LHR}$  for which the propagation characteristics are quite different, as previously shown in Figures 3.6a and 3.6b. For frequencies  $f > f_{LHR}$ , there exists a range of  $k$ -vectors for which the refractive index is very large and tends to infinity at the resonance cone angle  $\theta_{res}$  as shown in Figure 3.6a. It is therefore imperative to utilize much smaller cells in order to capture these tiny wavelengths resulting from the high refractive index relative to those used for frequencies  $f < f_{LHR}$  as shown in Figure 4.2. For frequencies below  $f_{LHR}$ , the resonance cone disappears as shown in Figure 3.6b with the refractive index surface being closed and possessing a maximum of  $\mu_r \simeq 600$  at directions orthogonal to the background magnetic field. The refractive index surface for  $f < f_{LHR}$  becomes more isotropic with decreasing frequency and thus larger cells sizes may be used as shown in Figure 4.2a. It is this difference in refractive index between the two frequency regimes that explains why the cell size along the  $\hat{z}$ -direction corresponding to the length of the antenna stays at a constant

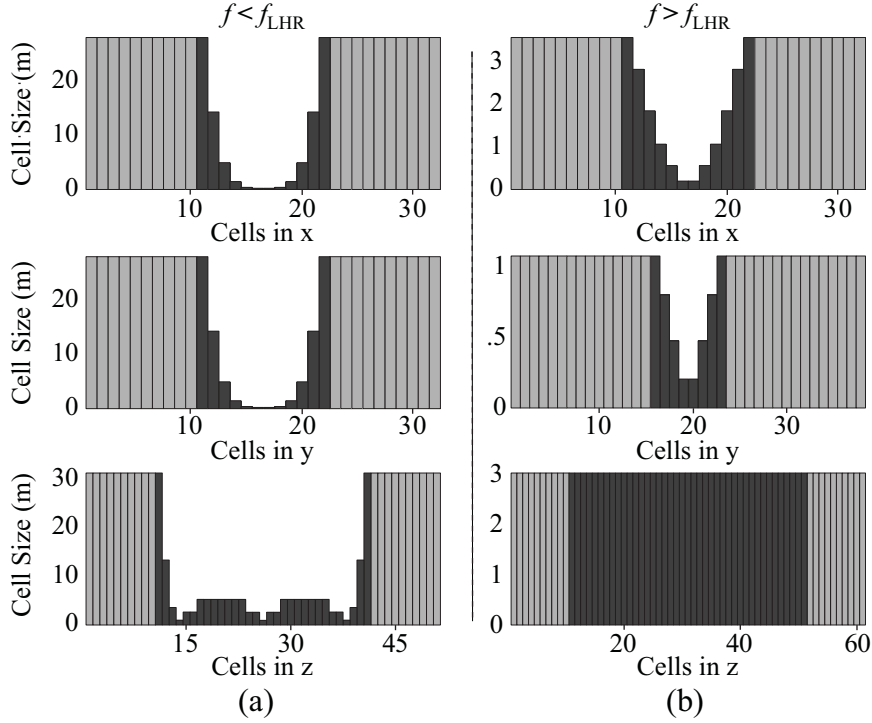


**Figure 4.2:** Variation in cell size along each of the principal directions for non-uniform mesh used in simulation at  $L=2$ . The dark gray cells correspond to those that are within the computational domain and the light gray cells correspond to the PML layers. (a) Frequencies below  $f_{LHR}$  with  $(\hat{x}, \hat{y}, \hat{z})$  dimensions  $32 \times 32 \times 51$ . (b) Frequencies above  $f_{LHR}$  with  $(\hat{x}, \hat{y}, \hat{z})$  dimensions  $32 \times 38 \times 61$ .

value of 3 m for  $f > f_{LHR}$  while the cell size is variable for  $f < f_{LHR}$ .

As with the computational mesh, the PML configuration used is also different for frequencies above and below  $f_{LHR}$ . For frequencies  $f > f_{LHR}$ , the PML consists of 10 cells in the  $\hat{x}$ -direction, 15 cells in the  $\hat{y}$ -direction, and 10 cells in the  $\hat{z}$ -direction. The PML layers in both the  $\hat{x}$  and  $\hat{z}$ -directions are made to absorb only evanescent waves, while the PML layers in the  $\hat{y}$ -direction absorb both propagating and evanescent waves in this frequency range. These layers, along with the computational mesh, are illustrated in Figure 4.2. For frequencies below  $f_{LHR}$ , there are 10 cells per PML layer in all directions and each PML is made to absorb both propagating and evanescent waves. The PML parameters are different for frequencies above and below  $f_{LHR}$  since the cell sizes and refractive index surfaces are quite different in the two cases. The

PML performance up to 10 kHz including frequencies above and below  $f_{\text{LHR}}$  for the simulations in the  $L=2$  environment are shown in Figure 4.3 corresponding to PML orientations parallel and perpendicular to the static magnetic field.

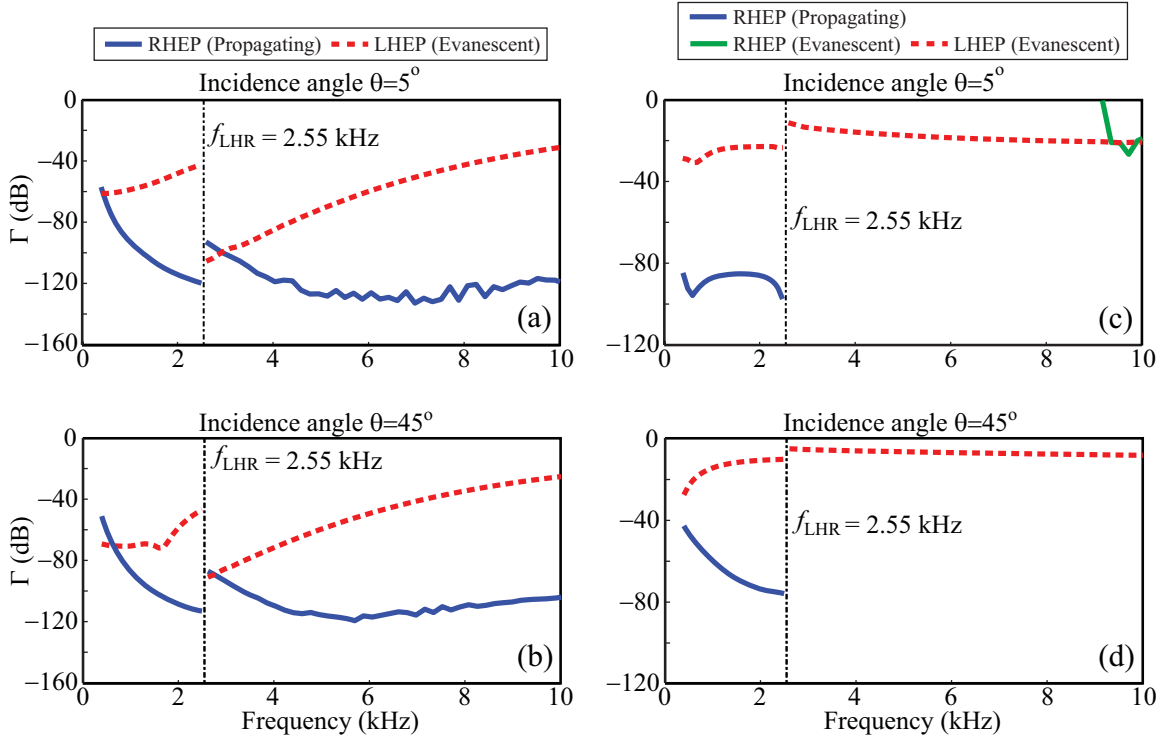


**Figure 4.3:** Reflection coefficient calculations for PML oriented both parallel and perpendicular to the static magnetic field, for angles of  $5^\circ$  and  $45^\circ$  with respect to normal incidence. RHEP and LHEP incident wave polarizations are shown including the performance for frequencies above and below  $f_{\text{LHR}}$ . (a) Parallel at  $5^\circ$  incidence. (b) Parallel at  $45^\circ$  incidence. (c) Perpendicular at  $5^\circ$  incidence. (d) Perpendicular at  $45^\circ$  incidence.

There are several things to notice about the plots in Figure 4.3. First of all, the only propagating modes in the frequency range  $f_{\text{ci}} \ll f < f_{\text{ce}}$  (where  $f_{\text{ci}} \ll f_{\text{LHR}}$ ) are right-hand elliptically-polarized (RHEP). All waves launched from the antenna that are left-hand elliptically-polarized (LHEP) are therefore evanescent in the plasma at these frequencies. The discontinuity in the reflection coefficient calculations at  $f_{\text{LHR}}$  is a direct result of the differences in mesh and PML geometries across this transition region as stated earlier. Though the PML performance for LHEP waves representing the directions orthogonal to the static magnetic field shown in Figures 4.3(c-d) is

relatively poor, being  $> -37$  dB across the frequency range shown, the reflected energy from these LHEP waves incident upon the PML parallel to the magnetic field is absorbed with greater attenuation as shown in Figures 4.3(a-b). As mentioned in Section 3.3.7, the PML in the direction orthogonal to the static magnetic field as represented in Figures 4.3(c-d) for frequencies  $f > f_{\text{LHR}}$  has been tailored to absorb evanescent waves only, so as to avoid the PML instabilities mentioned earlier. As a result, the incident RHEP propagating modes experience no attenuation and are perfectly reflected. Finally, there is a small section in Figure 4.3c in the range  $9.2 < f < 10$  kHz for which the incident RHEP wave is evanescent. The resonance cone angle of Figure 3.6a is  $5^\circ$  at  $\sim 9.2$  kHz and marks the point at which the incident RHEP waves become evanescent and are absorbed by this PML.

## 4.2 Antenna Current Distribution in Free-space

The derivation of the formula for the current distribution  $I(z)$  of a thin linear antenna in free-space is documented in many texts including that of [Kraus, 1988, page 219]:

$$I(z) = I_0 \sin \left[ \frac{2\pi}{\lambda} \left( \frac{\ell}{2} + z \right) \right] e^{j\omega t} \quad (4.2)$$

$$\frac{-\ell}{2} \leq z \leq \frac{\ell}{2}$$

where  $I_0$  is the peak magnitude of the *current*,  $\lambda$  is the *wavelength*,  $\ell$  is the *length* of the antenna,  $t$  is *time*,  $\omega$  is the driving *frequency* and  $z$  is the *distance* along the length of the antenna. It can be seen from Equation 4.2 that an antenna that is exactly  $\lambda/2$  in length exhibits a half wave current distribution over the length of the element. However, as the length of the antenna decreases to some fraction of a wavelength, the current distribution becomes more and more triangular in shape, as shown in Figure 4.4

At VLF wavelengths, antennas of  $\ell = 100$  m in length would be considered electrically short in free-space per Equation 4.2. Such has been the primary assumption in the works of *Balmain* [1964], *Wang and Bell* [1969], *Wang and Bell* [1970] and

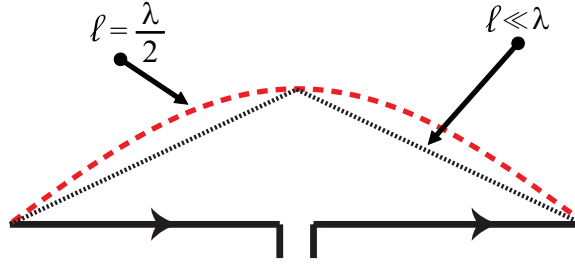


**Figure 4.4:** Current distributions for thin linear antenna.

*Wang* [1970] as well as other early theoretical formulations mentioned in Chapter 1. Although we show that this free-space approximation as applied to a magnetized plasma is valid for most cases considered in this dissertation, we present a few cases where this assumption breaks down, namely those of very long antennas and large electron number densities.

### 4.3 Current Distributions and Input Impedance Calculations for a 100 m Antenna at $L=2$

The first case study is a 100 m antenna located in the equatorial plane at  $L=2$ . Figure 4.5 represents the current distributions for frequencies above and below the local LHR frequency with  $f_{\text{LHR}}=2.55$  kHz.

It can be seen from Figures 4.5a-4.5d that the current distributions are virtually identical to the assumed triangular distribution of *Wang and Bell* [1969, 1970] and *Wang* [1970] for the frequency range considered. One important point is that for a simulated antenna of finite thickness, the current is non-zero at the ends, contrary to the ideal case, since the finite area allows for a build up of charge at the tips. The simulation results thus reflect this realistic condition much better than the idealized case shown in dashed lines.

The results from our AIP code represent the first self-consistent calculations of the current distribution along a short dipole antenna at VLF frequencies in a cold magnetoplasma, while making no assumptions as to the form of the current. These

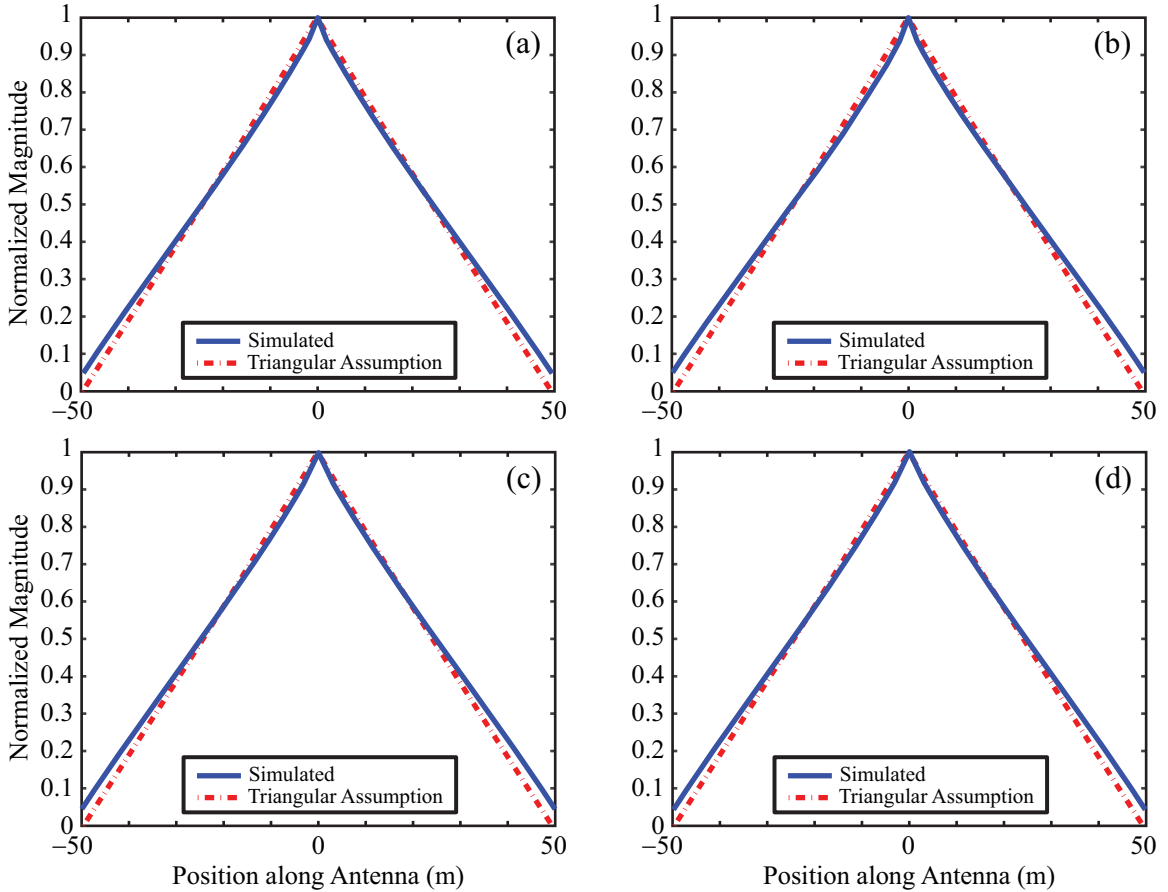


**Figure 4.5:** Current distribution for a 100 m antenna at  $L=2$  for driving frequencies above and below  $f_{LHR}$ . (a)  $f=400$  Hz ( $f < f_{LHR}$ ). (b)  $f=2.0$  kHz ( $f < f_{LHR}$ ). (c)  $f=2.6$  kHz ( $f > f_{LHR}$ ). (d)  $f=10.0$  kHz ( $f > f_{LHR}$ ).

simulations affirm the accuracy of the triangular current assumption made by *Wang and Bell* [1969, 1970] and *Wang* [1970] in the absence of the sheath providing assurance in the validity of the impedance calculations that are now discussed.

Figures 4.6a and 4.6b compare the simulated input impedance of the 100 m dipole antenna at  $L=2$  with results obtained from *Wang and Bell* [1969, 1970]; *Wang* [1970]. Figure 4.6b represents an expanded portion of Figure 4.6a showing the zero impedance point in finer detail. The plots for both the resistance and reactance calculated with our numerical simulation are in good agreement with those evaluated analytically by *Wang and Bell* [1969, 1970] and *Wang* [1970]. Below  $f_{LHR}$ , *Wang and*

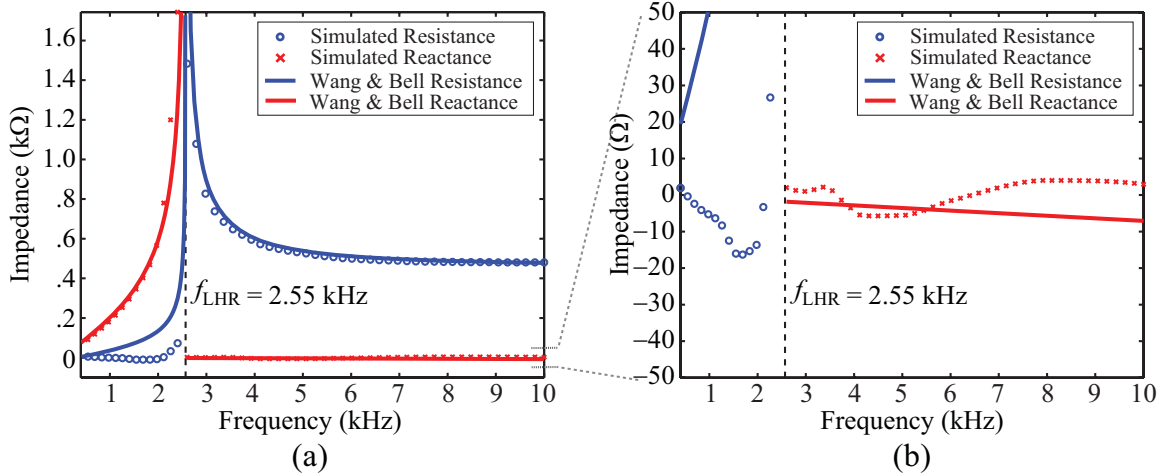


**Figure 4.6:** Input impedance for a 100 m antenna at  $L=2$ . (a) Full range response (b) Expanded region around zero impedance

*Bell* [1969, 1970] and *Wang* [1970] predict the reactance to vary from approximately 100  $\Omega$  at zero frequency to infinite at the LHR frequency. Unlike the case of the quasi-electrostatic assumption of *Balmain* [1964], the work of *Wang and Bell* [1969, 1970] and *Wang* [1970] predict the resistance to have a non-zero value below the LHR frequency ranging from zero at DC to infinite at the LHR frequency. These trends are reflected in the simulated results as shown in Figures 4.6a and 4.6b. Above  $f_{LHR}$ , the analytical reactance varies from zero to about  $-8 \Omega$  at 10 kHz. The simulated impedance results in this regime are within about 15  $\Omega$ .

The disparity between the analytical and simulated results in Figure 4.6b is attributed to a combination of theory and numerical accuracy of the FDFD technique. *Wang and Bell* [1969, 1970] and *Wang* [1970] assume a triangular current distribution with zero current at the tips of the antenna. In reality, an antenna possessing finite width supports current at the tips of the antenna as shown in the simulation plots of Figures 4.5a-4.5d. Additionally, the use of cells which are at least  $10^4$  times smaller than the corresponding free-space wavelength results in convergence issues for the associated FDFD matrix. The large ratio of wavelength to cell size produces a matrix with vastly different eigenvalues and thus a large condition number; a limitation of the frequency domain method in this regime. This limitation is readily seen in Figure

4.6b for which there exist impedance values that possess a negative resistance below the LHR frequency.

Since our impedance results agree quite well with the work of *Wang and Bell* [1969, 1970] and *Wang* [1970] except for the likely unphysical negative resistance below  $f_{\text{LHR}}$ , we expect that the results of *Wang and Bell* [1969, 1970] and *Wang* [1970] are more accurate for this resistance calculation than our AIP code. However, since *Wang and Bell* [1969, 1970] and *Wang* [1970] are restricted to dipole antennas, an accurate and general simulation tool is desired. Therefore, future work will need to explore possible ways to circumvent this difficulty such as a different type of normalization procedure or reformulating the FDFD equations in order to achieve better convergence in this frequency range.

## 4.4 Current Distributions and Input Impedance Calculations for a 100 m Antenna at $L=3$

The second case study examines the properties of a 100 m antenna located at  $L=3$  in the equatorial plane. Typical values of the plasma and gyrofrequencies at  $L=3$  are  $f_{\text{pe}} = 284$  kHz and  $f_{\text{ce}} = 32.6$  kHz respectively. Since the computational mesh geometry of Figure 4.2 and the PML performance characteristics of Figure 4.3 are very similar to the simulation setup at  $L=2$ , these characteristics are not shown. Only two different examples of the current distribution are given since they are not markedly different than those for the cases of an antenna at  $L=2$ . Figures 4.7a and 4.7b represent the current distributions for frequencies above and below  $f_{\text{LHR}}=761$  Hz respectively.

It can be seen from Figures 4.7a and 4.7b that there is no significant deviation from a triangular current distribution for an antenna subject to a decrease in plasma and gyrofrequencies. Figures 4.8a and 4.8b compare the simulated input impedance of the 100 m dipole antenna at  $L=3$  with results obtained from *Wang and Bell* [1969, 1970] and *Wang* [1970].

As with the results from the previous case study, the impedance characteristics

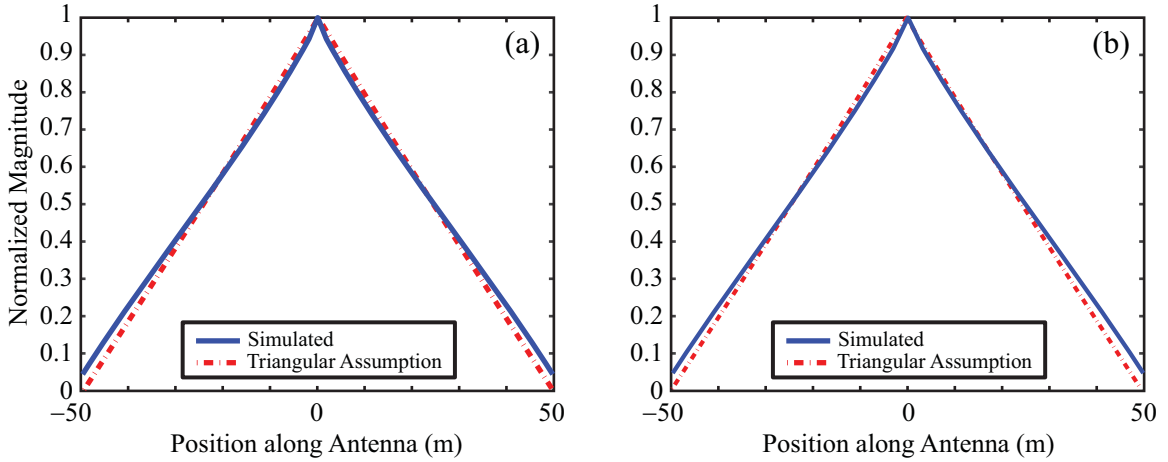


**Figure 4.7:** Current distribution for a 100 m antenna at  $L=3$  for driving frequencies above and below  $f_{LHR}$ . (a)  $f=460$  Hz ( $f < f_{LHR}$ ). (b)  $f=4.0$  kHz ( $f > f_{LHR}$ ).

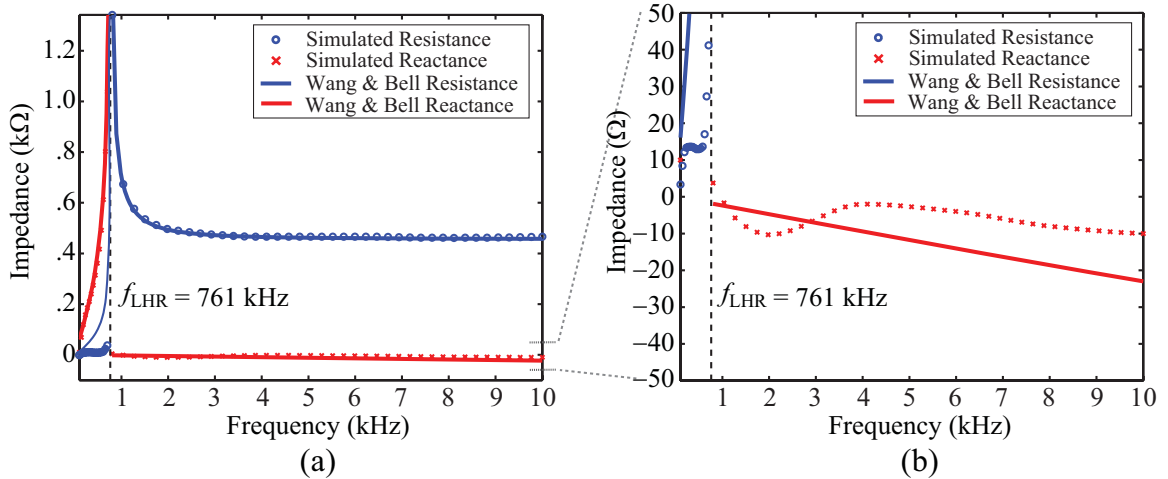


**Figure 4.8:** Input impedance for a 100 m antenna at  $L=3$ . (a) Full range response (b) Expanded region around zero impedance

in Figure 4.8 exhibit good agreement with the work of *Wang and Bell* [1969, 1970] and *Wang* [1970] except for the difference in resistance values for frequencies below  $f_{LHR}$ . Relative to the case at  $L=2$  however, the resistance values below  $f_{LHR}$  as shown in Figure 4.8b exhibit better agreement with the theoretical results. This can be attributed to the fact that since the number density and magnetic field strength are less at  $L=3$ , so is the degree of anisotropy, thereby resulting in an FDFD matrix

that possesses better convergence characteristics.

## 4.5 Non-triangular Current Distributions

For the 100 m antennas we have considered thus far operating at both  $L=2$  and  $L=3$  in the equatorial plane, the current distributions have remained virtually triangular. We now show that there exist cases for which these electrically short antennas operating at VLF frequencies exhibit current distributions that decay exponentially along the length of the antenna as a result of their orientation lying within the evanescent region of the refractive index surface for frequencies above  $f_{\text{LHR}}$ . For this purpose, we consider antennas operating at  $L=2$  only and consider variations in length and plasma frequency while keeping the gyrofrequencies constant. For these comparisons,  $f_{\text{LHR}}$  is unchanged and has a value of 2.55 kHz.

### 4.5.1 Long Antennas

First we consider the effects of an increase in antenna length, keeping all plasma parameters constant, corresponding to conditions found at  $L=2$  as in Section 4.3. Figures 4.9a and 4.9b show the current distribution for linear antennas that are 2000 m and 4000 m corresponding to lengths which are factors of 30 and 15 smaller than the equivalent free-space wavelength respectively.

It is seen from Figure 4.9a that for a 2000 m antenna, the current distribution only slightly deviates from the triangular assumption whereas for the 4000 m antenna shown in Figure 4.9b the current experiences substantial decay which would result in a significant decrease in the dipole moment, thereby reducing the radiation resistance. Thus, dipole antennas that exhibit this type of exponential decay along the length of the elements would not be as efficient at delivering power to the medium and therefore, are not as useful as wave-injection instruments.

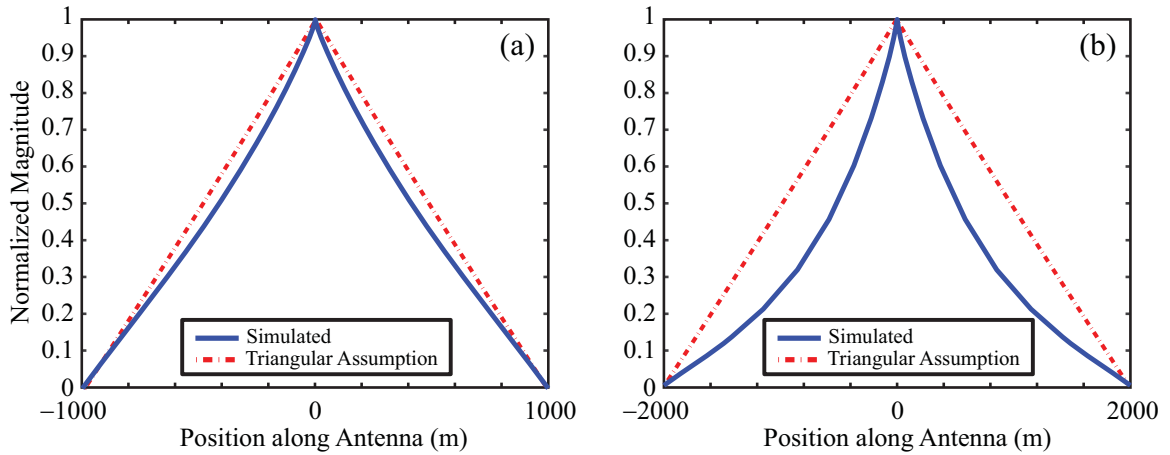


**Figure 4.9:** Current distributions for long antennas at  $L=2$  operating at 5 kHz. (a) Length = 2000 m (b) Length = 4000 m

### 4.5.2 High Plasma Frequency

An increase in the local plasma frequency, keeping all other factors unchanged, results in a similar exponential decrease in the antenna current distribution. In this case we examine a 100 m long antenna operating at an augmented  $L=2$  plasma environment by adjusting only the local plasma frequency  $f_{pe}$  to values of 10 MHz and 20 MHz. These results are shown in Figure 4.10.

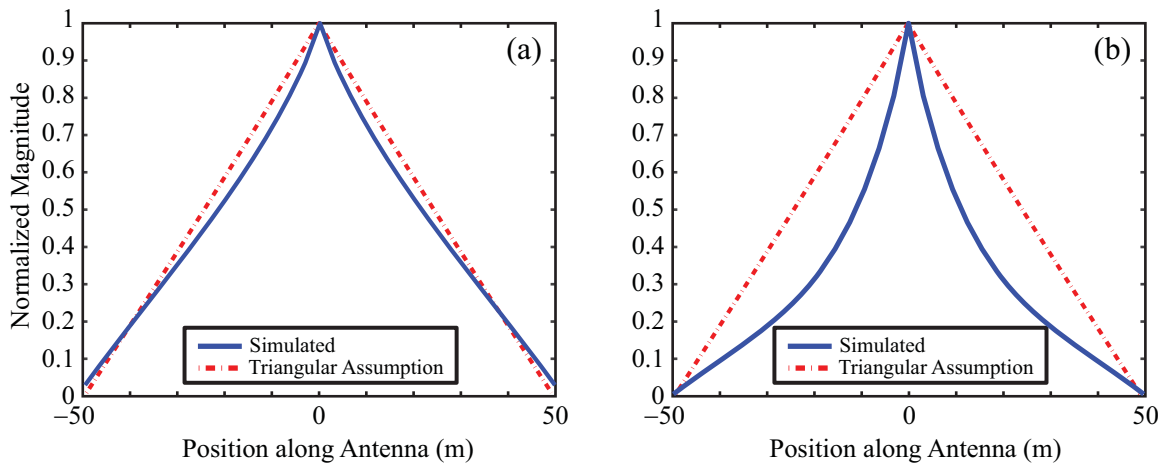


**Figure 4.10:** Current distributions for 100 m antenna operating in high density plasma at driving frequency of 5 kHz. (a)  $f_{pe} = 10$  MHz (b)  $f_{pe} = 20$  MHz

Figure 4.10a and 4.10b correspond to plasma frequencies that are roughly 20 and 40 times the normal value at  $L=2$ . It is not until the plasma frequency reaches 20 MHz as shown in Figure 4.10b that we see a detrimental effect on the current moment as in Figure 4.9b. Since plasma frequencies that are this high are not typically seen in space environments which are considered in this dissertation, the example of Figure 4.10 is of little concern for a 100 m antenna. However, for future space missions that propose long antenna designs, this adverse effect on the current distribution due to long antenna lengths is an issue that would need to be addressed since there apparently is nothing to be gained by using longer dipole antennas, at least in terms of radiation efficiency.

With respect to the case of high plasma frequency, our simulations have only explored 100 m antennas. However, it is entirely possible that slightly longer antennas orbiting at low altitudes such as in the polar regions of the Earth, where the electron densities can be much larger, would exhibit the same exponential decay as in the previous case study concerning the 4000 m antenna operating in the equatorial region of  $L=2$ . Future simulation work using our AIP code could determine this minimum length requirement for a given plasma environment.

# Chapter 5

## Warm Plasma Electrostatic Model

In this chapter, we extend the capability of the AIP simulation tool to include warm plasma effects in order to study the formation of the plasma sheath surrounding a dipole antenna. The warm plasma formulation incorporates all nonlinear effects for each fluid moment utilized, coupled with Poisson's equation for the quasi-electrostatic fields. The details of this approach along with the closure approximations and simulation techniques used are now discussed.

### 5.1 Closure Approximations

In the warm plasma fluid approximation, no assumptions of linearity are made and thus all convective terms in the system of moments defined by Equations 2.4a-2.4d are preserved. Three warm plasma closure mechanisms are considered in this dissertation. The first closure relation is the isothermal approximation which assumes that the pressure tensor  $\mathbf{P}$  is diagonal with each element  $p$  given by the ideal gas law relation  $p=nk_{\text{B}}T$ , where  $T$  is the plasma *temperature* in all directions. In this isothermal approximation, the system of equations representing the plasma is given by the first two fluid moments shown in Equations 2.4a-2.4b which are repeated here for convenience:

$$\partial_t(nm) + \nabla \cdot (nm\mathbf{u}) = 0 \quad (2.4a)$$

$$\partial_t(nm\mathbf{u}) + \nabla \cdot (nm\mathbf{u}\mathbf{u} + \mathbf{P}) - nq(\mathbf{E} + \mathbf{u} \times \mathbf{B}) = 0 \quad (2.4b)$$

It should be noted that a very simplified adiabatic energy equation for each species  $\alpha$  such as  $p_\alpha n_\alpha^{-\gamma_\alpha} = \text{constant}$  can be used instead of the isothermal approximation without explicitly solving a full moment equation for the pressure tensor  $\mathbf{P}$ . This modifies the isothermal approximation  $p = nk_B T$  by the factor  $\gamma$  where  $\gamma = 1 + 2/N$  and  $N$  is the number of *degrees of freedom* [Bittencourt, 2003, page 454]. Thus the pressure gradient, which is derived from the diagonal elements of the pressure tensor for each species in our two-moment model, now becomes:

$$\nabla p_\alpha = \gamma k_B T_\alpha \nabla n_\alpha \quad (5.2)$$

where  $n$  is the *number density* and  $p$  is one of the diagonal elements of the tensor. *Ma and Schunk* [1989] compared both this simplified adiabatic relation and the isothermal formulation and found that there was virtually no difference between the two approximations at high applied potentials relative to the background plasma potential. The reason the two approximations are equivalent is that the pressure gradient is most significant where the density changes rapidly and the electric field is weak [Ma and Schunk, 1989]; however, the only way to produce a large density gradient in our case is with a strong electric field.

The second closure relation assumes that the system is adiabatic (i.e.,  $\nabla \cdot \mathbf{Q} = 0$ ) and thus all terms involving the heat flux tensor are zero. In this adiabatic formulation, the plasma is represented by the first three moments of Equation 2.1 repeated below as Equations 2.4a-2.4c:

$$\partial_t(nm) + \nabla \cdot (nm\mathbf{u}) = 0 \quad (2.4a)$$

$$\partial_t(nm\mathbf{u}) + \nabla \cdot (nm\mathbf{u}\mathbf{u} + \mathbf{P}) - nq(\mathbf{E} + \mathbf{u} \times \mathbf{B}) = 0 \quad (2.4b)$$

$$\partial_t(\mathbf{P}) + \nabla \cdot (\mathbf{u}\mathbf{P} + \mathbf{Q}) + \{\mathbf{P} \cdot \nabla(\mathbf{u}) + \boldsymbol{\Omega}_c \times \mathbf{P}\}^{\text{sym}} = 0 \quad (2.4c)$$

The third closure relation makes no assumptions on adiabaticity and includes the heat-flux tensor as well as an approximation on the 4<sup>th</sup> order moment  $\mathbf{R}$ . The system of equations using this non-adiabatic closure approximation is given by:

$$\partial_t(nm) + \nabla \cdot (nm\mathbf{u}) = 0 \quad (2.4a)$$

$$\partial_t(nm\mathbf{u}) + \nabla \cdot (nm\mathbf{u}\mathbf{u} + \mathbf{P}) - nq(\mathbf{E} + \mathbf{u} \times \mathbf{B}) = 0 \quad (2.4b)$$

$$\partial_t(\mathbf{P}) + \nabla \cdot (\mathbf{u}\mathbf{P} + \mathbf{Q}) + \{\mathbf{P} \cdot \nabla(\mathbf{u}) + \boldsymbol{\Omega}_c \times \mathbf{P}\}^{sym} = 0 \quad (2.4c)$$

$$\partial_t(\mathbf{Q}) + \nabla \cdot (\mathbf{v}\mathbf{Q} + \mathbf{R}) + \left\{ \mathbf{Q} \cdot \nabla(\mathbf{u}) + \boldsymbol{\Omega}_c \times \mathbf{Q} - \mathbf{P} \nabla \cdot (\mathbf{P}) \frac{1}{nm} \right\}^{sym} = 0 \quad (2.4d)$$

## 5.2 Quasi-Electrostatic Approximation

Though early antenna work involving sheath formation makes unjustified simplifying assumptions [Mlodnosky and Garriott, 1963], some insight into the relative size of the sheath can be gained so as to gauge whether or not a quasi-electrostatic solution is justified at high voltages. The work of Laframboise [1997] provides modifications to the Boltzmann factor based on various criteria for spacecraft charging. Using Laframboise [1997] as a reference coupled with the sheath radius approximations in Mlodnosky and Garriott [1963], we can deduce that even at 1000 V applied potential on the antenna, the sheath radius would only be a couple of meters at VLF frequencies, still much smaller than the smallest electromagnetic wavelength. In addition, some insight can be obtained from the examination of Equations 3.4a and 3.4b in terms of the relative magnitudes of various quantities. A first order approximation of the wave electric field using Equations 3.4a and 3.4b at 1000 V does not produce a wave magnetic field that has a magnitude on the same scale as the background magnetic field. Likewise, a comparison of the displacement and conduction current terms at VLF frequencies yields the relation  $\sigma \gg \omega\epsilon_0$  when  $\omega_p \gg \omega$ , providing further justification for the electrostatic approximation since it is the conduction current term that is dominant. Therefore, a quasi-static approach is justified and Poisson's equation can be used to close the system of fluid equations given by:

$$\nabla \cdot \mathbf{E} = \frac{\sum_{\alpha} \rho_{\alpha}}{\epsilon_0} \quad (5.5)$$

where  $\epsilon_0$  is the *permittivity* of free space, and the *charge density*  $\rho$  is summed across all species  $\alpha$ , with  $\alpha=2$  representing only electrons and protons in our model. The use of Poisson's equation removes the electromagnetic time-stepping constraint and avoids the PML instabilities discussed in Chapter 3. Since the use of Poisson's equation in our model supports only electrostatic waves, a PML is not required. In addition, the use of Poisson's equation assumes a constant potential distribution on each antenna element as shown in Figure 5.1

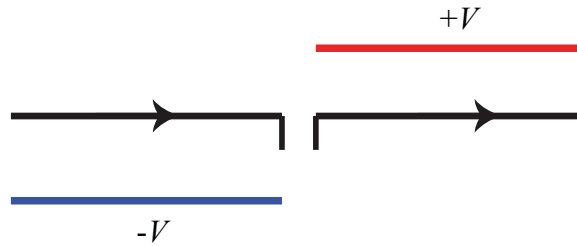


**Figure 5.1:** Electrostatic potential variation on electrically short dipole antenna.

The constant potential variation in Figure 5.1 forces a triangular current distribution on the antenna as previously shown in Figure 4.4 for the case of an electrically short antenna. This current distribution is in agreement with our findings using the cold plasma electromagnetic model and is therefore quite accurate for our purposes.

### 5.3 Simulation Development

Instead of using finite-differences for the spatial derivatives as in our cold plasma model of Chapter 3, the warm plasma model uses a finite-volume method to solve for the fluid dynamics and an iterative matrix solver for the solution of Poisson's equation which provides the electrostatic fields. Once again, the simulation tool uses the same PETSc framework [Balay *et al.*, 2001, 2004] as was used for development of the cold plasma model.

### 5.3.1 Fluid Formulation

Equations 2.4a-2.4d can be written as a system of conservation laws of the form:

$$\frac{\partial \bar{\mathbf{U}}}{\partial t} + \nabla \cdot \mathcal{F}(\bar{\mathbf{U}}) = \bar{\mathbf{S}} \quad (5.6)$$

where  $\bar{\mathbf{U}}$  is the column vector of conserved quantities,  $\mathcal{F}$  is the nonlinear flux function taking into account all convective derivatives in Equations 2.4a-2.4d and  $\bar{\mathbf{S}}$  corresponds to the source terms for each moment. In a Cartesian coordinate system,  $\bar{\mathbf{U}} = \bar{\mathbf{U}}(x, y, z, t)$  and  $\bar{\mathbf{S}} = \bar{\mathbf{S}}(x, y, z, t)$  are functions of both space and time. Strictly speaking, pressure and heat flux are not conserved quantities; however, rewriting the update equations for these variables in the form of Equation 5.6 allows for a straightforward application of a conservative FV technique for which these equations are aptly suited. In this context, ‘conservative’ means that the amount of a given quantity (such as mass density or momentum) leaving one cell and entering an adjacent cell through a single flux face is the same. This condition essentially means that field quantities are neither created nor removed as a result of the spatial difference operator.

Finite-Volume methods solve the integral form of a system of partial differential equations by recasting the homogeneous form of the general moment equation given by Equation 5.6 into conservative form using the divergence theorem:

$$\frac{\partial}{\partial t} \iiint_V \bar{\mathbf{U}} dV + \iint_S (\nabla \cdot \mathcal{F}) dS = 0 \quad (5.7)$$

The FV method we have chosen utilizes the central differencing formulation of *Kurganov and Tadmor* [2000]. This method is second order accurate in space and is coupled with the strong stability preserving (SSP) Explicit Runge-Kutta (ERK) time-integration schemes of *Spiteri and Ruuth* [2002] which are up to fourth order accurate in time. A variable time-step algorithm is employed in our simulation tool since the fluid velocities are constantly changing in time due to the dynamic structure of the sheath. This adaptive time-step is most critical during the early stages involving transient sheath formation.

The central differencing technique allows for all fluid variables to be colocated in space, being at the center of a computational cell, eliminating the need for the spatial averaging of various quantities as in the FDTD method. The method of *Kurganov and Tadmor* [2000] is a shock capturing scheme and utilizes nonlinear functions called ‘limiters’ to suppress spurious oscillations due to large spatial gradients and mesh decoupling due to the central differencing strategy. High resolution central schemes such as *Kurganov and Tadmor* [2000] have successfully been applied to the study of solar wind dynamics [*Keller et al.*, 2002] and semi-conductor processing [*Anile et al.*, 2000b,a]. The method of *Kurganov and Tadmor* [2000] was chosen so as to capture the steep density gradients that might form during initial sheath formation at large applied potentials due to the presence of nonlinear terms in the moment equations. Nonlinear terms have the effect of steepening propagating wavefronts, producing gradients on the order of a mesh cell size and creating spurious oscillations due to spatial aliasing. A detailed description of the method outlined in *Kurganov and Tadmor* [2000] and the concept of nonlinear limiters which suppress oscillatory behavior is provided in Appendix D. A brief outline of the key points of the method presented in *Kurganov and Tadmor* [2000] is now discussed.

The non-oscillatory nature of *Kurganov and Tadmor* [2000] is achieved through the addition of an artificial diffusion term which utilizes information on the local characteristic speeds of wave propagation in the medium which are related to the Courant-Friedrichs-Lewy (CFL) condition [*Courant et al.*, 1967]. The local characteristic speeds at time step  $n$  and at spatial step  $j + \frac{1}{2}$  are calculated using Equation 3.1 from *Kurganov and Tadmor* [2000]:

$$a_{j+\frac{1}{2}}^n = \max_{\bar{\mathbf{U}} \in \mathcal{C}(U_{j+\frac{1}{2}}^-, U_{j+\frac{1}{2}}^+)} \rho \left[ \frac{\partial \mathcal{F}}{\partial \bar{\mathbf{U}}} (\bar{\mathbf{U}}) \right] \quad (5.8)$$

Equation 5.8 states that the characteristics speeds are equal to the maximum value of the spectral radius of the Jacobian  $\mathcal{J}$  of the flux function  $\mathcal{F}$  evaluated at each cell interface, where  $\mathcal{J} = \partial \mathcal{F} / \partial \bar{\mathbf{U}}$ . The spectral radius corresponds to the magnitude of the largest eigenvalue found from the characteristic equation derived from taking the

determinant of  $\mathcal{J}$ . To illustrate the calculation of the spectral radius  $\mathbf{A}$  for a two-moment plasma fluid system, we examine only the  $\hat{x}$ -directed fluxes of the system of equations described by Equation 5.6 and neglect the source terms since the spectral radius only depends on the vector of fluxes  $\mathcal{F}$ . The resulting system of equations is given by Equation 5.9.

$$\begin{bmatrix} \rho \\ m_x \\ m_y \\ m_z \end{bmatrix}_t + \begin{bmatrix} m_x \\ m_x^2/\rho + p_{xx} \\ m_x m_y/\rho + p_{xy} \\ m_x m_z/\rho + p_{xz} \end{bmatrix}_x = 0 \quad (5.9)$$

where  $\rho$  is the *mass density*,  $m_x=\rho v_x$ ,  $m_y=\rho v_y$  and  $m_z=\rho v_z$  are the *momenta* in each coordinate direction, and  $p_{xx}$ ,  $p_{xy}$  and  $p_{xz}$  are the corresponding components of the *pressure tensor*. For simplicity in the example calculation, we use the ideal gas law for pressure  $\mathbf{P}=nk_B\mathbf{T}$ , providing  $p_{xx}=nk_B T$  with all off diagonal elements being zero. The subscripts  $t$  and  $x$  correspond to derivatives with respect to time and space in the  $\hat{x}$ -direction. The Jacobian  $\mathcal{J}$  of Equation 5.9 is given by Equation 5.10:

$$\mathcal{J} = \frac{\partial \mathcal{F}}{\partial \mathbf{U}} = \begin{bmatrix} 0 & 1 & 0 & 0 \\ \frac{k_B T}{m} - \frac{m_x^2}{\rho^2} & \frac{2m_x}{\rho} & 0 & 0 \\ -\frac{m_x m_y}{\rho^2} & \frac{m_y}{\rho} & \frac{m_x}{\rho} & 0 \\ -\frac{m_x m_z}{\rho^2} & \frac{m_z}{\rho} & 0 & \frac{m_x}{\rho} \end{bmatrix} \quad (5.10)$$

The characteristic polynomial is 4<sup>th</sup> order due to the rank of  $\mathcal{J}$  and thus provides 4 eigenvalues which are equal to  $\lambda = \left[ v_x + \sqrt{k_B T/m}, v_x - \sqrt{k_B T/m}, v_x, v_x \right]$  respectively. The spectral radius  $\mathbf{A}$  which is equal to the magnitude of the largest eigenvalue  $\lambda$  of the corresponding characteristic equation is one of  $\mathbf{A} = |\lambda| = \left| v_x \pm \sqrt{k_B T/m} \right|$  depending on the sign of the velocity  $v_x$ . This relation essentially states that the characteristic speeds are simply the sum of the bulk velocity and thermal velocity. The characteristic speeds are virtually the same in each of the other dimensions, with a simple substitution of coordinate direction, and the speeds for the higher order moments

are found in the same way. When the equations are normalized however, the expressions for the characteristic speeds become more complicated since it is assumed in the derivation that all normalization factors are different. This concept is discussed in the following section.

### 5.3.2 Normalization of Fluid Equations

Each equation in the set of fluid moments is normalized based on the ambient conditions and characteristic scales in the plasma. The normalization of the length scales in each coordinate direction  $(\tilde{x}, \tilde{y}, \tilde{z})$  are based upon the smallest cell size in the computational domain. Since each moment is derived by taking successive moments of the Vlasov equation with respect to powers of the total velocity  $\mathbf{v}$  and/or random thermal motions  $\mathbf{c}$ , the variables such as density, momentum, pressure and heat-flux are normalized with respect to the corresponding powers of the ambient thermal velocity for that species. The variable time is normalized with respect to the ratio of the smallest cell size in the computational domain to the speed of light. For instance, in a single dimension, this normalization would be  $\tilde{t} = \Delta x_{\min}/c$  where  $\Delta x_{\min}$  is the smallest *cell size* in the  $\hat{x}$ -direction,  $c$  is the *speed of light*, and  $\tilde{t}$  is the *normalization constant* for time.

### 5.3.3 Multi-scale Simulations

Multi-scale plasma simulation regions which have been used by previous authors [Parker *et al.*, 1993a,b; Wang and Wendt, 1999] are very useful in minimizing the computational requirements by utilizing spatial scales that are appropriate to the region of interest. In the context of sheath dynamics, one typically uses cell sizes on the order of a Debye length  $\lambda_D$  within the sheath region, in order to capture the shielding effects without spatial aliasing. Outside of the sheath region however, the scale lengths are generally larger in order to capture physics such as Langmuir oscillations and electromagnetic waves. For instance, Parker *et al.* [1993a] successfully modeled the sheath region and ion acoustic waves using a PIC code, while Wang and Wendt [1999] likewise modeled the sheath using a fluid approach. In both cases, the

cell size within the sheath region was on the order of a Debye length  $\lambda_D$  while outside of the sheath the cell size  $\Delta x$  gradually increased to lengths  $\Delta x \gg \lambda_D$ . Additionally, *Parker et al.* [1993b] applied a multi-scale approach to approximate the sheath with a ‘logical sheath’ boundary condition without actually resolving the sheath region, obtaining results comparable with analytical descriptions of the sheath.

An adjusted mass ratio is often used in simulations [*Calder and Laframboise*, 1990; *Calder et al.*, 1993] to reduce the computational requirements as long as the underlying principal physics is not significantly modified i.e.,  $m_i \gg m_e$ . In our simulations, we assume a proton-electron temperature ratio of  $(T_p/T_e)=1.0$  and in some of the simulation results presented in Chapter 6, a mass ratio of  $(m_p/m_e)=200$ . These assumptions are clearly marked in the corresponding results section.

### 5.3.4 Boundary Conditions

Boundary conditions are implemented for both Poisson’s equation and the plasma fluid equations. In either case, these relations must be specified on the plasma-facing surface of the material immersed within the plasma (e.g., the antenna surface) as well as at the exterior of the simulation domain. The boundary conditions used in our warm plasma model for the fields and the fluid are now discussed.

#### Poisson’s Equation

On the surface of the conductor there are two distinct types of boundary conditions implemented for the solution of Poisson’s equation, based on whether or not the conducting element is active or passive. If the element is active, as in the case of a transmitting antenna, the potential on the conducting surface is forced to be the driving potential. If the element is passive, the situation is slightly more complex. A conducting body immersed in a plasma collects space charge, creating a floating DC potential on the conducting surface as a result of the different mobility of each plasma species. At a temperature of  $T = 2000^\circ$  K, this negative DC floating potential has a magnitude on the order of a few tenths of an electron-volt (eV). The passive condition corresponds to the initial conditions of the fluid simulation since it is the initial state of

any non-transmitting element in a plasma. Therefore, in our simulations, this initial floating state of the conductor is first run as a separate self-consistent simulation, providing the initial conditions used in the active antenna simulations. The solution of Poisson's equation for the floating conductor utilizes the capacity matrix method developed by *Hockney and Eastwood* [1981].

At the edge of the computational space, our model utilizes a Robin boundary condition [*Eriksson et al.*, 1996, page 184] for Poisson's equation which allows us to specify, for the potential  $\Phi$ , a Dirichlet condition  $\Phi = \Upsilon$ , Neumann condition  $d\Phi/dx = \Upsilon$ , or any linear combination thereof for a value of the constant  $\Upsilon$  and spatial variable  $x$ . The partial differential equation describing a Robin boundary condition for the potential  $\Phi$  in the  $\hat{x}$ -direction is given by Equation 5.11.

$$\eta\Phi + \xi\frac{d\Phi}{dx} = \Upsilon \quad (5.11)$$

where  $\eta$  and  $\xi$  are user-adjustable constants. We assume the plasma to be quasi-neutral far from the sheath region and therefore implement a Dirichlet boundary condition with the potential at the outer boundary of the domain equal to zero. In this case, we set  $\eta=1$ ,  $\xi=0$ , and  $\Upsilon=0$ , and adjust the corresponding boundary values in the potential matrix.

### Fluid Equations

The boundary conditions at the conductor surface for each of the fluid moments are found by integrating an assumed Maxwellian distribution in either the left or right half plane for each quantity that is crossing an imaginary flux surface in a single direction. For the first two moments, the distribution function is assumed to be a drifting Maxwellian given by Equation 2.2. For the pressure and heat flux moments which only take into account the thermal motions of the particles, the distribution function is modeled as a non-drifting Maxwellian. For the 0<sup>th</sup> moment which corresponds to mass density, we assume a zero gradient or Neumann condition across the surface of the conductor. For the 1<sup>st</sup> moment corresponding to momentum conservation, the uni-directional velocity  $v_s$  of a fluid element at the surface of a conductor located in

the right half plane is given by Equation 5.12:

$$v_s = \frac{1}{2} \left\{ e^{-v_0^2/(2v_{th}^2)} \sqrt{\frac{2}{\pi}} v_{th} + \left[ 1 + \operatorname{erf} \left( \frac{v_0}{\sqrt{2}v_{th}} \right) \right] v_o \right\} \quad (5.12)$$

where  $v_0$  is the Maxwellian drift velocity,  $v_{th}$  is the thermal velocity, and  $\operatorname{erf} [ ]$  represents the error function. Figure 5.2 is a plot of Equation 5.12 showing the relationship between the drift velocity and total velocity of the particles.

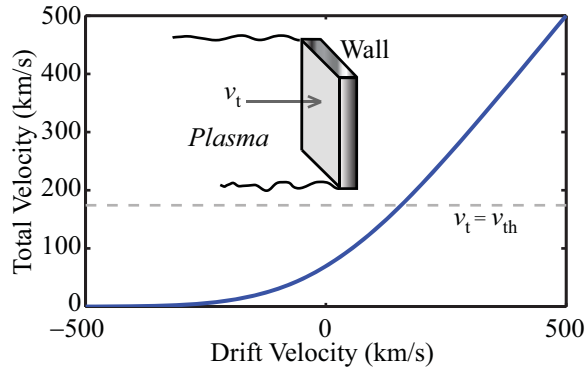


**Figure 5.2:** Fluid velocity boundary condition at material facing surface.

From Figure 5.2, it can be seen that the total velocity of the fluid element is always directed into the material. Thus, on a microscopic scale, when a particle impacts on the surface of the conductor, it is absorbed and is thus not able to return to the bulk plasma. High energy particles impacting the surface could certainly spawn the emission of secondary particles. However, for reasons outlined in Chapter 2, this effect is not included in our present model. The pressure and heat flux elements at the conductor surface are found in a similar manner by integrating with respect to a uni-directional velocity distribution in the direction facing the conductor. This integration produces a pressure tensor at the material boundary for which all off-diagonal elements are zero, resulting from the integration of an odd function in the directions perpendicular to the material-facing surface.

# Chapter 6

## Plasma Sheath Results

The warm plasma fluid formulation is designed for the study of sheath formation surrounding an electric dipole antenna. In this chapter we apply the AIP code in the electrostatic regime to study the sheath properties. We show that it is the sheath which dominantly determines the terminal impedance and thus the tuning requirements for the antenna, and that it is thus imperative to accurately simulate its contribution. We begin by validating our fluid model in the context of one-dimensional planar sheath simulations through comparison with the analytical work of *Bohm* [1949]. As discussed in Chapter 1, these analytical formulas provide a reasonable approximation to the floating sheath and are documented in many plasma physics textbooks [*Bitencourt*, 2003, pages 279-288]. Next, we examine the effect of various closure mechanisms on the formation of the sheath around a two-dimensional infinite line source considering both isotropic and magnetized plasmas. Finally, simulation results for the sheath surrounding a 20 m long electric dipole antenna in three-dimensions are presented for four case studies. Geometric and terminal impedance characteristics of the dipole antenna are highlighted in interpreting the results of these simulation runs.

## 6.1 One-dimensional Planar Sheath

### 6.1.1 Bohm Sheath Derivation

In the presence of a conservative force field, the equilibrium steady-state Maxwell-Boltzmann distribution of Equation 2.2 is modified by an additional exponential forcing function which is called the Boltzmann factor and is equal to [Bittencourt, 2003, page 181]:

$$\exp \left[ -\frac{U(\mathbf{r})}{k_B T} \right] \quad (6.1)$$

where  $U(\mathbf{r}) = q\Phi(\mathbf{r})$  for a *potential* field  $\Phi(\mathbf{r})$  and *position* vector  $\mathbf{r}$ . Once again,  $q$  is the *charge* of the particle,  $k_B$  is *Boltzmann's constant* and  $T$  is *temperature*. Using the assumption that the electrostatic potential is weak relative to the background temperature of the plasma, i.e.,  $q\Phi(\mathbf{r}) \ll k_B T$ , one can derive the formula for the Debye shielding distance  $\lambda_D$  which is equal to:

$$\lambda_D = \sqrt{\frac{\epsilon_0 k_B T}{n_e q_e^2}} \quad (6.2)$$

where  $n_e$  is the electron *number density* and all other variables were defined earlier. The relation  $q\Phi(\mathbf{r}) \ll k_B T$  and Equation 6.1 form the basis of the derivation in *Bohm* [1949], allowing for the closed form solution of the planar-sheath which develops adjacent to a conducting wall. The details of the formulation, which are based upon the first two linearized moments of Equation 2.1 coupled with Poisson's equation, are outlined in [Bittencourt, 2003, pages 279-288]. A summary of these analytical formulas with which we compare our nonlinear warm plasma formulation in a regime for which the analytical results are valid is now given. Subsequently, we point out the inherent weaknesses in these analytical formulations as they relate to AC antenna sheath analysis at high voltages.

The sheath develops as a result of the vastly different mobilities of the electrons and protons in our two species plasma. As electrons collect on the conductor, being much lighter and more mobile, they produce a net negative potential on the surface

of the floating conductor which prevents additional electrons from being collected. Eventually, a steady state is reached when the net current draw onto the conductor is zero. The analytical floating potential on the wall in this steady state situation is equal to:

$$\Phi_{\text{wall}} = -\frac{k_B T}{4|q_e|} \ln\left(\frac{m_p}{m_e}\right) \quad (6.3)$$

where  $m_p$  and  $m_e$  are the *mass* of a proton and electron respectively. Allowing for 1-D variations in  $\hat{x}$  only, the steady-state electron and proton density profiles in the  $\hat{x}$ -direction are found to be:

$$n_e(x) = n_0 \exp\left[\frac{|q_e|\Phi(x)}{k_B T}\right] \quad (6.4a)$$

$$n_p(x) = n_0 \left[1 - \frac{2|q_e|\Phi(x)}{m_p u_{\text{op}}^2}\right]^{-1/2} \quad (6.4b)$$

where  $n_0$  is the bulk plasma density and  $u_{\text{op}}$  is the drift velocity of the protons entering the sheath originating from  $x = \infty$ . The final approximation needed in the derivation of Equations 6.4a-6.4b is given by Equation 6.5:

$$m_e u_e^2 \ll k_B T \ll m_p u_p^2 \quad (6.5)$$

where  $u_e$  and  $u_p$  are the *velocities* of the electrons and proton fluids throughout the sheath region. Equation 6.5 is simply a statement that the kinetic energy of the ions is greater than their thermal energy, while for the electrons, the opposite is assumed.

### 6.1.2 1-D Simulation of Planar Sheath

To test our warm plasma simulation tool, we consider a collisionless, fully ionized plasma with parameters corresponding to  $L=2$  in the equatorial plane as in the cold plasma results of Chapter 4. The Debye length for this plasma is  $\lambda_D \simeq 7$  cm and the proton-electron mass ratio is  $(m_p/m_e) = 1836$ . The cell size in the simulation domain is chosen as to capture any Debye-scale effects under these low-voltage conditions and

is made to be  $\Delta x = 2.5$  cm, with the entire space being 2.5 m in length or roughly  $36 \lambda_D$ . For these one-dimensional planar sheath calculations we neglect the magnetic field. A floating (no applied potential) conducting wall is placed in the left half plane of the 1-D simulation space with the initial number densities of electrons and protons made constant across the simulation domain. In addition, the initial velocities of both the protons and electrons are zero with the only non-zero element being the directed drift-velocity boundary condition specified in Equation 5.12 and shown in Figure 5.2. The boundary condition of Equation 5.12 is the initial condition that allows for the electrons to initially collect on the surface of the conductor and eventually form a negative potential barrier. On the outside of the simulation domain, the potential is held at 0 V and the boundary conditions for the fluid elements utilize a Neumann condition as discussed in Chapter 5.

Figure 6.1 represents a comparison between our fully nonlinear warm plasma model and the analytical results of *Bohm* [1949]. Simulations were performed using all three warm plasma closure mechanisms outlined in Chapter 2. However, there were negligible differences between the simulation runs for the one-dimensional floating sheath since we are in an essentially linear regime. Thus, only the simulation results obtained by using the full non-adiabatic closure assumption represented by Equations 2.4a-2.4d are shown.

Figure 6.1 presents comparisons of our sheath model with that of *Bohm* [1949] for the potential, electron density and proton density variations, given by Equations, 6.3, 6.4a and 6.4b. It can be seen from the figure that our warm plasma results are in very good agreement with the analytical results, as to be expected for the case of a floating potential. The floating potential on the conducting surface as shown in Figure 6.1a is  $\Phi_{\text{wall}} \simeq -0.2$  V, which is slightly less than the background plasma potential.

Unlike the analytical results of *Bohm* [1949] which force a steady-state sheath condition, our simulations let this condition develop naturally in a self consistent manner. The total simulation time to reach the quasi-steady state condition represented by our model in Figure 6.1 was about  $t = 5$  ms which corresponds to 2000

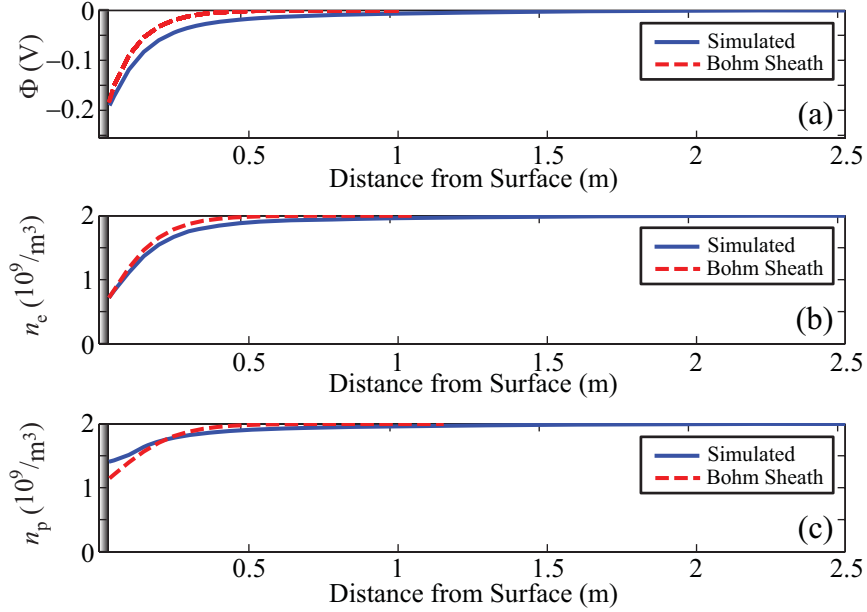


**Figure 6.1:** Comparison of 1-D planar sheath simulation with analytical results of Bohm. (a) Potential. (b) Electron number density. (c) Proton number density.

$\tau_{pe}$ , where  $\tau_{pe}$  is an electron plasma period equal to  $2.5 \mu\text{s}$  at  $L=2$ . If the 5 ms simulation time was to represent the period of an AC voltage source, the steady-state sheath would develop on scales corresponding to the period of a 200 Hz sine wave, a frequency far lower than the VLF range for the wave-particle interaction applications that motivate our study. In addition, with a plasma potential of  $\sim 0.2 \text{ eV}$  at  $L=2$ , application of even 1 V across the antenna elements would already imply a regime in which the linear analytical theory is not valid. For the collisionless plasma considered here, it is thus evident, based on the time-scales involved in sheath formation, that the distribution function never reaches the steady-state equilibrium described by the Boltzmann factor of Equation 6.1 for a source that is varying at VLF frequencies. This fact puts into serious question any analytical sheath derivations that utilize this Boltzmann factor for voltages in excess of the plasma potential, for anything other than DC applied potentials in a collisionless plasma, such as the work of *Song et al.* [2007]. On the other hand, collisions such as those present in a dense ionospheric plasma, could certainly aid in speeding up the relaxation of the distribution function

back to a Maxwellian state over time scales comparable to or less than the period corresponding to VLF frequencies [*Mlodnosky and Garriott, 1963; Baker et al., 1973*].

## 6.2 Two-dimensional Infinite Line Source

The purpose of the two-dimensional studies is two-fold. The first is to determine the importance of the proton dynamics in sheath formation. The second is to compare the various truncation schemes in order to gauge the importance of higher order moments in the fluid formulation for characterizing the time-varying sheath. In the interest of limiting the computational demands imposed by keeping the full heat-flux tensor in higher dimensions, we consider only the isothermal and adiabatic approximations for all subsequent 2-D simulation runs.

Using our validated fluid model, we examine the sheath structure surrounding a two-dimensional infinite line element. This study considers a two-dimensional infinite line source in an isotropic plasma with parameters corresponding to  $L=3$  where the ambient background number densities of the plasma are  $10^9 \text{ m}^{-3}$  for both species. We use an artificial proton-electron mass ratio of  $(m_p/m_e) = 200$ ; a commonly used practice in order to ease the computation burden [*Calder et al., 1993*]. The scaled proton plasma frequency in this case is  $f_p = 20 \text{ kHz}$ . The simulation uses Neumann boundary conditions for the fluid at the edge of the space and any particles hitting the line source are completely absorbed as in the planar sheath simulation of the previous section. A sketch of the simulation domain is shown in Figure 6.2.

We examine the time-varying sheath formation using a quasi-electrostatic approach as discussed earlier. This approach involves the use of Poisson's equation in which a sinusoidal potential is applied to the line element with a source frequency of  $f_s = 25 \text{ kHz}$  and peak potential of approximately 1000 times the background plasma potential, which is  $\sim 172 \text{ V}$ .

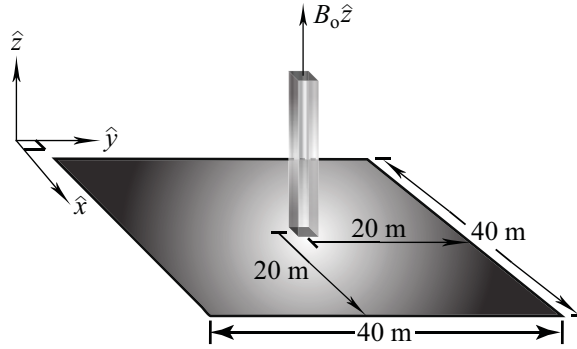


**Figure 6.2:** Conceptual drawing of two-dimensional simulation region.

### 6.2.1 Proton Dynamics

In order to determine the importance of the proton dynamics in sheath formation, we consider RF frequencies above and below the proton plasma frequency. To illustrate the density variations within the sheath, we assume an isotropic plasma and recognizing the resulting azimuthal symmetry, we take a vertical slice plane through the line element and plot the resulting potential and density profiles using a 1-D representation. Furthermore, we use the full adiabatic (3-moment) approximation for this purpose. A diagram of the slice plane is shown in Figure 6.3.

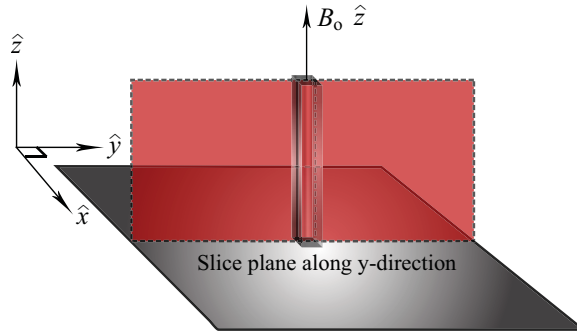


**Figure 6.3:** Slice plane through infinite line source.

At time  $t=0$  s, the sinusoidal potential starts with the positive cycle. During the initial transient response, the protons are pushed away from the line source while the electrons accelerate toward the antenna and are collected. Due to their inertia, and

the fact that the source frequency is in the vicinity of the proton plasma frequency, the majority of the protons traveling outward from the conductor cannot respond to the change in electric field as the potential switches to the negative portion of the cycle and are permanently displaced from the sheath region. This displacement forms an evacuated or proton-depleted region for which the only substantial current collection on the line element is now due solely to the electron response. Figure 6.4 depicts the potential and density profiles at two specific times during this initial transient response corresponding to the maximum and minimum potentials during the first cycle of the sinusoidal waveform represented by  $t^+$  and  $t^-$  respectively.

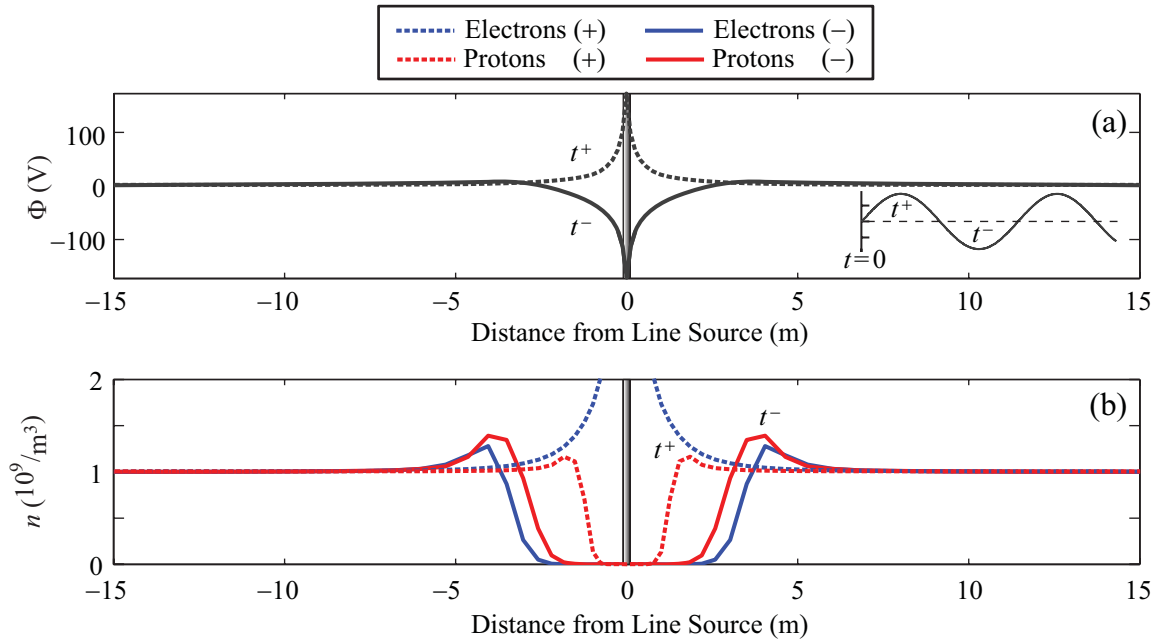


**Figure 6.4:** Transient response of 2-d simulation at  $L=3$ . The symbols  $t^+$  and  $t^-$  correspond to the first positive and negative peaks of the potential cycle for the 25 kHz sinusoidal source. All quantities shown by a dashed line correspond to  $t^+$  and all solid lines correspond to quantities at  $t^-$ . (a) Potential variation. (b) Electron and proton number densities.

During the negative potential cycle denoted by  $t^-$  in Figure 6.4, the electrons are pushed away from the sheath region, but due to their higher mobility, surpass the outward propagating proton wavefront. Since the tendency of the plasma is to neutralize any electric field perturbations that may exist, the electrons which exhibited

the initial overshoot relative to the outward propagating protons start to electrostatically shield the proton density perturbation, forming plasma frequency oscillations at the sheath edge. After several sinusoidal cycles, this double-layer ceases to exist, forming an outward propagating ion acoustic wave, which is shielded by the electrons and eventually leaves the space. This behavior is in stark disagreement with some analytical formulations in which the proton motion was neglected since it was thought that the much heavier mass of the protons would essentially make them immobile [Song *et al.*, 2007].

The steady state situation near the line element is represented by Figures 6.5 and 6.6 which display time snapshots of the potential and density profiles for the electrons and protons of our two species plasma after a number of periods of the 25 kHz applied potential (which is 5 kHz above the proton plasma frequency) by which time the response is periodic (except for the outward propagating density disturbance).

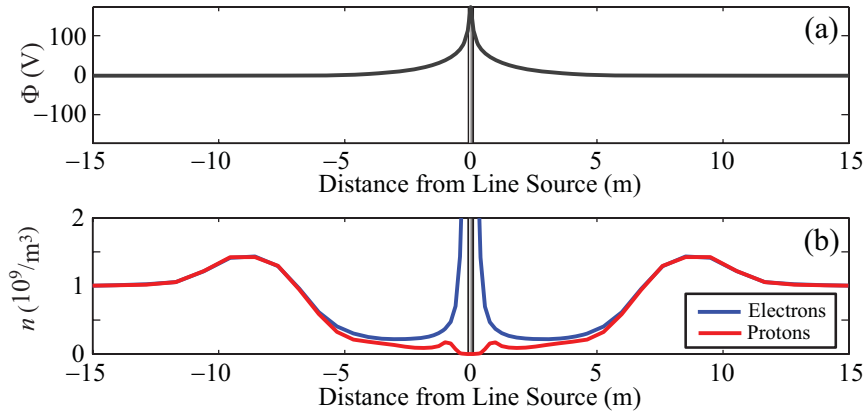


**Figure 6.5:** Snapshot during positive potential cycle of infinite line source.

During the positive cycle, the few ions that are left in the sheath region are repelled from the line element, whereas the electrons instantaneously react to the sinusoidal varying potential since the operating frequency is well below the electron plasma frequency being roughly  $f_{pe} = 284$  kHz at  $L=3$ .

At a much later time, the density disturbance exits the simulation domain and the electron and proton density profiles remain relatively unchanged at a distance of up to 7 meters from the conductor. Beyond this point, the number density of both

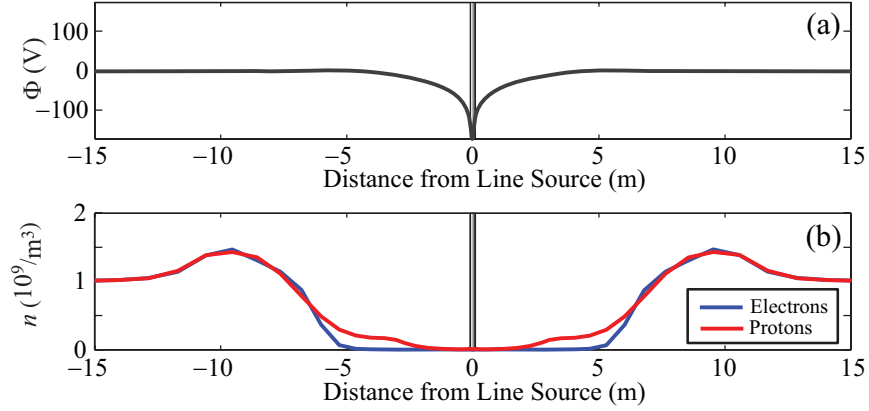


**Figure 6.6:** Snapshot during negative potential cycle of infinite line source.

species is approximately equal to the ambient density of the plasma.

## 6.2.2 Comparison of Isothermal and Adiabatic Closure Conditions for Sinusoidal Excitation

In this section, we compare the isothermal and adiabatic closure relations for an AC driven line element operating in both isotropic and magnetized plasmas by comparing the current-voltage characteristics on the infinite line element. We consider two frequencies that are 5 kHz above and below the proton gyrofrequency and for the magnetized plasma, the magnetic field is oriented along the axis of the element in the  $\hat{z}$ -direction.

Figures 6.7-6.10 represent the entire time-sequence for the voltage and current collection on the line element for a given RF applied potential for frequencies that are 5 kHz above and below the proton plasma frequency. The blue curves represent the isothermal approximation (2-moments) and the red curves represent the adiabatic approximation (3-moments) with the term mAdB indicating miliamps on a decibel scale.

The current  $I$  on the conductor is calculated by taking the integral around the closed surface  $\mathbf{S}$  defined by the exterior of the element. This integral is represented by Equation 6.6:

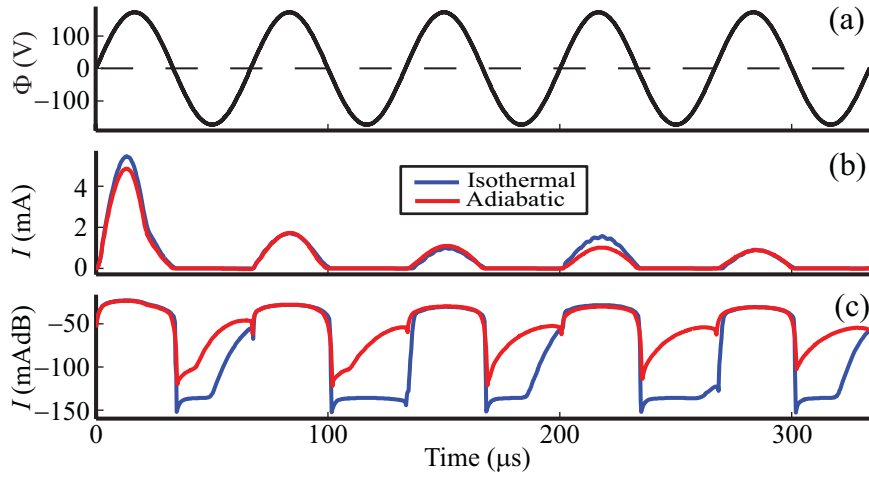


**Figure 6.7:** Current-voltage relationship for isotropic plasma with sinusoidal applied potential at 15 kHz. ‘Blue’ - 2 moments. ‘Red’ - 3 moments.

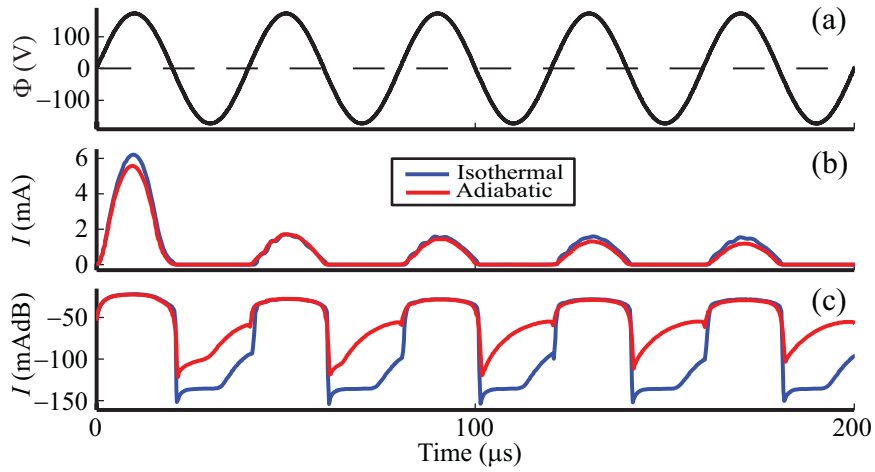


**Figure 6.8:** Current-voltage relationship for isotropic plasma with sinusoidal applied potential at 25 kHz. ‘Blue’ - 2 moments. ‘Red’ - 3 moments.

$$I = \oiint_S \mathbf{J} \cdot d\mathbf{S} \quad (6.6)$$

For the 2-D line source represented in Figure 6.2, Equation 6.6 amounts to a closed line integral in the  $\hat{x}$ - $\hat{y}$  plane representing a current per unit length.

Figures 6.7 and 6.8 represent the current collection on the line element assuming an

isotropic plasma. The current waveform is shown in both linear and log scales in order to illustrate the small contribution of the protons. Although the proton contribution to the current is negligible as seen per the rectified nature of the waveform, it is nevertheless non-zero. The other important point is that there is little difference between the isothermal and adiabatic approximations, suggesting that only a small number of moments are necessary in order to capture the relevant physics in sheath formation even under the collisionless assumption. This conclusion is supported by the earlier work of *Thiemann et al.* [1992] who compared both a 2-moment fluid code and a particle in cell (PIC) code with good qualitative agreement in a collisionless isotropic plasma.

Figures 6.9 and 6.10 include the effects of a static magnetic field oriented in the  $\hat{z}$ -direction as shown in Figure 6.2.

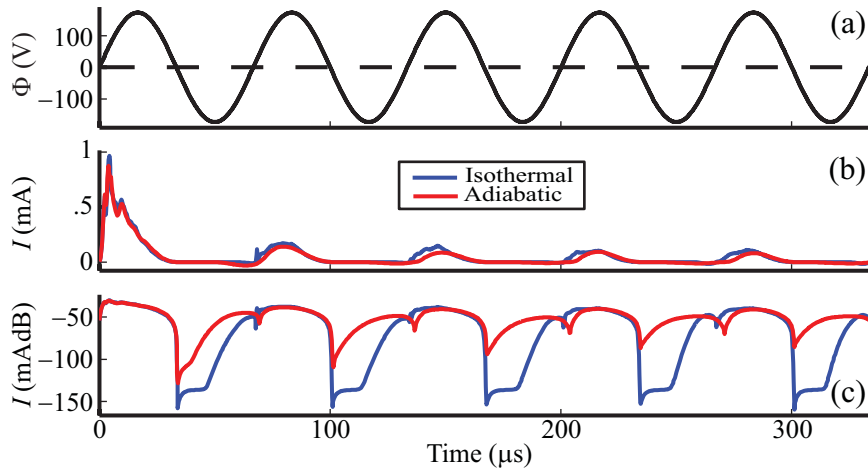


**Figure 6.9:** Current-voltage relationship for magnetized plasma with sinusoidal applied potential at 15 kHz. ‘Blue’ - 2 moments. ‘Red’ - 3 moments.

The inclusion of the magnetic field in the formulation has the effect of limiting the current flow to the line element, as expected since charged particles gyrate around magnetic field lines. The magnetic field has a much less pronounced effect on the proton collection as seen in the log scale plots of Figures 6.9-6.10. The more massive protons have a much larger gyroradius and therefore their contribution to the current collection is relatively unchanged between the cases with and without the static

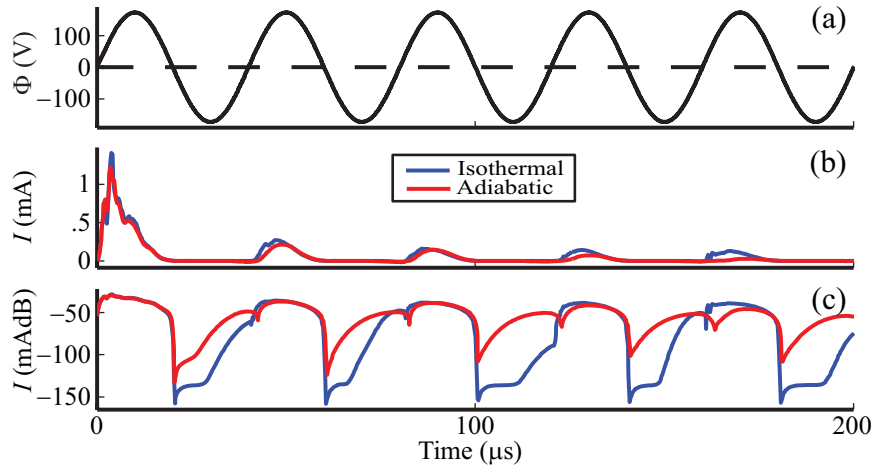


**Figure 6.10:** Current-voltage relationship for magnetized plasma with sinusoidal applied potential at 25 kHz. ‘Blue’ - 2 moments. ‘Red’ - 3 moments.

magnetic field.

### 6.2.3 Comparison of Isothermal and Adiabatic Closure Conditions for Pulse Train Excitation

The last set of 2-D comparisons is with respect to a pulse train in order to highlight the highly dynamic character of the sheath resulting from instantaneous changes in DC applied potentials. These results also illustrate the reason why the steady-state Boltzmann factor of Equation 6.1 is not valid for a collisionless plasma perturbed via DC applied potentials when driven at VLF frequencies.

Similar to the previous examples entailing sinusoidal applied waveforms, Figures 6.11-6.14 represent the entire time-sequence for the voltage and current collection on the line element operating at frequencies in the vicinity of the proton plasma frequency assuming an isotropic plasma with plasma density corresponding to  $L=3$ .

In the simulations represented by Figures 6.11-6.14, the same rectified behavior is present; however, the peaks of the current waveforms exhibit very strong plasma frequency oscillations that were also present in the simulations of *Calder and Laframboise* [1990], *Ma and Schunk* [1989], *Thiemann et al.* [1992] and *Ma and Schunk* [1992a,b]

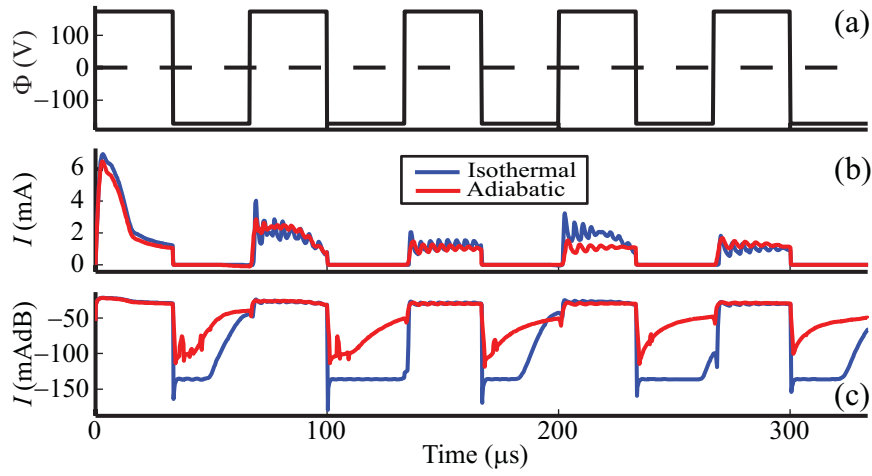


**Figure 6.11:** Current-voltage relationship for isotropic plasma with pulse train applied potential at 15 kHz. ‘Blue’ - 2 moments. ‘Red’ - 3 moments.

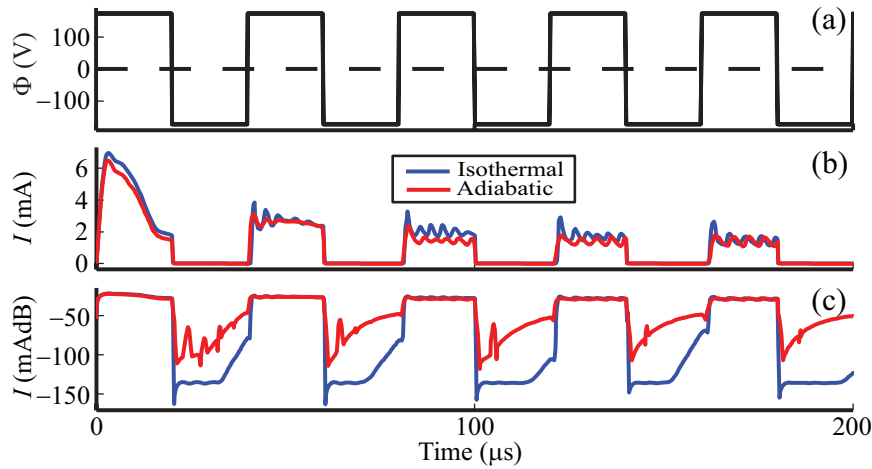


**Figure 6.12:** Current-voltage relationship for isotropic plasma with pulse train applied potential at 25 kHz. ‘Blue’ - 2 moments. ‘Red’ - 3 moments.

when studying current collection characteristics under DC applied potentials. The plasma ringing starts to decay over the length of the positive pulse and then reappears during the next cycle. Since the ringing is still evident even at frequencies below the proton plasma frequency, the system never reaches a steady state and therefore the Boltzmann factor of Equation 6.1 is not applicable at these frequencies. In addition, the peak current during the positive cycle for both the sinusoidal cases (Figures 6.7

and 6.8) and the pulse train cases (Figures 6.11 and 6.12) is roughly the same, being 1.5 mA at 15 kHz and 2 mA at 25 kHz, suggesting that the dominant factor governing the current collection is the fundamental driving frequency and not the form of the excitation.

We complete this section by including the effects of a  $\hat{z}$ -directed static magnetic field as shown in Figure 6.2. Figures 6.13 and 6.14 represent the current-voltage characteristics for this case, exhibiting the same decrease in current collection as with the sinusoidal waveform, once again resulting from the magnetic field inhibiting free-streaming particle flow. Even with the presence of the magnetic field which inhibits particle motion across field lines, the plasma frequency oscillations are still present.

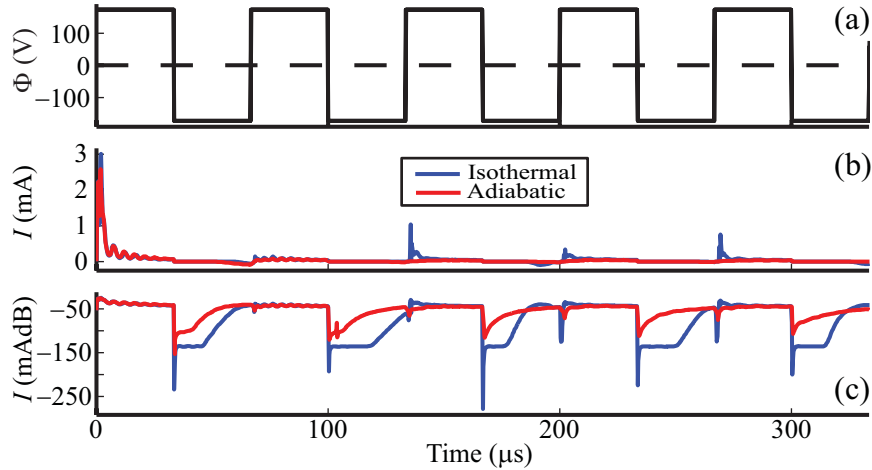


**Figure 6.13:** Current-voltage relationship for magnetized plasma with pulse train applied potential at 15 kHz. ‘Blue’ - 2 moments. ‘Red’ - 3 moments.

The major difference between the pulse and sinusoidal excitations other than the plasma ringing is in the transient current collection. When the potential is stepped to a DC value as opposed to slowly varying as in the sinusoidal case, the transient current draw is much larger during the first cycle of the waveform for both isotropic and magnetized plasmas.

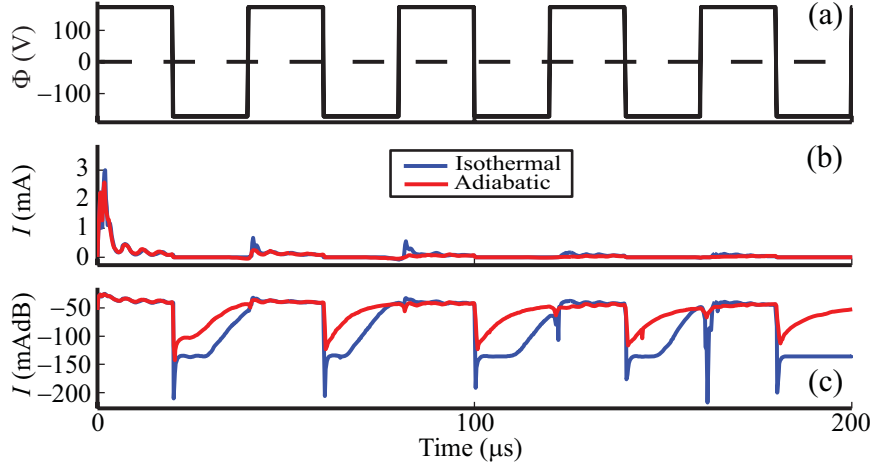


**Figure 6.14:** Current-voltage relationship for magnetized plasma with pulse train applied potential at 25 kHz. ‘Blue’ - 2 moments. ‘Red’ - 3 moments.

### 6.3 Three-dimensional Dipole Antenna

In this section we use our three-moment (adiabatic approximation) warm fluid code to examine the formation of the sheath surrounding a dipole antenna in a magnetized plasma in 3-dimensions. The electric dipole antenna considered is 20 m in length (tip-to-tip), 10 cm in diameter, and possesses a gap distance ranging from 20 cm to 2 m between the two antenna elements. For these simulations, we consider cases for which the operation of an electric dipole is under conditions corresponding to  $L=2$  and  $L=3$  in the geomagnetic equatorial plane. The antenna is excited using a sinusoidal inter-element potential difference of  $\sim 86$  V, approximately 500 times the background plasma potential which we denote as  $500\Phi_p$ . In addition, the same scaled proton-electron mass ratio of  $(m_p/m_e)=200$  is used as in the 2-D simulations. Only perpendicular antenna orientations with respect to the background magnetic field are considered as in the cold plasma simulation runs. Since there was virtually no difference in the behavior of the current collection for the 2-D cases for frequencies just above and below the proton plasma frequency, all 3-D simulation runs are performed at a frequency 5 kHz above the local proton plasma frequency, being 28.4 kHz and 20 kHz at  $L=2$  and  $L=3$  respectively for the scaled mass ratio of  $(m_p/m_e)=200$ .

As shown in Section 6.1, a floating conductor immersed in a plasma develops a

negative potential due to the high mobilities of the electrons. An electric dipole antenna experiences the same charging mechanism, if the collected charge is not removed from the antenna using, for example, an electron gun. However, unlike the floating wall, a transmitting antenna operating at high voltage relative to the background plasma potential accumulates a large number of electrons on the positively biased element during the sinusoidal cycle. This accumulation has the effect of producing a negative bias on the antenna elements that causes the entire system to drift to some negative DC potential. Instead of a symmetrically driven system, one of the elements is at a large negative potential while the other is at only a slight positive potential, forming asymmetric sheaths around the elements. In the following simulation runs, we examine a number of different scenarios by varying the plasma environment, gap spacing, and consider both a case for which an electron gun is used as well as that for which the electrons are allowed to accumulate (i.e., no electron gun).

As mentioned in Chapter 1, the actual location of the sheath ‘edge’ is quite arbitrary with no consensus on the defining criteria for this point [Franklin, 2004]. In this dissertation, we define the edge of the plasma sheath as a point in the field distribution at which the potential drops to within 10% of the maximum/minimum amplitude as shown in Figure 6.15.

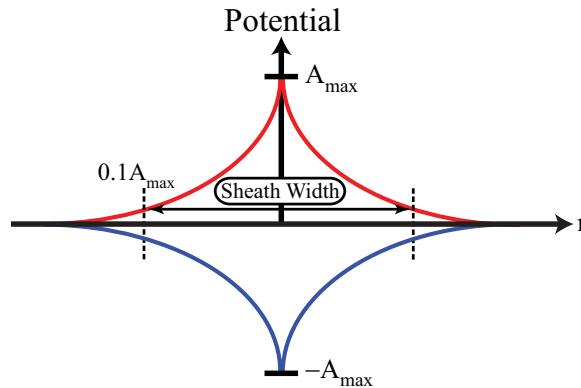


**Figure 6.15:** Diagram describing location of sheath edge.

This definition of the sheath edge provides a much more stable result since the densities are constantly varying during the sinusoidal cycle with electrostatic waves

propagating outward from the sheath region. The electrostatic potential distribution nevertheless remains periodic with the sheath edge remaining relatively unchanged throughout the simulation runs.

### 6.3.1 Antenna at $L=3$ with Electron Gun and 2 m Gap

In this first case study, we consider the antenna to be located in the equatorial plane at  $L=3$  and assume that an electron gun removes negative charge from the antenna. We initially start at  $L=3$  since the magnetic field is weaker and the Debye length is larger than the corresponding situation at  $L=2$ . Thus, the  $L=3$  scenario is slightly more reminiscent of an isotropic plasma. A sketch of the simulation region is shown in Figure 6.16, with the  $\hat{x}$ -directed background magnetic field oriented perpendicular to the antenna.

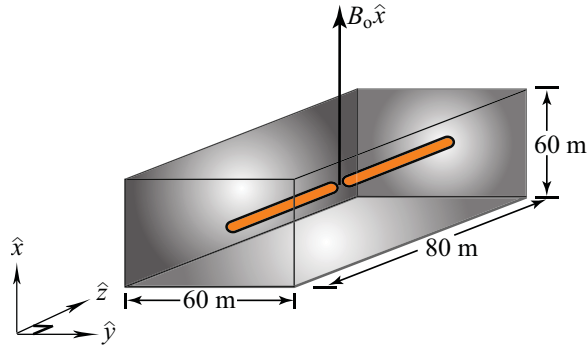


**Figure 6.16:** 3-dimensional computational domain at  $L=3$ .

As with Figures 6.5 and 6.6 from the 2-D runs of the previous section, we present a time-snapshot of the sheath during the peak of a sinusoidal cycle after a quasi-steady state has been reached. Figure 6.17 represents an orthographic projection of the sheath during the peak of the sinusoidal cycle after several periods in each slice plane. It can be seen from Figure 6.17 that the sheath is approximately 1 m wide and is virtually symmetric in each of the slice planes suggesting that the background magnetic field strength at  $L=3$  does not play much of a role in the steady-state formation of the sheath. On the other hand, it is clearly seen from Figure 6.17 that the sheaths are not the same size on each element. This disparity is due to the fact

that the expanding sheath does not instantaneously react to the applied voltage on the antenna, due to the mass difference and finite transit time of the protons and electrons through the sheath region. Therefore, the negative and positive sheaths surrounding each element fully expand to roughly the same size, but just not at the same time.

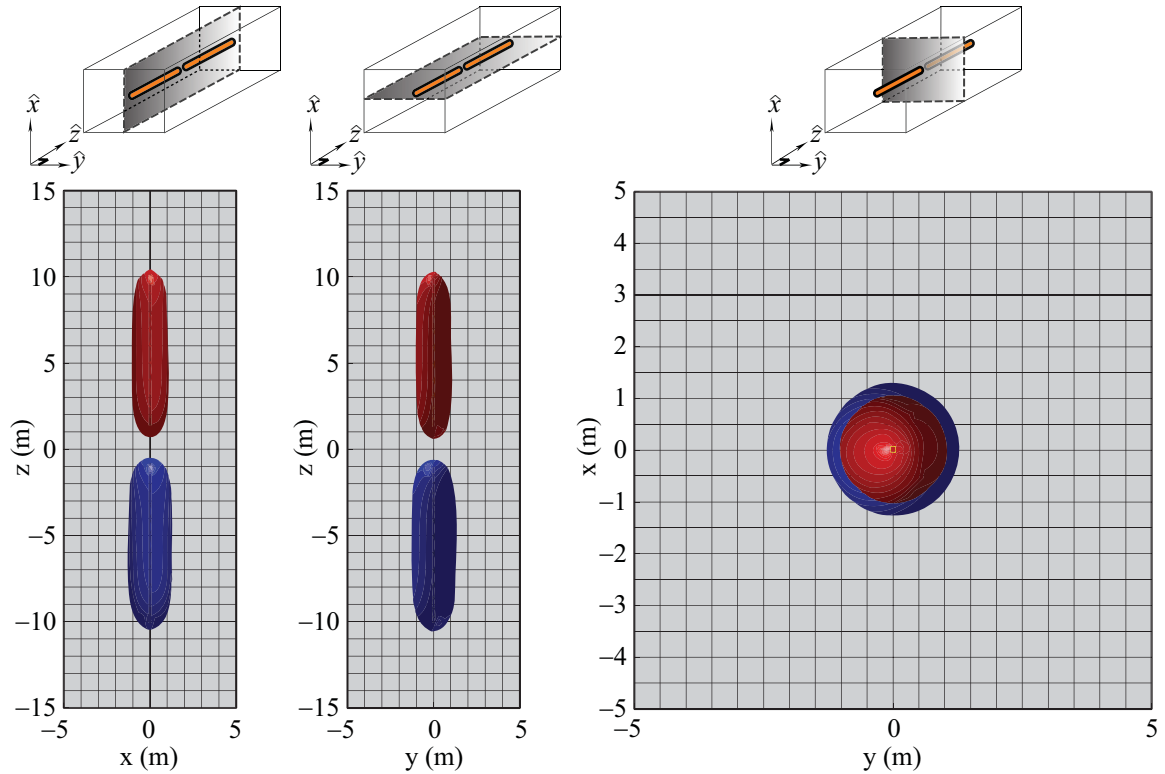


**Figure 6.17:** Orthographic projection of expanded sheath for  $L=3$  at maximum potential difference  $500\Phi_p$ . Operating frequency is at  $f=25$  kHz.

Figure 6.18 represents the 1-D variation of the potential and number density for a radial slice taken through the midpoint of one of the dipole elements in the  $\hat{x}$ -direction. Analogous to Figure 6.4, the steady-state density variations for each species during the negative and positive peaks of the sinusoidal cycle are shown. The steady-state situation represented in Figure 6.18 is reached after 5 periods of the waveform. Although the sheath itself is only 1 m wide as seen in Figures 6.17 and 6.18a, the presheath region, which is defined by the density profiles, extends several meters from

the conductor. However, the large outward propagating density perturbation seen in the 2-D simulations has all but vanished by this time as can be seen in Figure 6.18b.

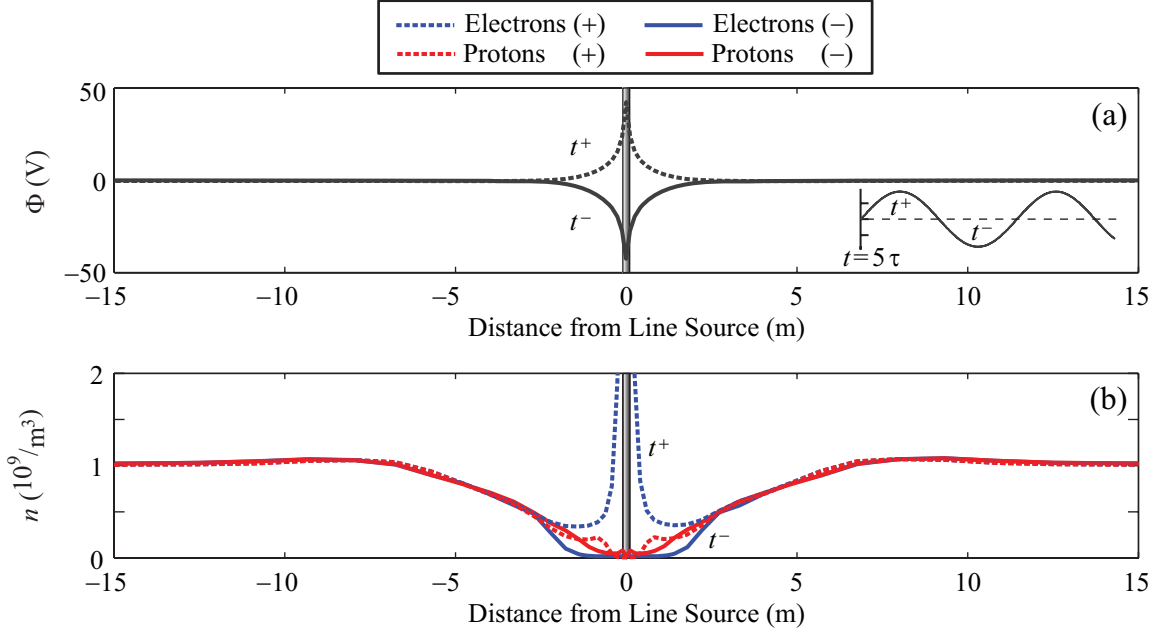


**Figure 6.18:** Electron and proton density variation for cross-section through midpoint of dipole antenna element at  $L=3$ . The symbols  $t^+$  and  $t^-$  correspond to the first positive and negative peaks of the potential cycle after 5 periods of the sinusoidal waveform. All quantities shown by a dashed line correspond to  $t^+$  and all solid lines correspond to quantities at  $t^-$ . (a) Potential variation. (b) Electron and proton number densities.

The time-domain waveforms in Figures 6.19a-6.19c represent the terminal characteristics for a single element of the dipole antenna located at  $L=3$ , including potential, current and charge. The current on the element is calculated using Equation 6.6 while the charge  $Q$  is calculated using Equation 6.7:

$$Q = \oiint_{\mathbf{S}} \epsilon_0 \mathbf{E} \cdot d\mathbf{S} \quad (6.7)$$

where  $\mathbf{E}$  is the *electric* field emanating from the dipole element. The charge is calculated by evaluating Gauss' law around the conductor where the electric field  $\mathbf{E}$  is obtained from the solution of Poisson's equation via  $\mathbf{E} = -\nabla\Phi$  where  $\Phi$  is the *potential* applied to the element.

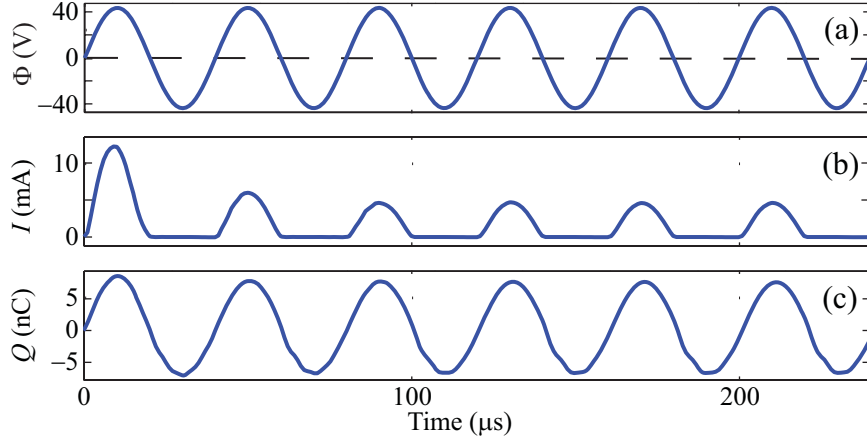


**Figure 6.19:** Terminal characteristics for 20 m antenna located at  $L=3$ . (a) Voltage. (b) Current. (c) Charge.

The presence of discontinuities in the current profile of Figure 6.19b produces high frequency content in the Fourier domain. As such, the resistance function, being highly nonlinear, would render the design of a tuning circuit, a challenging task. It is seen from Figure 6.19 that the transient behavior during initial sheath formation has subsided after the first excitation period. Figure 6.19b exhibits the same rectified sine wave behavior present in the 2-D simulations resulting from negligible proton current flowing to the dipole element.

In order to obtain a rough approximation of the steady-state sheath's contribution to the terminal properties of the dipole antenna, we calculate the time-domain root mean square (RMS) capacitance and resistance values using Equations 6.8a and 6.8b:

$$C_{\text{rms}} = \frac{Q_{\text{rms}}}{\Phi_{\text{rms}}} \quad (6.8a)$$

$$R_{\text{rms}} = \frac{\Phi_{\text{rms}}}{I_{\text{rms}}} \quad (6.8b)$$

where  $\Phi_{\text{rms}}$ ,  $I_{\text{rms}}$ ,  $Q_{\text{rms}}$ ,  $C_{\text{rms}}$  and  $R_{\text{rms}}$  are the RMS values of *potential*, *current*, *charge*, *capacitance* and *resistance* respectively. Substituting the RMS values inferred from Figure 6.19 into the formulas given by Equations 6.8a and 6.8b, the time-domain capacitance and resistance values at the driving frequency of 25 kHz are roughly  $C \sim 169$

pF and  $R \sim 13.7 \text{ k}\Omega$  respectively, thus it can be concluded that the sheath dominates the tuning characteristics of the antenna relative to the cold plasma impedance calculations of Chapter 4.

It is important to note that due to the nonlinear nature of the sheath, capacitance and resistance values used for tuning purposes are only valid for the peak sinusoidal voltage at which the transmitter is driven. Therefore, separate simulation runs would need to be made to calculate the sheath's contribution to the terminal impedance properties for each excitation waveform and driving potential used for a particular plasma environment.

To complete the sheath analysis of the dipole antenna at  $L=3$ , Figure 6.20 represents a plot of the time-domain current flowing within the center of the gap between the elements. The current is determined by integrating the flux of particles flowing through a cross section with radius equal to the sheath width, being 1 m in this case. Results from this calculation allow us to determine the importance of inter-element current flow on the total current moment of the antenna so as to ascertain whether or not the dipole elements should be spaced at some minimum distance to prevent adverse effects on the radiation resistance.

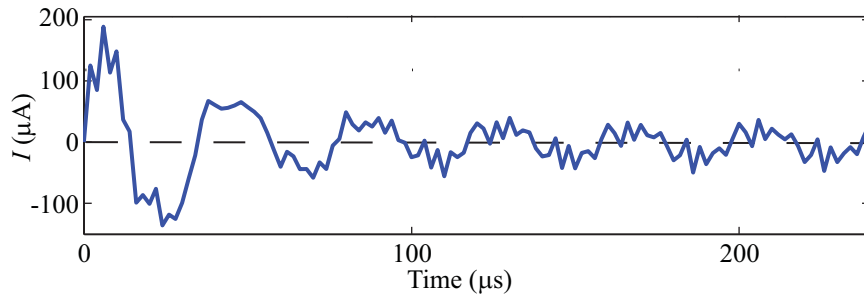


**Figure 6.20:** Inter-element gap current for dipole antenna at  $L=3$ .

From Figure 6.20, it is seen that after the initial transient has diminished ( $\sim 60 \mu\text{s}$ ), a steady-state current is reached, having a peak value of approximately  $40 \mu\text{A}$ . In the next few sections, we compare this value of the gap current with that of dipole antennas possessing a smaller gap spacing, floating potential, and operating in more dense plasma environments.

### 6.3.2 Antenna at $L=2$ with Electron Gun and 2 m Gap

The next case study is that of an electric dipole antenna located at  $L=2$  where the magnetic field is more appreciable than that at  $L=3$ . Since the Debye length is smaller at  $L=2$  with a number density that is approximately a factor of two larger, the computational domain is slightly smaller in size. A sketch of the simulation region is shown in Figure 6.21.

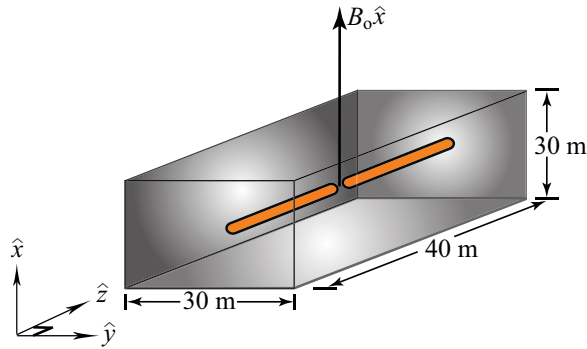


**Figure 6.21:** 3-dimensional computational domain at  $L=2$ .

Although not shown here, one major difference between the runs at  $L=2$  and  $L=3$  is during the initial transient response in which the transient sheath expands along the field line. However, the steady-state sheath (reached after a few sinusoidal cycles) is virtually the same as that found at  $L=3$  with only a very slight increase in the amount of asymmetry along the slice planes. Figure 6.22 represents the corresponding orthographic projection of the fully expanded sheath for the case at  $L=2$ .

The sheath structure as shown in Figure 6.22 exhibits some minor differences over the previous simulation run at  $L=3$ . The radius of the sheath surrounding the negative element is  $\sim 1$  m again, whereas the sheath around the positive element is closer to 1.5 m along the  $\hat{x}$ -direction which corresponds to the direction of the magnetic field. In the  $\hat{y}$ -direction however, which is perpendicular to the magnetic field, the sheath radius is slightly smaller for both elements. This difference is due to the magnetic field and not the finite transit time as discussed in the previous section. The larger magnetic field strength at  $L=2$  has the effect of decreasing the electron gyroradius from  $\sim 85$  cm at  $L=3$  to  $\sim 25$  cm at  $L=2$  for electrons traveling at the

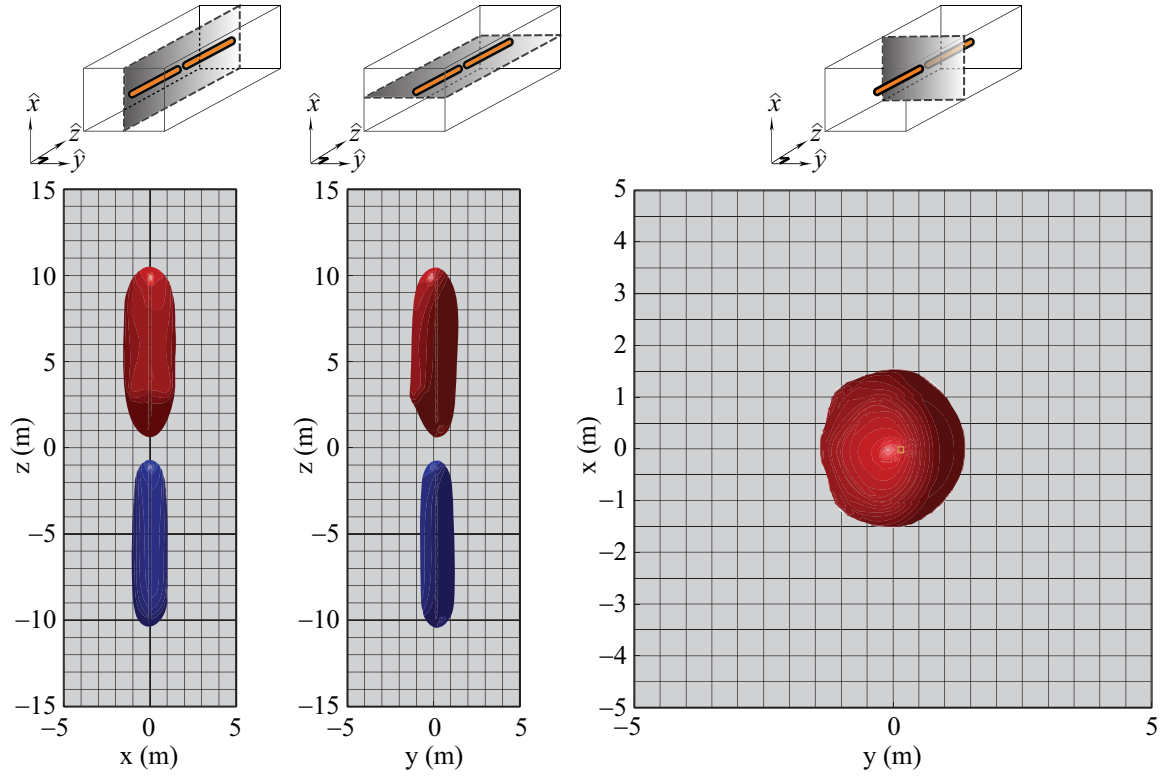


**Figure 6.22:** Orthographic projection of expanded sheath for  $L=2$  at maximum potential difference  $500\Phi_p$ . Operating frequency is at  $f=33.4$  kHz.

thermal velocity. Thus any electrons traveling close to the thermal velocity have a gyroradius that is smaller than the sheath radius and therefore do not travel along straight lines toward the antenna elements, thus producing the deviation from axial symmetry. At  $L=3$ , both the positive and negative sheaths surrounding the elements expand and contract at roughly the same time; however at  $L=2$ , the positive sheath expands and contracts at a rate quicker than the sheath surrounding the negative element. Though the negative sheath takes more time to fully expand, it persists for a longer duration of time for the following reasons. After the periodic steady-state sheath has developed, the ions are pushed away during the positive cycle while the electrons at the edge of the sheath are attracted. However, due to the smaller gyroradius of the electrons and weak electric field at the sheath boundary, the electron motion across the magnetic field lines is hindered, decreasing the total number of

electrons that are able to shield the positive potential. For a negative applied potential however, the electrons within the sheath region experience a much stronger force and possess a larger gyroradius as a result, and are thus quickly repelled from the antenna without their trajectories being significantly altered by the magnetic field.

The effect of the magnetic field on the density profiles is readily seen in Figure 6.23 which represents a slice plane through the center of one of the dipole elements depicting the potential and number density variations for each species.

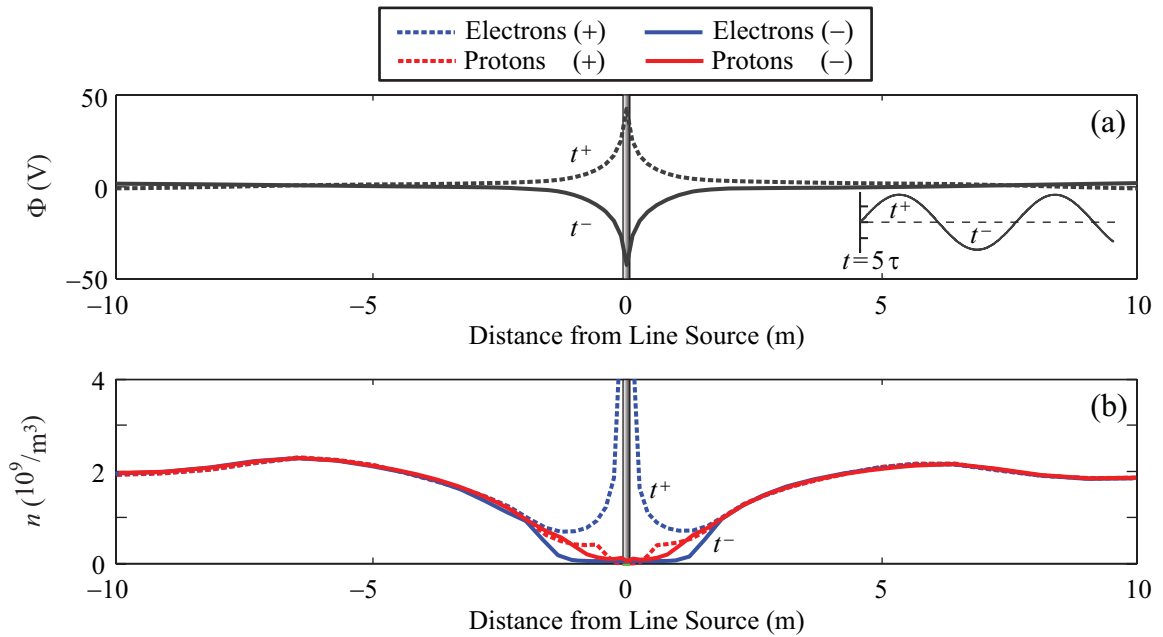


**Figure 6.23:** Electron and proton density variation for cross-section through midpoint of dipole antenna element at  $L=2$ . The symbols  $t^+$  and  $t^-$  correspond to the first positive and negative peaks of the potential cycle after 5 periods of the sinusoidal waveform. All quantities shown by a dashed line correspond to  $t^+$  and all solid lines correspond to quantities at  $t^-$ . (a) Potential variation. (b) Electron and proton number densities.

The smaller shielding distance resulting from the smaller Debye length can be seen in Figure 6.23b where the protons and electrons follow the same density profile beyond a distance of 2 m, as opposed to roughly 3 m as seen in Figure 6.18 for the case at  $L=3$ . A new feature that results from the larger magnetic field at  $L=2$  is the bunching of particles beyond the edge of the sheath region at a distance of  $\sim 7$  m where the densities of both the protons and electrons are larger than the ambient value of  $2 \times 10^9$

$\text{m}^{-3}$ .

Figure 6.24 is a plot of the terminal properties for the dipole antenna located at  $L=2$ . It can be seen from the figure that the current-voltage characteristics are similar to the case study at  $L=3$  with a slightly larger peak current of 6 mA versus 5 mA at  $L=3$ .

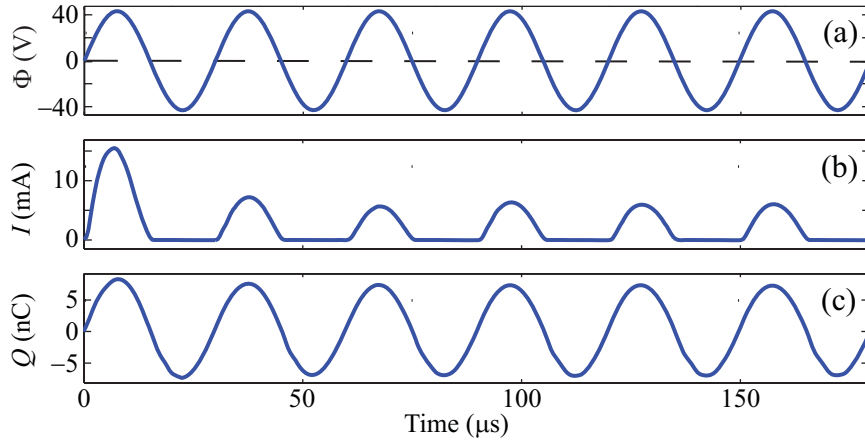


**Figure 6.24:** Terminal characteristics for 20 m antenna located at  $L=2$ . (a) Voltage. (b) Current. (c) Charge.

In Figure 6.24c, a similar value in peak charge accumulation ( $\sim 8$  nC) at the driving frequency of 33.4 kHz is seen relative to the case at  $L=3$  represented by Figure 6.19c. The RMS capacitance and resistance values derived from the terminal characteristics depicted in the waveforms of Figure 6.24 at the driving frequency of 33.4 kHz for the antenna located at  $L=2$  are 169 pF and 9.95 k $\Omega$  respectively for the element shown.

The inter-element gap current of Figure 6.25 shows a significant difference in the transient behavior relative to the corresponding case at  $L=3$  with the current being larger at steady-state than during the initial few periods. This effect can be attributed to the large magnetic field hindering the initial flow of electrons through the gap which dominate the current response due to their high mobility. Instead of freely flowing back and forth between the elements as in Figure 6.20, the particles gyrate around the field lines and take a greater duration of time to reach steady-state behavior. The steady-state gap current at  $L=2$  is not established for about 4 periods as opposed to only 3 periods for the dipole antenna at  $L=3$ . The greater magnitude of the current

relative to the corresponding case at  $L=3$  can be attributed to the larger density of particles in this region of space.

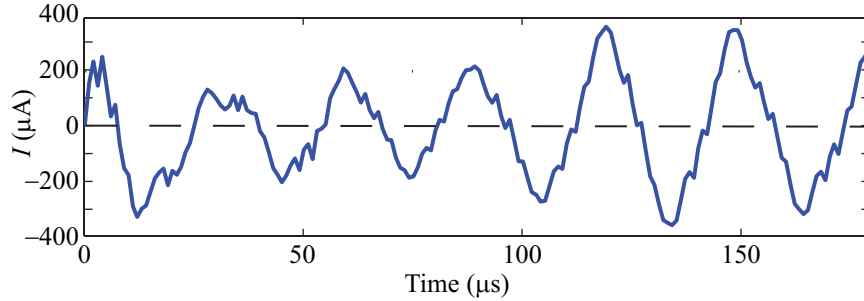


**Figure 6.25:** Inter-element gap current for dipole antenna at  $L=2$ .

### 6.3.3 Antenna at $L=3$ with Electron Gun and 20 cm Gap

For this next case study, we examine the sheath and terminal characteristics of a dipole antenna with an inter-element gap that is 20 cm in width. As alluded to earlier, it is possible that with elements that are not as electrically isolated in the plasma as those with a larger gap spacing, substantial currents may flow from one dipole element to the other. Such a short circuit current could potentially cause a significant decrease in the radiation resistance of the antenna, with most of the radiation being produced by a current flowing across a very small area. This case study aims to assess the importance of this short-circuit effect.

For this purpose, we assume an operating environment corresponding to  $L=3$  with a simulation space that is identical to that shown in Figure 6.16 with the only difference being the decrease in gap separation. Figure 6.26 represents the orthographic projection of the sheath for this case with results that are not markedly different from the case study at  $L=3$  with the 2 m gap separation.

In fact, the sheaths surrounding the positive and negative elements are virtually identical to those for the larger gap spacing with the only difference being the separation distance. Likewise, the potential and number density variations represented in Figure 6.27 at the peak of a steady-state sinusoidal cycle are very similar to the

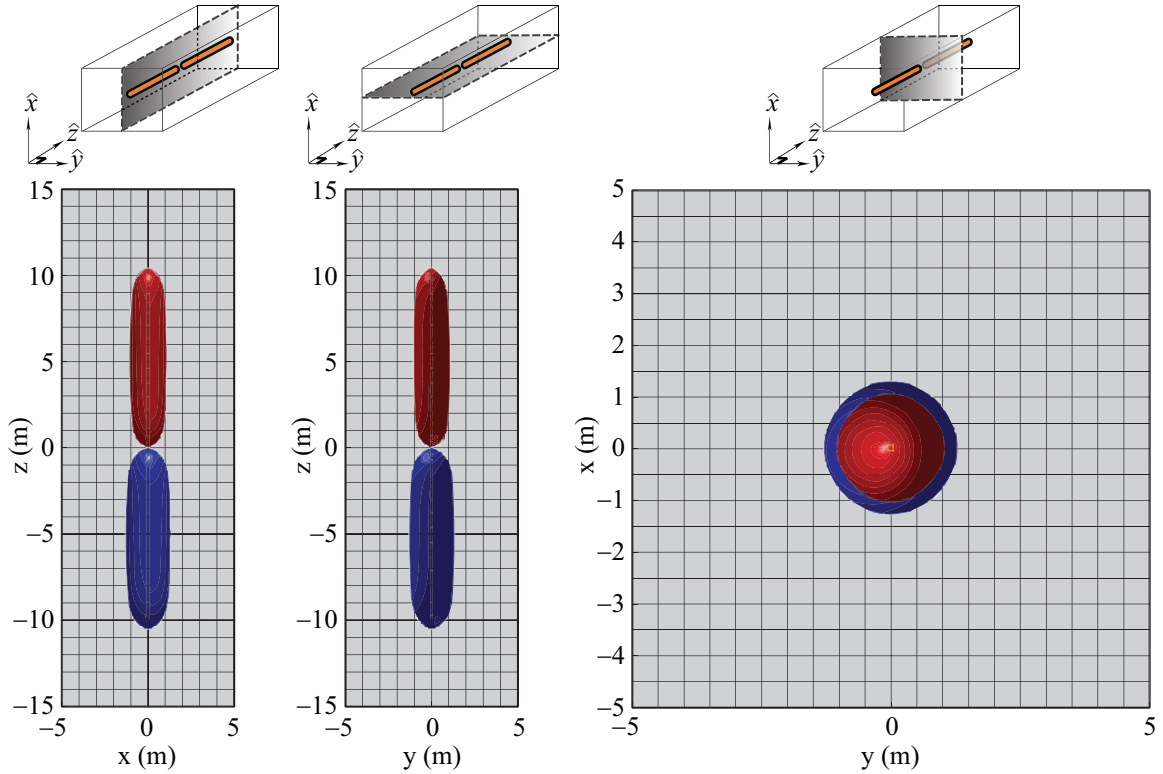


**Figure 6.26:** Orthographic projection of expanded sheath for  $L=3$  with 20 cm gap at maximum potential difference  $500\Phi_p$ . Operating frequency is at  $f=25$  kHz.

baseline case with the 2 m gap. This negligible difference in density and sheath profiles between the two cases is likely due to the fact that the small gap spacing only effects the profiles near the terminals of the dipole elements.

Along with the density and potential variations shown in Figure 6.27, the RMS capacitance and resistance values determined from the terminal characteristics represented in Figure 6.28 are very similar to those found for the larger gap spacing, with values of  $C \sim 187$  pF and  $R \sim 13.5$  k $\Omega$  at the driving frequency.

On the other hand, we might expect to see a significant difference between the two cases at  $L=3$  in the time domain gap current plot of Figure 6.29. With the smaller gap separation, the electric field is much larger since the potential difference between the two antennas is over a distance that is a factor of 10 less for the case presented here. Surprisingly enough however, it can be seen from Figure 6.29 that the inter-element

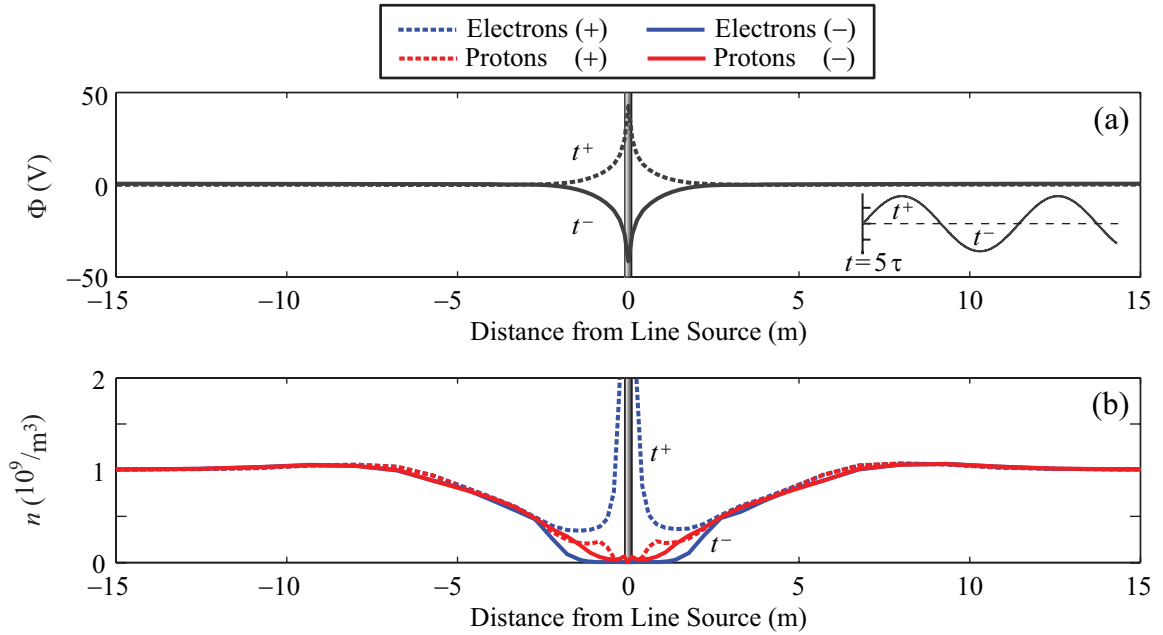


**Figure 6.27:** Electron and proton density variation for cross-section through midpoint of dipole antenna element at  $L=3$  with 20 cm gap. The symbols  $t^+$  and  $t^-$  correspond to the first positive and negative peaks of the potential cycle after 5 periods of the sinusoidal waveform. All quantities shown by a dashed line correspond to  $t^+$  and all solid lines correspond to quantities at  $t^-$ . (a) Potential variation. (b) Electron and proton number densities.

gap current is roughly the same as that for antenna with the 2 m gap separation, still being  $\sim 40 \mu\text{A}$ . Although the velocity of the fluid element is undoubtedly larger due to the increase in electric field strength, this proportional increase in current is likely offset by the smaller density of particles present between the terminals of the antenna. This balance between density and field strength results in a current that is equivalent to that which is found in the case of antenna with a 2 m gap separation. We can conclude on this basis that a small inter-element gap spacing does not have a detrimental effect on the current moment of the antenna versus that with a large gap separation.

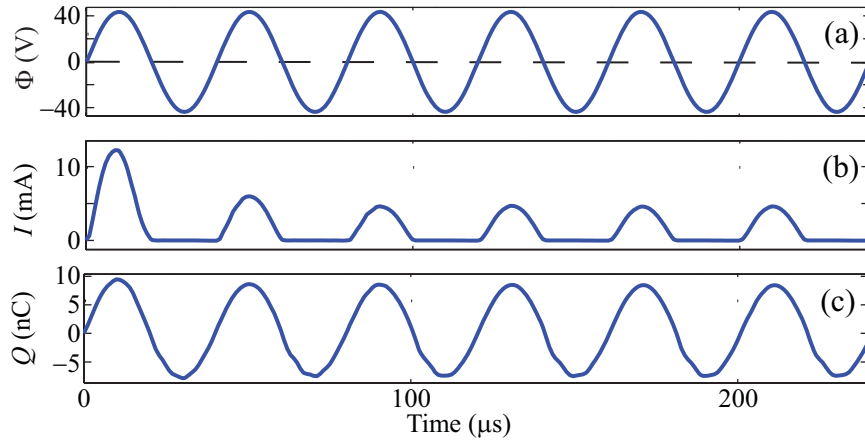


**Figure 6.28:** Terminal characteristics for 20 m antenna located at  $L=3$  with 20 cm gap. (a) Voltage. (b) Current. (c) Charge.

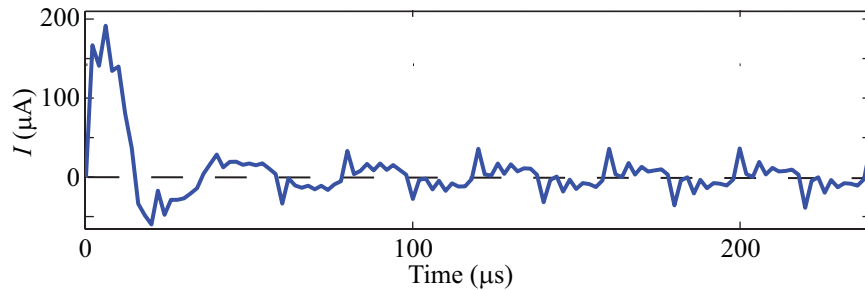


**Figure 6.29:** Inter-element gap current for dipole antenna at  $L=3$  with 20 cm gap.

### 6.3.4 Antenna at $L=3$ without Electron Gun and 2 m Gap

The final case study is that of a dipole antenna with no electron gun present, allowing for charge buildup on the antenna surface. Analogous to the case of a floating conductor in a plasma, this net negative charge buildup due to the higher mobility of the electrons has the effect of producing a net negative potential bias on both elements of the antenna since they are electrically connected through the internal circuitry of the space-craft. This negative drift is readily seen in the orthographic projections of the sheath shown in Figure 6.30. As seen in Figure 6.30, the positive sheath is relatively small, being  $\sim 0.5$  m in radius, while the negative sheath has a radius of  $\sim 1$  m. The asymmetry between the positive and negative sheaths is most readily seen in Figure

6.31 representing the 1-D potential and density variation through one of the elements.

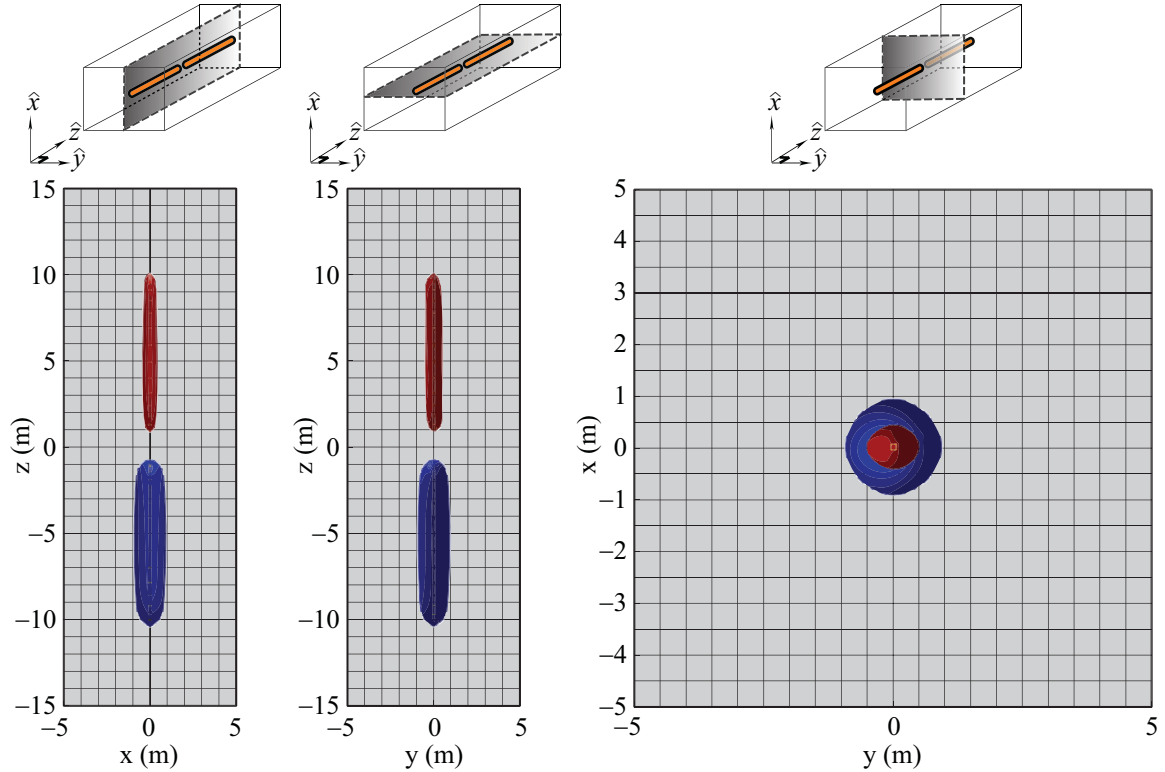


**Figure 6.30:** Orthographic projection of expanded sheath for  $L=3$  without electron gun at maximum potential difference  $500\Phi_p$ . Operating frequency is at  $f=25$  kHz.

The major difference between the floating dipole and that in which an electron gun is used is in the current collection due to the electron contribution on the element as shown in Figure 6.31b. Because the antenna system is allowed to drift to a large negative potential, it does not collect as many electrons during the positive potential cycle. However, because of the large negative bias, the number of protons collected on the antenna surface is much larger than that for the non-floating case, contributing to the small positive voltage seen in Figure 6.31a.

The potential difference between the two elements is governed by the voltage-source, although without the removal of excess charge, the entire system operates primarily in a negative voltage regime. Figure 6.32 shows the time-domain terminal characteristics for both elements of the dipole antenna. As seen in Figure 6.32a, the

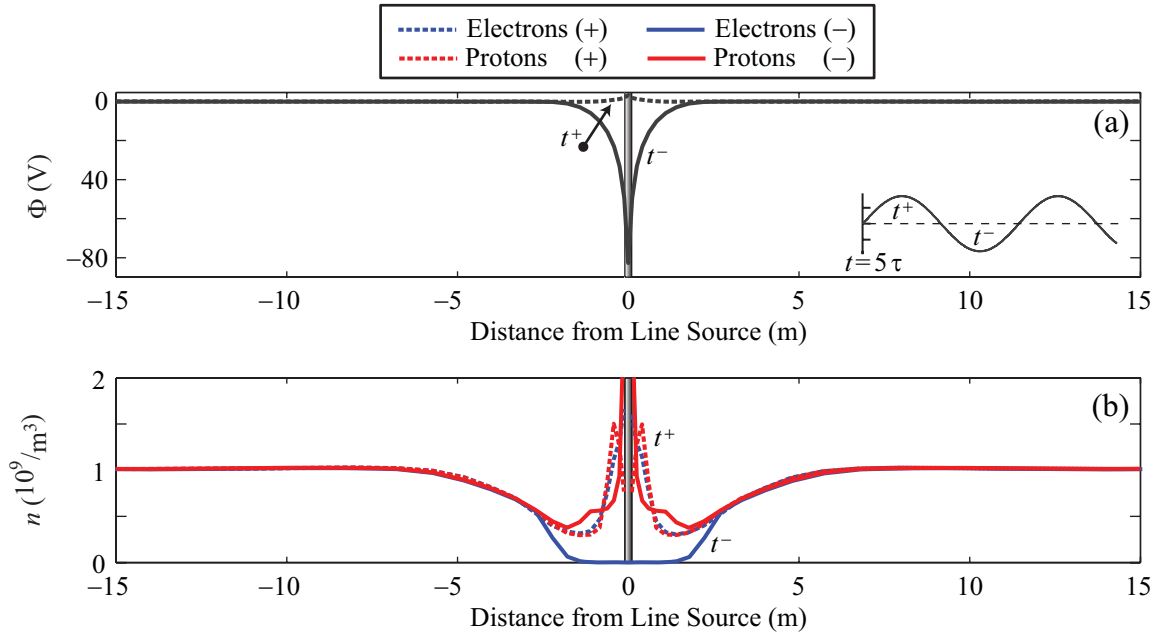


**Figure 6.31:** Electron and proton density variation for cross-section through midpoint of dipole antenna element at  $L=3$  without electron gun. The symbols  $t^+$  and  $t^-$  correspond to the first positive and negative peaks of the potential cycle after 5 periods of the sinusoidal waveform. All quantities shown by a dashed line correspond to  $t^+$  and all solid lines correspond to quantities at  $t^-$ . (a) Potential variation. (b) Electron and proton number densities.

potential on Element #1 stays just above 0 V during the first half cycle, while Element #2 drifts to a potential that is approximately twice the peak sinusoidal amplitude of the waveform. The voltage in Figure 6.32a is highly nonlinear, oscillating between the positive potential of only several volts, to a large negative potential, with the potential difference between the two elements equal to the 25 kHz driving sinusoid as shown in Figure 6.32b. The current waveforms for both elements, shown in Figure 6.32c, are vastly different than the electron-gun case where it is seen that a large flux of protons is clearly hitting the antenna, unlike the previous case studies in which the current waveform resembled a rectified sinusoid. This large proton flux is also seen in Figure 6.31b where there is a significant proton density adjacent to the antenna during both negative and positive cycles, exceeding that of the electrons. In fact, the proton current at steady-state, represented by  $I < 0$  in Figure 6.32c, is roughly equal

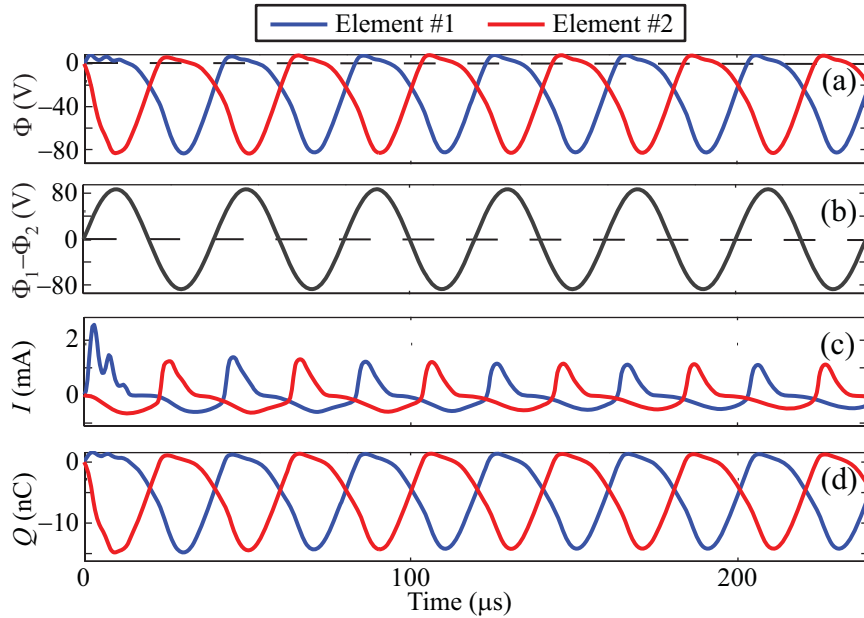


**Figure 6.32:** Terminal characteristics for 20 m antenna located at  $L=3$  without electron gun. (a) Voltage. (b) Inter-element potential difference. (c) Current. (d) Charge.

to half of the contribution due to the electrons, showing a significant increase over previous case studies.

Although the RMS capacitance value is only slightly different from that of the previous case studies, the RMS resistance is significantly larger due to the reduced electron flux through the surface of the dipole element resulting from the negative potential bias of the system. The RMS capacitance and resistance values at the 25 kHz driving frequency for this floating dipole antenna are 177 pF and 107 k $\Omega$  respectively with the resistance value exhibiting a significant deviation from the previous calculations which utilized an electron gun.

Finally in Figure 6.33, we examine the gap current for the floating dipole antenna. The gap current waveform is very similar to that of the other  $L=3$  case studies except that the magnitude is down by a factor of two being approximately 20  $\mu\text{A}$ .

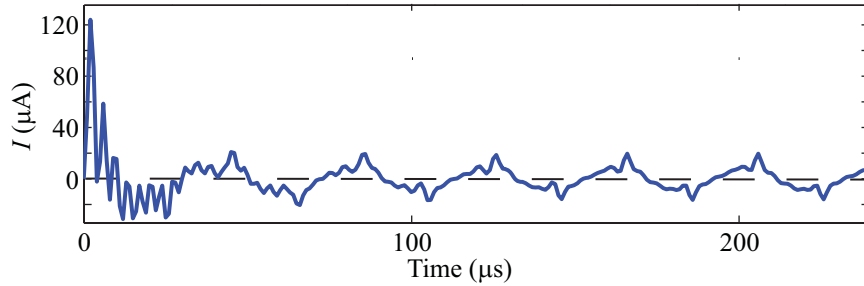


**Figure 6.33:** Inter-element gap current for dipole antenna at  $L=3$  without electron gun.

### 6.3.5 Antenna Tuning

In all of the cases considered, the nonlinear structure of the sheath is readily apparent in terms of the terminal characteristics and hence, tuning properties. For the sinusoidal waveforms considered, the structure of the sheath does exhibit a steady-state nature with each of the dipole elements possessing very similar characteristics in terms of voltage, charge and current draw. Thus one might expect, based on our findings, that the tuning circuit used to maximize the power delivered to the antenna would be the same for each dipole element, albeit complicated. It is also clear from our warm plasma findings that for frequencies above  $f_{LHR}$ , the complex impedance of the antenna is dominated by the sheath characteristics as opposed to the almost perfectly tuned antenna that the cold plasma model predicts. As such, the results presented in our warm plasma model constitute one of the first complete attempts to determine the plasma sheath contribution to the near-field antenna-plasma coupling response. This coupling would need to separately be determined for every driving potential and frequency content of the source excitation waveform considered as well as for each environment in which the antenna will be operating. Though the capacitance and resistance values calculated in this section are not meant to be used in practical design implementation, they do provide a first order approximation of the sheath's impact on tuning requirements. The generality of our simulation tool allows for its use in determining the near field coupling of antennas of arbitrary geometry and operating environments making it a flexible and useful tool in future antenna design and analysis.

# Chapter 7

## Summary and Suggestions for Future Work

In this dissertation, we have addressed the near-field coupling of electric dipole antennas to a collisionless magnetized plasma using a multi-moment fluid approach. The first approach entailed the development of both time and frequency cold plasma electromagnetic models to determine the current distribution and terminal impedance of an electric dipole antenna without considering the sheath. The second approach involved the development of a nonlinear warm plasma electrostatic model to determine the effects of the plasma sheath on the terminal characteristics of electric dipole antennas.

### 7.1 Cold Plasma Model Contributions

We have illustrated some of the difficulties in modeling electromagnetic wave propagation in a magnetized plasma and have verified an important assumption inherent in past analytical work, namely the assumed current distribution along the dipole antenna. The current distribution appears to be triangular for virtually all cases shown at whistler-mode frequencies and our results for the terminal impedance of the dipole antennas studied here agree well with those of past analytical work. It has also been shown that for the cases of longer antennas and higher plasma frequencies,

the current distribution exhibits exponential decay along the length of the element for antenna orientations that are perpendicular to the static background magnetic field. It should also be noted that the antennas at both  $L=2$  and  $L=3$  seem to be self tuning for the frequencies simulated above  $f_{\text{LHR}}$  in that the reactive part of the impedance shown in Figures 4.6 and 4.8 are virtually zero across the range given. With the current distribution thus verified to be triangular, the results of *Wang and Bell* [1972a] can be used to determine the power radiation pattern since the pattern should be unaffected by the near-field contribution of the sheath.

The cold plasma model represents an initial step in the development of a more complete (in terms of the underlying physics) electromagnetic code to self-consistently solve for both the near and far fields generated by electric dipole antennas. The numerical methods including the PML boundary condition utilized herein resolve a number of difficult challenges which are not specific to a cold plasma environment. As such, this work also represents an advance in the numerical study of electromagnetic wave propagation in a magnetized plasma in particular, or more generally for arbitrary anisotropic media.

## 7.2 Warm Plasma Model Contributions

The cold plasma model was the simplest approximation used, and from the results we were able to verify that an electrostatic approximation is valid for the simulation of the near field-properties of antennas operating in an anisotropic environment with high refractive indices. With the addition of the warm plasma fluid equations, we gained the capability of examining the formation of the electrostatic sheath and were able to draw a number of conclusions based on these results. The first result is that sheath structure is periodic using a sinusoidal waveform excitation, exhibiting a quasi-steady state structure. In addition, we have shown that the Boltzmann factor is not adequate in describing the density modification to the distribution function under AC applied potentials in a collisionless plasma. We find that the common assumption of immobile protons used in past work is incorrect, and that the density of protons varies significantly throughout the sheath region and contributes to the current collection.

Lastly, we have shown that not only does the sheath dominate the tuning properties of the antenna, but that the time-varying resistance and capacitance throughout the RF cycle do not vary by orders of magnitude as suggested by previous authors [*Mlodnosky and Garriott*, 1963; *Baker et al.*, 1973; *Song et al.*, 2007].

## 7.3 Suggestions for Future Research

Although the application of our models is specific to particular magnetospheric locations, the AIP code itself is very general, allowing for electromagnetic and electrostatic simulations in many types of isotropic and anisotropic media. We have gained a great deal of insight into the operation of electric dipole antennas in a magnetoplasma; however, there are still a number of areas in which the capability of our AIP code can be extended.

### 7.3.1 Adaptive Mesh Refinement

The current modeling methodology utilizes a non-uniform Cartesian grid for both the warm and cold plasma simulation tools. For explicit time-integration methods, the time-step is constrained by the maximum velocity in the space and the smallest cell size used. Therefore, to remain stable, the largest time-step for the entire computational domain is limited by the smallest cell size. For the frequency domain methods presented in Chapter 3, the convergence rate is in part, subject to these same constraints. In addition, the small cell sizes are only used to capture the detailed geometry of the object in the center of the domain, i.e. the antenna, but are not needed toward the outside of the domain. However, in a highly anisotropic medium such as a plasma with refractive indices which vary as a function of both frequency and wave normal angle with respect to the static magnetic field, it is difficult to determine in advance where to apply the resolution need to capture the small wavelengths that may exist within the simulation region.

An Adaptive Mesh Refinement (AMR) strategy would prove to be quite beneficial for this purpose. AMR only applies refinement where necessary such as in areas with

large spatial gradients in the solution or to capture the geometry of an object placed within the computational domain. The time-stepping algorithm used in an AMR methodology only applies time steps that are proportional to the local cell size in the subdivided region. Therefore, where the space is locally refined, the AMR package super-cycles the time step in that local region, and a larger time step is used in grid which are coarser. This would be of great benefit in our plasma simulations.

### 7.3.2 Unstructured Grids and Sub-cell Modeling

Cartesian grids have limited use when it comes to complex geometric structures such as circular loops or structures with a number of overlapping parts. The solutions usually become first order accurate in these regions and the resulting block-structured approximation is usually insufficient to capture fine-scale field structure especially around a curved surface. Two techniques that can be used to resolve this problem are unstructured grids and local sub-cell methods. Both have inherent strengths and weakness, but both methods are suitable to model more complex geometric structures than the traditional Cartesian mesh.

### 7.3.3 Particle in Cell Methods

Finally, our model would greatly benefit from the incorporation of particles, perhaps as an additional species so that wave-particle effects can be included. This improvement would allow for the study of instabilities, trapping, and a host of other single particle phenomena that are not resolved using a fluid approach. We could then gain the capability to model a more general category of plasma behavior in various operating environments.

# Appendix A

## Tensor Quantities

This Appendix gives the form of the velocity, pressure, heat-flux, and R-moment tensors discussed in Chapter 2.

$$\mathbf{u} = \begin{bmatrix} u_x \\ u_y \\ u_z \end{bmatrix} \quad (\text{A.1})$$

$$\mathbf{P} = \begin{bmatrix} p_{xx} & p_{xy} & p_{xz} \\ p_{yx} & p_{yy} & p_{yz} \\ p_{zx} & p_{zy} & p_{zz} \end{bmatrix} \quad (\text{A.2})$$

$$\mathbf{Q} = \begin{bmatrix} \begin{pmatrix} q_{xxx} \\ q_{xxy} \\ q_{xxz} \end{pmatrix} & \begin{pmatrix} q_{xyx} \\ q_{xyy} \\ q_{xyz} \end{pmatrix} & \begin{pmatrix} q_{xzx} \\ q_{xzy} \\ q_{xzz} \end{pmatrix} \\ \begin{pmatrix} q_{yxx} \\ q_{yxy} \\ q_{yxz} \end{pmatrix} & \begin{pmatrix} q_{yyx} \\ q_{yyy} \\ q_{yyz} \end{pmatrix} & \begin{pmatrix} q_{yzx} \\ q_{yzy} \\ q_{yzz} \end{pmatrix} \\ \begin{pmatrix} q_{zxx} \\ q_{zxy} \\ q_{zxz} \end{pmatrix} & \begin{pmatrix} q_{zyx} \\ q_{zyy} \\ q_{zyz} \end{pmatrix} & \begin{pmatrix} q_{zzx} \\ q_{zzy} \\ q_{zzz} \end{pmatrix} \end{bmatrix} \quad (\text{A.3})$$

$$\mathbf{R} = \left[ \begin{array}{ccc}
\begin{pmatrix} r_{xxxx} & r_{xxxy} & r_{xxxz} \\ r_{xxyx} & r_{xxyy} & r_{xxyz} \\ r_{xxzx} & r_{xxzy} & r_{xxzz} \end{pmatrix} &
\begin{pmatrix} r_{xyxx} & r_{xyxy} & r_{xyxz} \\ r_{xyyx} & r_{xyyy} & r_{xyyz} \\ r_{xyzx} & r_{xyzy} & r_{xyzz} \end{pmatrix} &
\begin{pmatrix} r_{zxzx} & r_{zxzy} & r_{zxxz} \\ r_{zzyx} & r_{zzyy} & r_{zzyz} \\ r_{zzzx} & r_{zzzz} & r_{zxxx} \end{pmatrix} \\
\begin{pmatrix} r_{yxxx} & r_{yxyx} & r_{yxxz} \\ r_{yxyx} & r_{yxyy} & r_{yxyz} \\ r_{yxzx} & r_{yxzy} & r_{yxxx} \end{pmatrix} &
\begin{pmatrix} r_{yyxx} & r_{yyxy} & r_{yyxz} \\ r_{yyyx} & r_{yyyy} & r_{yyyz} \\ r_{yyzx} & r_{yyzy} & r_{yyzz} \end{pmatrix} &
\begin{pmatrix} r_{yzxx} & r_{yzxy} & r_{yzxz} \\ r_{yzyx} & r_{yzyy} & r_{yzyz} \\ r_{yzzx} & r_{yzzz} & r_{yxxx} \end{pmatrix} \\
\begin{pmatrix} r_{zxxx} & r_{zxxz} & r_{zxxx} \\ r_{zxyx} & r_{zxyy} & r_{zxyz} \\ r_{zxxx} & r_{zxxx} & r_{zxxx} \end{pmatrix} &
\begin{pmatrix} r_{zyxx} & r_{zyxy} & r_{zyxz} \\ r_{zyyx} & r_{zyyy} & r_{zyyz} \\ r_{zyzx} & r_{zyzy} & r_{zyzz} \end{pmatrix} &
\begin{pmatrix} r_{zzxx} & r_{zzxy} & r_{zzxz} \\ r_{zzyx} & r_{zzyy} & r_{zzyz} \\ r_{zzzx} & r_{zzzy} & r_{zzzz} \end{pmatrix}
\end{array} \right] \tag{A.4}$$

# Appendix B

## Time Integration Schemes

### B.1 Staggered Leapfrog

The first method is the staggered leapfrog method which is commonly used in FDTD calculations [*Taflove and Hagness, 2000*]. As the name implies, this method entails the staggering of the electric and magnetic fields in time by  $1/2$  a time step. The method is  $2^{nd}$  order accurate and the most efficient of the explicit methods discussed in terms of time and storage requirements. The leapfrog method is conditionally stable with a time step governed by the Courant condition. A detailed description of this method is found in *Taflove and Hagness [2000]*.

### B.2 Runge-Kutta Methods

Unlike the staggered leapfrog presented in the last section, Runge-Kutta methods assume that all variables are located at the same instance in time. Runge Kutta methods are a class of multi-step methods in which the approximation of the time derivative is made up of a linear combination of intermediate steps. Runge Kutta methods differ from other multi-step methods such as Adams-Bashforth or Adams-Moulton methods in that they do not require storage of more than one previous function value to calculate the solution at the next incremental step. Instead, they only require knowledge of the past step and make subsequent approximations of the

$c_1$	$a_{11}$	$a_{12}$	$a_{13}$	$\cdots$	$a_{1s}$
$c_2$	$a_{21}$	$a_{22}$	$a_{23}$	$\cdots$	$a_{2s}$
$c_3$	$a_{31}$	$a_{32}$	$a_{33}$	$\cdots$	$a_{3s}$
$\vdots$	$\vdots$	$\vdots$	$\vdots$	$\ddots$	$\vdots$
$c_s$	$a_{s1}$	$a_{s2}$	$a_{s3}$	$\cdots$	$a_{ss}$
	$b_1$	$b_2$	$b_3$	$\cdots$	$b_s$

**Table B.1:** Butcher array for general  $s$ -stage Runge-Kutta method

solution in the range  $t_n - t_{n+1}$  where in this case, the incremental step is time. Though Runge-Kutta methods are not specific to the evaluation of time derivatives, this is the purpose for which we will use them, therefore all subsequent references will be with respect to a time.

Runge Kutta methods are commonly used in Computational Fluid Dynamics (CFD) codes which make them a convenient choice for their use in the fully non-linear warm plasma fluid code. Runge-Kutta (RK) methods are useful for solving systems of time-dependent first order differential equations of the form:

$$\frac{d\bar{\mathbf{y}}}{dt} = f(\bar{\mathbf{y}}, t) \quad (\text{B.1})$$

where  $\bar{\mathbf{y}}$  is a vector of unknowns and  $f$  is a function of  $\bar{\mathbf{y}}$  and time  $t$ . For an  $s$ -stage Runge-Kutta method, the solution at the next time-step denoted  $y_{n+1}$ , is equal to:

$$y_{n+1} = y_n + h \sum_{i=1}^s b_i k_i \quad (\text{B.2})$$

$$k_i = f \left( t_n + c_i h, y_n + h \sum_{j=1}^s a_{ij} k_j \right)$$

where  $h$  is the time-step,  $y_n$  is the solution at the past time step, and the coefficients  $a, b$  and  $c$  are elements of the corresponding Butcher array [Hairer et al., 2000; Hairer and Warner, 2002]:

$c_1$	0	0	0	$\cdots$	0
$c_2$	$a_{21}$	0	0	$\cdots$	0
$c_3$	$a_{31}$	$a_{32}$	0	$\cdots$	0
$\vdots$	$\vdots$	$\vdots$	$\vdots$	$\ddots$	$\vdots$
$c_s$	$a_{s1}$	$a_{s2}$	$a_{s3}$	$\cdots$	0
	$b_1$	$b_2$	$b_3$	$\cdots$	$b_s$

**Table B.2:** Butcher array for  $s$ -stage Explicit Runge-Kutta (ERK) method

### B.2.1 Explicit Runge Kutta

Explicit Runge-Kutta (ERK) methods are conditionally stable methods in which all variables are located at the same instance of time. In an ERK method, each intermediate function evaluation described by Equation B.3 only requires knowledge of the previous steps in the evaluation. The generalized  $s$ -stage ERK method is represented by the Butcher array of Table B.2.

The methods chosen for implementation into our model are those found in *Spiteri and Ruuth* [2002]. They are a family of Strong Stability Preserving (SSP) methods which offer a larger region of stability relative to the Courant condition than do other types of Runge Kutta methods. The methods chosen here range from 2nd to 4th order accuracy.

### B.2.2 Implicit Runge Kutta

The last types of time integration scheme incorporated into the model are called Implicit Runge Kutta (IRK) methods. These are fully implicit Runge Kutta methods with implementations that range from 2nd to 4th order accuracy. IRK methods are unconditionally stable and provide accurate integration for stiff systems of equations. This allows for time steps to far exceed the Courant condition, limited only by accuracy constraints. These methods are very useful in both the cold and warm plasma models that possess vastly different time scales. Such time-scales include the plasma and gyro frequencies, wave phase velocities and excitation frequencies, which will vary by orders of magnitude depending on cell size, among other factors.

Unlike the ERK methods of Section B.2.1, Implicit Runge-Kutta (IRK) methods

$c_1$	$a_{11}$	$0$	$0$	$\cdots$	$0$
$c_2$	$a_{21}$	$a_{22}$	$0$	$\cdots$	$0$
$c_3$	$a_{31}$	$a_{32}$	$a_{33}$	$\cdots$	$0$
$\vdots$	$\vdots$	$\vdots$	$\vdots$	$\ddots$	$\vdots$
$c_s$	$a_{s1}$	$a_{s2}$	$a_{s3}$	$\cdots$	$a_{ss}$
	$b_1$	$b_2$	$b_3$	$\cdots$	$b_s$

**Table B.3:** Butcher array for  $s$ -stage Single Diagonally Implicit Kunge-Kutta (SDIRK) method.

are unconditionally stable. In an IRK method, each intermediate function evaluation described by Equation B.3 requires function evaluations at both past and present values of the time step. Since the values of the solution at the current time step are unknown, this requires the use of a matrix inversion in order to find the solution. This matrix inversion solves the system defined by the intermediate steps of Equation B.3:

$$k_i - f\left(t_n + c_i h, y_n + h \sum_{j=1}^s a_{ij} k_j\right) = 0 \quad (\text{B.3})$$

The most general IRK method is given by the Butcher array in Table B.1. Since all elements of the Butcher array are unknown at each intermediate step, the size of the matrix inversion is equal to  $s$ -times the number of field unknowns making it an extremely computational intensive operation.

Single Diagonally Implicit Runge-Kutta (SDIRK) methods alleviate some of this difficulty by minimizing the size of the matrix inversion [Hairer and Warner, 2002, pages 91-101]. Instead of solving a single iteration which includes all  $s$ -stages of the RK method, each intermediate stage evaluation requires knowledge of only current and previous stages. Thus, although one needs to perform a matrix inversion for each stage, this process is sequential and the size of each stage is now only the number of field unknowns (a factor of  $n$  less than the full IRK method). The Butcher array corresponding to an SDIRK method is given in Table B.3

The nonlinear fluid moments of 2.1 requires a nonlinear solver. Thus the SDIRK methods utilize an analytical Jacobian in conjunction with a Newton-step for each stage of the Runge-Kutta update for the the system of differential equations given by

Equations 2.4a-2.4d.

### B.3 Alternating Direction Implicit

All Runge-Kutta methods require additional time steps to be stored, resulting in increased time and memory requirements. Another type of method which was considered but dismissed as a viable alternative to the fully implicit method was the Alternating Direction Implicit (ADI) method *Zheng et al.* [1999]. ADI methods have been around for decades, but *Zheng et al.* [1999] proved the unconditional stability for the 3-D system of Maxwell's equations. However, this method suffers from a few serious drawbacks as it relates to our model. The first is shown by *Garcia et al.* [2002] in that the ADI method, though unconditionally stable, is inaccurate for time steps well beyond the Courant condition. The second is that the ADI method is not easily implemented for a system of nonlinear equations as represented by the first few moments of Equation 2.1, and would prove too cumbersome for future extensions of the existing model, and is thus not included in our formulation.

# Appendix C

## Time Domain Solution to Z-mode Instability

Noise level transients are always present in FDTD based numerical simulations regardless of the source excitation characteristics. The frequency content of these simulations is limited only by the temporal sampling rate. Thus a PML which amplifies for given modes in the system will also amplify signals which exist in the noise levels. Analogous to the PML which amplifies waves in the whistler mode which possess wave normal vectors orthogonal to the static magnetic field, Z-mode wave propagation can exhibit these same instabilities inside of the PML. The difference between the two cases is that frequencies which correspond to Z-mode propagation are not intentionally excited and are a consequence of source transients at startup. Figure 3.8 illustrates this instability as a result of the Z-mode refractive index surface.

It is seen from Figure 3.8 that the PML oriented along the magnetic field which attenuated waves at frequencies in the whistler mode is now unstable for Z-mode propagation. However since we are not concerned with propagation at these frequencies for the purposes of radiation belt remediation, we can filter this frequency range out as discussed in the following section.

## C.1 Low-Pass Filtering of Cold Plasma Equations

The filtering of Z-mode frequencies is performed through the use of an FIR (Finite Impulse Response) filter. The application of FIR filtering to our system of equations follows that performed by *Sarto and Scarlatti* [2001] using the FDTD method. *Sarto and Scarlatti* [2001] originally proposed the use of low-pass FIR filters for removing high frequency transients which were a result of the free-space absorbing boundary condition used. The FIR filter as applied to our system of equations is a low-pass filter used to remove all frequencies beyond the whistler mode so that waves amplified at frequencies above the electron gyrofrequency due to a PML instability are immediately suppressed. FIR filters are chosen for their *linear phase*, and constant *group delay*. The linear phase means that there will be no phase distortion of the electromagnetic waves at different frequencies. The constant group delay means that the group delay is the same for all frequencies. The group delay is proportional to the number of ‘taps’ or ‘zeros’ of the filter as well as its causality. As it pertains to our simulation, the group delay constitutes a change in the refractive index of the medium. Therefore the larger the order of the filter, the smaller the wavelength. For instance, a group delay of 1 would modify the wavelength of a wave to 1/2 of its free-space value.

The filter response is realized by taking a weighted product of the filter coefficients with past, present and future values of the function you wish to filter as described by:

$$y[n] = \sum_{k=0}^{M-1} h(k) x(n-k) \quad (\text{C.1})$$

where  $M$  is the *filter order*,  $h$  represents the *filter coefficients*,  $x$  is the *input sequence*, and  $y$  is the *output sequence*. Since a distortion-less response is required for accurate simulation, we must make sure that the group delay is zero for all filters chosen. This limits the size of the filter since each filter coefficient of an FIR filter constitutes an additional past time-step to be stored and used in the time integration. For instance, a 5<sup>th</sup> order filter would not only require the storage of 4 additional time steps over

the current value, but the time integration scheme would need to utilize field values at two future time steps to maintain a zero group delay resulting in an FIR filter that is impossible to implement. The models presented here follow the lead of *Sarto and Scarlatti* [2001] and use a  $3^{rd}$  order filter requiring only one past and one future time step. The one future time step being the next stage in the time-sequence, is a natural bi-product of the solution process.

Since we have virtually no control over the frequency response of a  $3^{rd}$  order FIR filter due to the small number of coefficients used to describe the filter response, we must make sure that we have enough attenuation in the stop band. For a filter of a given order, this is controlled by the sampling frequency. If the frequency is too large (or the time step is too small such as for explicit time integration methods) the filter does not possess sufficient roll-off in the transition band to compensate for the exponential increase of the wave inside of the unstable PML. Thus as the cell size decreases, implicit methods now become mandatory in order to control the sampling frequency. Implicit methods such as the SDIRK method presented in Appendix B are not restricted by the Courant condition and thus the sampling frequency can be made much smaller, limited only by accuracy constraints.

# Appendix D

## Details of Finite Volume Method

The system of fluid moments comprising our plasma description can be cast into the following conservative form:

$$\frac{\partial \bar{\mathbf{U}}}{\partial t} + \nabla \cdot \mathcal{F}(\bar{\mathbf{U}}) = \bar{\mathbf{S}} \quad (5.6)$$

where  $\bar{\mathbf{U}}$  is a vector of *conserved* quantities,  $\mathcal{F}$  is a nonlinear *flux* function, and  $\bar{\mathbf{S}}$  corresponds to the *source* terms for each moment.

### D.1 Shocks and Artificial Viscosity

In computational fluid dynamics (CFD), shocks are defined as spatial fluctuations that are smaller than the minimum cell size used in the simulation space. The inadequate spatial sampling of the shock wave will, in turn, produce oscillations resulting from Gibbs phenomena, since the mesh is unable to capture the extremely high spatial frequencies. Shock capturing schemes are methods which attempt to capture these small wavelength features without producing spurious oscillations. The method of *Kurganov and Tadmor* [2000] uses artificial viscosity which adds a second order diffusion term to each moment in the system of fluid equations. Assuming a 1-d solution with  $\hat{x}$ -dependence only, the conservation law of Equation 5.6 with artificial diffusion is represented by Equation D.1:

$$\frac{\partial \bar{U}}{\partial t} + \frac{\partial \mathcal{F}}{\partial x} - D \frac{\partial^2 \bar{U}}{\partial x^2} = 0 \quad (\text{D.1})$$

where  $D$  is the *diffusion* coefficient.

## D.2 Flux Calculation

The method of *Kurganov and Tadmor* [2000] includes the artificial viscosity using a nonlinear limiting function which is summarized in this section. The diffusion coefficient of *Kurganov and Tadmor* [2000] is present within the flux contribution for the corresponding cell face. Assuming the 1-d system defined by Equation D.1 and neglecting the diffusion term, the  $\hat{x}$ -component of the flux is:

$$\frac{dU}{dt} = -\frac{F_{i+\frac{1}{2}} - F_{i-\frac{1}{2}}}{\Delta x} \quad (\text{D.2})$$

where the flux function through the positive cell face at  $i + \frac{1}{2}$  is given as:

$$F_{i+\frac{1}{2}} := \frac{F(U_{i+\frac{1}{2}}^+) + F(U_{i+\frac{1}{2}}^-)}{2} - \frac{a_{i+\frac{1}{2}}}{2} [U_{i+\frac{1}{2}}^+ - U_{i+\frac{1}{2}}^-] \quad (\text{D.3})$$

The term  $\frac{a_{i+\frac{1}{2}}}{2} [U_{i+\frac{1}{2}}^+ - U_{i+\frac{1}{2}}^-]$  represents the positive flux contribution of the artificial diffusion component and the spectral radius  $a_{j+\frac{1}{2}}^n$  was given previously in Equation 5.8 of Chapter 5 as:

$$a_{j+\frac{1}{2}}^n = \max_{\bar{U} \in \mathcal{C}(U_{j+1/2}^-, U_{j+1/2}^+)} \rho \left( \frac{\partial \mathcal{F}}{\partial \bar{U}} (\bar{U}) \right) \quad (5.8)$$

The intermediate values are:

$$U_{i+\frac{1}{2}}^+ := U_{i+1} - \frac{\Delta x}{2} (U_x)_{i+1} \quad (\text{D.4a})$$

$$U_{i+\frac{1}{2}}^- := U_i + \frac{\Delta x}{2} (U_x)_i \quad (\text{D.4b})$$

where the the quantity  $(U_x)_i$  represents a *derivative* given by:

$$(U_x)_i := \text{minmod} \left( \frac{U_i - U_{i-1}}{\Delta x}, \frac{U_{i+1} - U_{i-1}}{2\Delta x}, \frac{U_{i+1} - U_i}{\Delta x} \right) \quad (\text{D.5})$$

The *minmod* function is the nonlinear *limiter* which suppresses oscillations. This function is equal to:

$$\text{minmod}(a, b) := \frac{1}{2} [\text{sgn}(a) + \text{sgn}(b)] \cdot \min(|a|, |b|) \quad (\text{D.6})$$

where *min* is a function which takes the smallest value of the list of arguments and *sgn* represents the *signum* function given by Equation D.7

$$\text{sgn}(x) = \begin{cases} -1 & : x < 0 \\ 0 & : x = 0 \\ 1 & : x > 0 \end{cases} \quad (\text{D.7})$$

### D.3 Shock Capture

The benefit of the artificial diffusion term is most readily shown in Figure D.1 which represents the propagation of a Gaussian pulse and square wave at a particular instance in time  $t > 0$ . Figures D.1a-D.1c demonstrate the effectiveness of three different spatial differencing methods on capturing solutions with steep gradients. The methods shown in Figures D.1a, D.1b, and D.1c are Lax-Wendroff, the 1<sup>st</sup>-order upwind method, and a FV method using the *minmod* limiter. The Lax-Wendroff method, which uses finite differences as in the FDTD technique, produces highly oscillatory behavior. The 1<sup>st</sup>-order upwind method contains implicit diffusion but is not tailored to the local wave speeds and is thus very diffusive. Meanwhile, the solution representing the *minmod* limiter of Figure D.1c suppresses oscillations yet is able to capture the steep gradients in the solution.

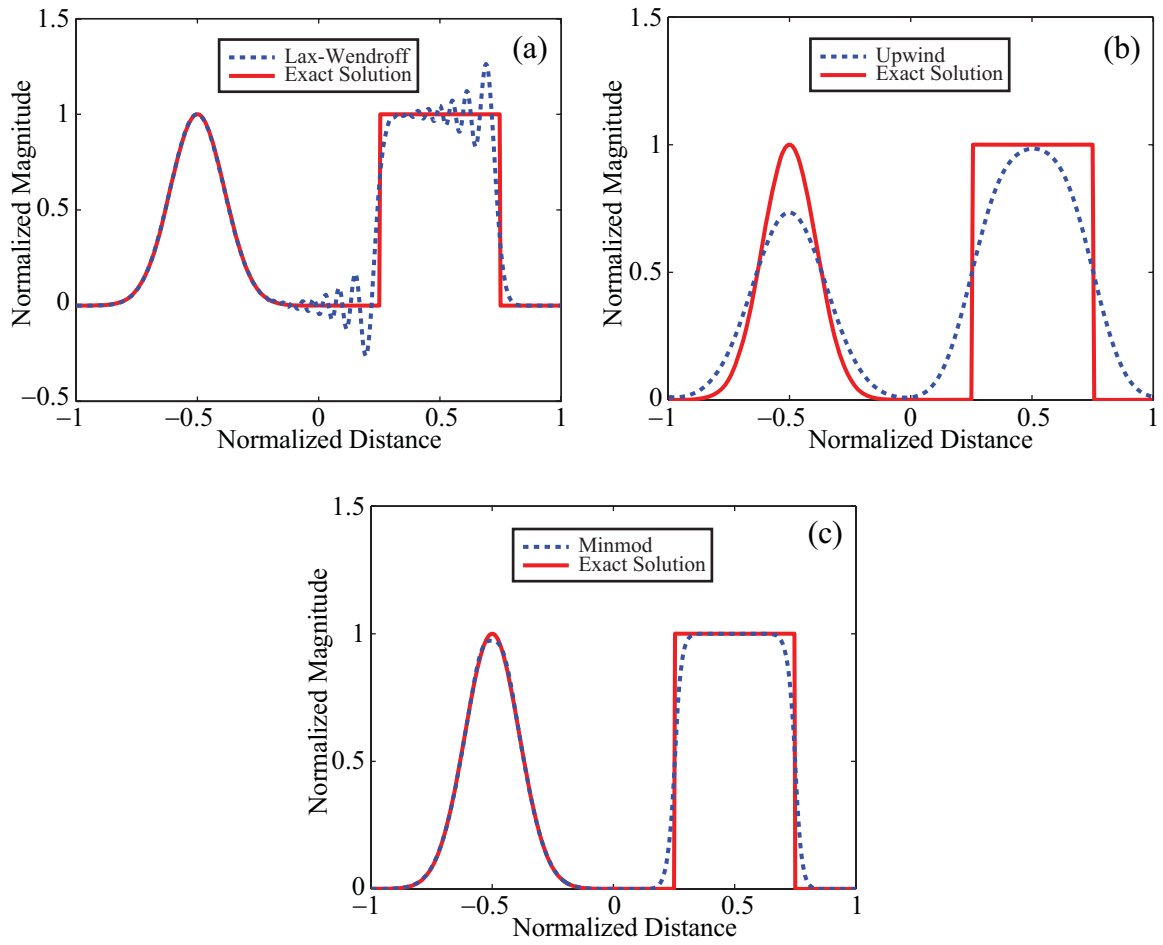


**Figure D.1:** Example of shock capturing scheme. (a) Lax-Wendroff. (b) 1<sup>st</sup> order upwind method. (c) Minmod limiter.

# Bibliography

- Abel, B., and R. Thorne, Electron scattering loss in Earth's inner magnetosphere. 1. dominant physical processes, *Journal of Geophysical Research*, 103(A2), 2385–2396, 1998.
- Albert, J., Comparison of pitch angle diffusion by turbulent and monochromatic whistler waves, *Journal of Geophysical Research*, 106(A5), 8477–8482, 2001.
- Amatucci, W., D. Blackwell, D. Walker, G. Gatling, and G. Ganguli, Whistler wave propagation and whistler wave antenna radiation resistance measurements, *IEEE Transactions on Plasma Science*, 33(2), 637–646, doi:10.1109/TPS.2005.844607, 2005.
- Anile, A. M., N. Nikiforakis, and R. M. Pidatella, Assessment of a high resolution centered scheme for the solution of hydrodynamical semiconductor equations, *SIAM Journal on Scientific Computing*, 22(5), 1533–1548, 2000a.
- Anile, A. M., V. Romano, and G. Russo, Extended hydrodynamical model of carrier transport in semiconductors, *SIAM Journal on Applied Mathematics*, 61(1), 74–101, 2000b.
- Baboolal, S., Boundary conditions and numerical fluid modelling of time-evolutionary plasma sheaths, *Journal of Physics. D, Applied Physics*, 35(7), 658–664, 2002.
- Baker, D., H. Weil, and L. Bearce, Impedance and large signal excitation of satellite-borne antennas in the ionosphere, *IEEE Transactions on Antennas and Propagation*, AP-21(5), 672–679, 1973.

- Balay, S., K. Buschelman, W. Gropp, D. Kaushik, M. Knepley, L. McInnes, B. Smith, and H. Zhang, PETSc Web page, 2001.
- Balay, S., K. Buschelman, V. Eijkhout, W. Gropp, D. Kaushik, M. Knepley, L. McInnes, B. Smith, and H. Zhang, *PETSc Users Manual*, Argonne National Laboratory, anl-95/11 - revision 2.1.5. ed., 2004.
- Balmain, K., The impedance of a short dipole antenna in a magnetoplasma, *IEEE Transactions on Antennas and Propagation*, *AP-12*(5), 605–617, 1964.
- Balmain, K., Antennas in plasma: characteristics as functions of frequency, *Radio Science*, *7*(8-9), 771–775, 1972.
- Balmain, K., Properties of antennas in plasmas, *Annales Des Telecommunications*, *34*(3-4), 273–283, 1979.
- Barakat, A. R., and R. W. Schunk, Transport equations for multicomponent anisotropic space plasmas: a review, *Plasma Physics*, *24*(4), 389–418, 1982a.
- Barakat, A. R., and R. W. Schunk, Comparison of transport equations based on maxwellian and bi-maxwellian distributions for anisotropic plasmas, *Journal of Physics. D, Applied Physics*, *15*(7), 1195–1216, 1982b.
- Becache, E., S. Fauqueux, and P. Joly, Stability of perfectly matched layers, group velocities and anisotropic waves, *Journal of Computational Physics*, *188*(2), 399–433, 2003.
- Bell, T., U. Inan, M. Platino, J. Pickett, P. Kossey, and E. Kennedy, CLUSTER observations of lower hybrid waves excited at high altitudes by electromagnetic whistler mode signals from the HAARP facility, *Geophysical Research Letters*, *31*(6), L06811 1-5, 2004.
- Bell, T., U. Inan, and T. Chevalier, Current distribution of a VLF electric dipole antenna in the plasmasphere, *Radio Science*, *41*(2), 2006.

- Berenger, J.-P., A perfectly matched layer for the absorption of electromagnetic waves, *Journal of Computational Physics*, 114(2), 185–200, 1994.
- Bezrukikh, V. V., G. A. Kotova, L. A. Lezhen, J. Lemaire, V. Pierrard, and Y. I. Venediktov, Dynamics of temperature and density of cold protons of the Earth's plasmasphere measured by the auroral probe/alpha-3 experiment data during geomagnetic disturbances, *Cosmic Research*, 41(4), 392–402, 2003.
- Bittencourt, J., *Fundamentals of plasma physics*, third ed., Bittencourt, J.A., 2003.
- Blackwell, D., D. Walker, and W. Amatucci, Measurement of absolute electron density with a plasma impedance probe, *Review of Scientific Instruments*, 76(2), 023,503–023,506, 2005.
- Bohm, D., *The characteristics of electrical discharges in magnetic fields*, edited by Guthrie, A. and Wakerling, R.K. (New York: McGraw-Hill), Chapter 3, p. 77., 1949.
- Borovsky, J., The dynamic sheath: objects coupling to plasmas on electron-plasma-frequency time scales, *The Physics of Fluids*, 31(5), 1074–1100, 1988.
- Bruno, D., C. Catalfamo, A. Laricchiuta, D. Giordano, and M. Capitelli, Convergence of chapman-enskog calculation of transport coefficients of magnetized argon plasma, *Physics of Plasmas*, 13(7), 072307 1-9, 2006.
- Budden, K., *The propagation of radio waves*, Cambridge University Press, 1985.
- Calder, A. C., and J. G. Laframboise, Time-dependent sheath response to abrupt electrode voltage changes, *Physics of Fluids. B, Plasma Physics*, 2(3), 655–666, 1990.
- Calder, A. C., G. W. Hulbert, and J. G. Laframboise, Sheath dynamics of electrodes stepped to large negative potentials, *Physics of Fluids. B, Plasma Physics*, 5(3), 674–690, 1993.

- Carpenter, D., and R. Anderson, An ISEE/whistler model of equatorial electron density in the magnetosphere, *Journal of Geophysical Research*, 97(A2), 1097–1108, 1992.
- Carpenter, D., T. Bell, U. Inan, R. Benson, V. Sonwalkar, B. Reinisch, and D. Gallagher, Z-mode sounding within propagation cavities and other inner magnetospheric regions by the RPI instrument on the IMAGE satellite, *Journal of Geophysical Research*, 108(A12), 1421, 2003.
- Chapman, S., and T. G. Cowling, *The Mathematical Theory of Non-Uniform Gases*, 3rd ed., Cambridge UP: London, 1970.
- Chevalier, M., and U. Inan, A PML using a convolutional curl operator and a numerical reflection coefficient for general linear media, *IEEE Transactions on Antennas and Propagation*, 52(7), 1647–1657, 2004.
- Chew, G. F., M. L. Goldberger, and F. E. Low, The Boltzmann equation and the one-fluid hydromagnetic equations in the absence of particle collisions, *Proceedings of the Royal Society of London. Series A, Mathematical and Physical Sciences*, 236, 112–118, 1956.
- Chew, W. C., and W. Weedon, A 3D perfectly matched medium from modified Maxwells equations with stretched coordinates, *Microwave and Optical Technology Letters*, 7(13), 599–604, 1994.
- Chust, T., and G. Belmont, Closure of fluid equations in collisionless magnetoplasmas, *Physics of Plasmas*, 13(1), 012506 1-21, 2006.
- Cluggish, B., and C. Munson, Secondary electron enhanced discharges in plasma source ion implantation, *Journal of Applied Physics*, 84(11), 5945–5955, 1998.
- Cook, D., and I. Katz, Ionization-induced instability in an electron-collecting sheath, *Journal of Spacecraft and Rockets*, 25(2), 132–138, 1988.
- Courant, R., K. Friedrichs, and H. Lewy, On partial difference equations of mathematical physics, *IBM Journal of Research and Development*, 11(2), 215–234, 1967.

- Cummer, S., An analysis of new and existing FDTD methods for isotropic cold plasma and a method for improving their accuracy, *IEEE Transactions on Antennas and Propagation*, 45(3), 392–400, 1997.
- Cummer, S., Perfectly matched layer behavior in negative refractive index materials, *IEEE Antennas and Wireless Propagation Letters*, 3(1), 172–175, 2004.
- Demmel, J., *Applied numerical linear algebra*, SIAM, 1997.
- Eriksson, K., D. Estep, P. Hansbo, and C. Johnson, *Computational differential equations*, Cambridge University Press, 1996.
- Franklin, R., and W. Han, The stability of the plasma-sheath with secondary emission, *Plasma Physics and Controlled Fusion*, 30(6), 771–784, 1988.
- Franklin, R. N., The plasma-sheath boundary region, *Journal of Physics. D, Applied Physics*, 36(22), R309–R320, 2003.
- Franklin, R. N., Where is the sheath edge?, *Journal of Physics. D, Applied Physics*, 37(9), 1342–1345, 2004.
- Furkal, E., and A. Smolyakov, The generalized hydrodynamic equations for arbitrary collision frequency in a weakly ionized plasma, *Physics of Plasmas*, 7(1), 122–134, 2000.
- Garcia, S., T.-W. Lee, and S. Hagness, On the accuracy of the ADI-FDTD method, *IEEE Antennas and Wireless Propagation Letters*, 1, 31–34, 2002.
- Gendrin, R., Le guidage des whistlers par le champ magnetique, *Planetary and Space Science*, 5(4), 274–278, 1961.
- Godyak, V., and N. Sternberg, On the consistency of the collisionless sheath model, *Physics of Plasmas*, 9(11), 4427–4430, 2002.
- Godyak, V. A., and N. Sternberg, Dynamic model of the electrode sheaths in symmetrically driven rf discharges, *Physical Review. A, General Physics*, 42(4), 2299–2312, 1990a.

- Godyak, V. A., and N. Sternberg, Smooth plasma-sheath transition in a hydrodynamic model, *IEEE Transactions on Plasma Science*, 18(1), 159–168, 1990b.
- Goswami, P., T. Passot, and P. L. Sulem, A Landau fluid model for warm collisionless plasmas, *Physics of Plasmas*, 12(10), 102109 1-9, 2005.
- Hairer, E., and G. Warner, *Solving ordinary differential equations II: stiff and differential-algebraic problems*, Springer, 2002.
- Hairer, E., S. Nørsett, and G. Warner, *Solving ordinary differential equations I: non-stiff problems*, vol. 8, 14, Springer, 2000.
- Hockney, R. W., and J. W. Eastwood, *Computer simulation using particles*, McGraw-Hill International Book Co., New York, 1981.
- Inan, U., T. Bell, J. Bortnik, and J. Albert, Controlled precipitation of radiation belt electrons, *Journal of geophysical research*, 108(A5), 1186 1-11, 2003.
- Keller, K., M. Hesse, M. Kuznetsova, L. Rastatter, T. Moretto, T. Gombosi, and D. DeZeeuw, Global MHD modeling of the impact of a solar wind pressure change, *Journal of Geophysical Research*, 107(A7), 1126 1-8, 2002.
- Kivelson, M., and C. Russell, *Introduction to space physics*, Cambridge University Press, 1995.
- Kraus, J., *Antennas*, second ed., McGraw Hill, 1988.
- Kumar, H., and S. Roy, Hydrodynamic model of plasma-sheath for RF discharges with and without collision, *43rd AIAA Aerospace Sciences Meeting and Exhibit Meeting Papers*, (AIAA2005-948), 9327, 2005.
- Kurganov, A., and E. Tadmor, New high-resolution central schemes for nonlinear conservation laws and convection-diffusion equations, *Journal of Computational Physics*, 160(1), 241–282, 2000.

- Labrunie, S., J. A. Carrillo, and P. Bertrand, Numerical study on hydrodynamic and quasineutral approximations for collisionless two-species plasmas, *Journal of Computational Physics*, 200(1), 267–298, 2004.
- Laframboise, J. G., Current collection by a positively charged spacecraft: effects of its magnetic presheath, *Journal of Geophysical Research*, 102(A2), 2417–2432, 1997.
- Langmuir, I., The interaction of electron and positive ion space charges in cathode sheaths, *Physical Review*, 33(6), 0954–0989, 1929.
- Laurin, J. J., G. A. Morin, and K. G. Balmain, Sheath wave propagation in a magnetoplasma, *Radio Science*, 24(3), 289–300, 1989.
- Lee, J. H., and D. Kalluri, Three-dimensional FDTD simulation of electromagnetic wave transformation in a dynamic inhomogeneous magnetized plasma, *IEEE Transactions on Antennas and Propagation*, 47(7), 1146–1151, 1999.
- Lieberman, M. A., Analytical solution for capacitive rf sheath, *IEEE Transactions on Plasma Science*, 16(6), 638–644, 1988.
- Lieberman, M. A., Dynamics of a collisional, capacitive RF sheath, *IEEE Transactions on Plasma Science*, 17(2), 338–341, 1989.
- Luttgen, A. A. E., and K. G. Balmain, Nonreciprocal magnetoplasma sheath waves, *Radio Science*, 31(6), 1599–1613, 1996.
- Ma, T., and R. Schunk, A fluid model of high voltage spheres in an unmagnetized plasma, *Plasma Physics and Controlled Fusion*, 31(3), 399–421, 1989.
- Ma, T., and R. Schunk, High negative voltage spheres in an unmagnetized plasma: fluid simulation, *Plasma Physics and Controlled Fusion*, 34(5), 783–799, 1992a.
- Ma, T., and R. Schunk, High-voltage spheres in an unmagnetized plasma: long-term evolution and rise-time effects, *Plasma Physics and Controlled Fusion*, 34(5), 767–781, 1992b.

- Mlodnosky, R. F., and O. K. Garriott, The V.L.F. admittance of a dipole in the lower ionosphere, *Proc. of the Int'l Conf. on the Ionosphere, London, July 1962*, p. 484, 1963.
- Morin, G. A., and K. G. Balmain, Hydrodynamic radio-frequency model of an ion sheath near a conductor in a plasma, *Radio Science*, *26*(2), 459–467, 1991.
- Morin, G. A., and K. G. Balmain, Plasma sheath and presheath waves: theory and experiment, *Radio Science*, *28*(2), 151–168, 1993.
- Nikitin, P., and C. Swenson, Impedance of a short dipole antenna in a cold plasma, *IEEE Transactions on Antennas and Propagation*, *49*(10), 1377–1381, 2001.
- Palmadesso, P., Interaction of a spherical high voltage probe with the space environment: electron trapping, current drain and collective process, in *Proceedings of the Intersociety Energy Conversion Engineering Conference*, vol. 1, pp. 435–440, 1989.
- Parker, L., and B. Murphy, Potential buildup on electron-emitting ionospheric satellite, *Journal of Geophysical Research*, *72*(5), 1631–1636, 1967.
- Parker, S. E., A. Friedman, S. L. Ray, and C. K. Birdsall, Bounded multiscale plasma simulation - application to sheath problems, *Journal of Computational Physics*, *107*(2), 388–402, 1993a.
- Parker, S. E., R. J. Procassini, C. K. Birdsall, and B. I. Cohen, A suitable boundary condition for bounded plasma simulation without sheath resolution, *Journal of Computational Physics*, *104*(1), 41–49, 1993b.
- Platino, M., U. Inan, T. Bell, D. Gurnett, J. Pickett, P. Canu, and P. Decreau, Whistlers observed by the cluster spacecraft outside the plasmasphere, *Journal of Geophysical Research*, *110*(A3), A03212 1-16, 2005.
- Procassini, R. J., C. K. Birdsall, and E. C. Morse, A fully kinetic, self-consistent particle simulation model of the collisionless plasma-sheath region, *Physics of Fluids. B, Plasma Physics*, *2*(12), 3191–3205, 1990.

- Ramos, J. J., Dynamic evolution of the heat fluxes in a collisionless magnetized plasma, *Physics of Plasmas*, 10(9), 3601–3607, 2003.
- Ramos, J. J., Fluid formalism for collisionless magnetized plasmas, *Physics of Plasmas*, 12(5), 052102 1-14, 2005.
- Riemann, K. U., Bohm criterion and sheath formation, *Journal of Physics. D, Applied Physics*, 24(4), 493–518, 1991.
- Roy, S., B. P. Pandey, J. Poggie, and D. V. Gaitonde, Modeling low pressure collisional plasma sheath with space-charge effect, *Physics of Plasmas*, 10(6), 2578–2585, 2003.
- Salat, G. A., Non-linear plasma transport equations for high flow velocity, *Plasma Physics*, 17(7-8), 589–607, 1975.
- Sarto, M., and A. Scarlatti, Suppression of late-time instabilities in 3-D-FDTD analyses by combining digital filtering techniques and efficient boundary conditions, *IEEE Transactions on Magnetics*, 37(5), 3273–3276, 2001.
- Self, S. A., Exact solution of collisionless plasma-sheath equation, *The Physics of Fluids*, 6(12), 1762–1768, 1963.
- Shkarofsky, I., Nonlinear sheath admittance, currents, and charges associated with high peak voltage drive on a VLF/ELF dipole antenna moving in the ionosphere, *Radio Science*, 7(4), 503–523, 1972.
- Song, P., B. W. Reinisch, V. Paznukhov, G. Sales, D. Cooke, J. N. Tu, X. Huang, K. Bibl, and I. Galkin, High-voltage antenna-plasma interaction in whistler wave transmission: plasma sheath effects, *Journal of Geophysical Research*, 112(A3), A03205 1-12, 2007.
- Spiteri, R. J., and S. J. Ruuth, A new class of optimal high-order strong-stability-preserving time discretization methods, *SIAM Journal on Numerical Analysis*, 40(2), 469–491, 2002.

- Stenzel, R., Antenna radiation patterns in the whistler wave regime measured in a large laboratory plasma, *Radio Science*, 11, 1045–1056, 1976.
- Stenzel, R. L., Instability of the sheath-plasma resonance, *Phys. Rev. Lett.*, 60(8), 704–707, 1988.
- Stix, T., *The theory of plasma waves*, McGraw-Hill, 1962.
- Taflove, A., and S. Hagness, *Computational electrodynamics : the finite-difference time-domain method*, second ed., Artech House, 2000.
- Thiemann, H., T. Z. Ma, and R. W. Schunk, High voltage spheres in an unmagnetized plasma: fluid and PIC simulations, *Advances in Space Research*, 12(12), 57–60, 1992.
- Trovato, M., and P. Falsaperla, Full nonlinear closure for a hydrodynamic model of transport in silicon, *Physical Review. B, Condensed Matter*, 57(8), 4456–4471, 1998.
- Vandenberg, H. P., K. U. Riemann, and G. Ecker, The plasma-sheath transition in an asymmetric collisionless plasma, *Physics of Fluids. B, Plasma Physics*, 3(3), 838–846, 1991.
- Walker, D., R. Fernsler, D. Blackwell, W. Amatucci, and S. Messer, On collisionless energy absorption in plasmas: theory and experiment in spherical geometry, *Physics of Plasmas*, 13(3), 032108 1-9, 2006.
- Walt, M., *Introduction to geomagnetically trapped radiation*, Cambridge University Press, 1994.
- Wang, S. B., and A. E. Wendt, Sheath thickness evaluation for collisionless or weakly collisional bounded plasmas, *IEEE Transactions on Plasma Science*, 27(5), 1358–1365, 1999.
- Wang, T., and T. Bell, Radiation resistance of a short dipole immersed in a cold magnetoionic medium, *Radio Science*, 4, 167–177, 1969.

- Wang, T., and T. Bell, On VLF radiation resistance of an electric dipole in a cold magnetoplasma, *Radio Science*, 5(3), 605–610, 1970.
- Wang, T., and T. Bell, VLF/ELF radiation patterns of arbitrarily oriented electric and magnetic dipoles in a cold lossless multicomponent magnetoplasma, *Journal of Geophysical Research*, 77, 1174–1189, 1972a.
- Wang, T., and T. Bell, Electric dipole radiation at VLF in a uniform warm magnetoplasma, *Revue de Physique Appliquee*, 7(1), 11–20, 1972b.
- Wang, T., and T. Bell, VLF/ELF input impedance of an arbitrarily oriented loop antenna in a cold collisionless multicomponent magnetoplasma, *IEEE Transactions on Antennas and Propagation*, 20(3), 394–398, 1972c.
- Wang, T. N.-C., VLF input impedance characteristics of an electric antenna in a magnetoplasma, Ph.D. thesis, Stanford University, 1970.
- Ward, J., C. Swenson, and C. Furse, The impedance of a short dipole antenna in a magnetized plasma via a finite difference time domain model, *IEEE Transactions on Antennas and Propagation*, 53(8), 2711–2718, 2005.
- Yee, K., Numerical solution of initial boundary value problems involving Maxwell's equations in isotropic media, *IEEE Transactions on Antennas and Propagation*, AP-14(3), 302–307, 1966.
- Zheng, F., Z. Chen, and J. Zhang, A finite-difference time-domain method without the courant stability conditions, *IEEE Microwave and Guided Wave Letters*, 9(11), 441–443, 1999.